UTRECHT UNIVERSITY

DELTARES

Future sand dynamics in the Mekong Delta

Author

Aris Kwadijk

Supervisors

Maarten van der Vegt (UU) & Mick van der Wegen (Deltares)

Final version

30-6-2023

Contents

List of Figures

Chapter 1

Acknowledgement

I hereby want to thank everyone involved in this project. First of all, I want to thank my supervisors Maarten van der Vegt and Mick dan der Wegen for all the weekly morning discussions. These gave me great new insights. Also I want to thank Fleur for all the support she gave me this year, especially during the last weeks, this has been a great help. My parents in Haarlem, who were always there when I needed them this year. And lastly, my roommates for keeping me optimistic about the process.

Chapter 2

Abstract

As sand is a key building element of deltas, human interference with sand transport alters the deltas morphology. In the Mekong Delta, upstream sediment trapping by dams and local sand mining practises have already proven to rapidly change the deltas morphology in the form of river bed deepening and coastal retreat, resulting in land loss and increased salinisation in the delta. Further processes that contribute to these problems in the delta are delta-wide subsidence due to groundwater extraction and global sea level rise (SLR). This study aims to provide an overview on the projected changes in sand transport mechanisms due to SLR, subsidence, river bed lowering and discharge alteration by dams. For this, a delta-wide DELFT3D-FM hydro- and morphological model is used to illustrate the current complex sand dynamics inside the delta. This study shows the influence of human impact on the deltas internal sand dynamics by separately testing the systems response to SLR sea level, subsidence, river bed lowering and an altered discharge. In the end, projected changes on sand dynamics for 2040 were simulated. The results confirm the different distinct hydrodynamic regimes present in the delta. In the fluvial dominated tract seaward sand transport is highly variable and rates are 1-2 orders of magnitude larger than in the estuaries downstream. Here, a reduced wet season discharge results in lower net annual sand transport volumes. Deepening the river bed lowers water levels relative to the banks, effectively capturing the peak flow, reducing the deltas buffering capacity. This ultimately increases the seasonality of the sand transport in this region. In the fluvial-tidal regime, seaward sand export increases by the amplified tidal velocity amplitude as a result of SLR, subsidence and river bed deepening. In the tide-dominated regime, seaward sand export rates decrease as increased water depth in the wide estuaries results in a large increase in the estuaries cross-sectional area, reducing the tidal flow velocity amplitude. Sand influx from the Mekong is expected to decrease as wet season discharge is reduced. Furthermore, increased erosion rates can be expected near My Thuan, contributing to the already present river-bank instability. Lastly, the low transport rates in the smaller estuaries show that sand replenishment is slow, therefore exploitation in these regions will have long-term consequences for the sand availability here. The results of this study can be used to identify locations where morphological changes can be expected in other deltas worldwide.

Chapter 3

Introduction

Located at the East Sea, the Mekong delta is the worlds third largest delta and is home to around 20 million people. In Vietnam, about 60% of the area is cultivated (Q. V. Thanh, 2021), as it provides 50% of the nation's food production (Anthony et al., 2015). With an average elevation of only 0.8m above sea level (Minderhoud et al., 2019) and extreme seasonal discharge variability, the VMD is highly vulnerable to salinisation, flooding and loss of land. The resilience of the delta against these actors has been in decline as the delta's aggradation rate is outpaced by relative sea level rise (RSLR) (Zoccarato et al., 2018). This disequilibrium is mainly the result of groundwater extraction-induced subsidence (Minderhoud et al. (2018, 2020)). Reduced sediment availability due to the construction of hydropower dams upstream and sand mining in the VMDs river channels (Kummu and Varis, 2007) (Anthony et al., 2015), results in rapid (up to 0.13 m/yr) (Eslami et al., 2019) widespread deepening of the channels throughout the delta, reducing the river's bank stability (Hackney et al., 2020), resulting in land loss, jeopardising agricultural practises and eventually, the livelihood of its inhabitants.

The problems residing by the disequilibrium between the delta's sediment demand and supply have resulted in many studies being conducted on sediment budget estimations inside the delta.Q. V. Thanh, 2021 found that 23% of the sediment flux at Kratie, Cambodia, reaches the East sea, while the remaining portion is trapped on the floodplains and inside the river channels. Incoming sediment load estimations at Kratie before the dam period range between 145-166.7 Mt/yr (Kondolf et al., 2014), (Binh et al., 2020), (Li et al., 2017). After the construction of upstream dams, this dropped by 70-80% (Binh et al., 2020), (Nowacki et al., 2015). Estimates predict that the 130 existing and planned dams will decrease the total sediment load up to 90% compared to the pre-dam period (Kondolf et al., 2014), reducing the sedimentation rates on the floodplains and the deltas sediment export volumes (Manh et al., 2015).

While sand only contributes 5-20% of the total sediment portion in the Mekong River in the VMD, (Hackney et al., 2020), it's a key building element in the delta. Fines are moving rapidly throughout the delta as it resides in suspension more often than sand, resulting in short residence times inside the delta. As sand is deposited along the way, it drives river bed morphology and, on longer timescales, the morphology of the delta as a whole. At the same time, this fraction of the sediment flux is being mined most severely (Gruel et al., 2022), (Bravard et al., 2013). Although sand dynamics at specific sites have been investigated (Stephens et al., 2017), (Hackney et al., 2020), (Nowacki et al., 2015) no delta-wide studies have been performed on sand dynamics. This study, therefore, aims to provide insight into the current and future sand dynamics of the Mekong Delta.

Chapter 4

Background/Study area

4.1. Study area extend

The official Mekong Delta is defined as the roughly triangular area between Phomn Penh, the Saigon River mouth near Ho Chi Minh City and Ca Mau Cape, in the most southwestern of Vietnam. It covers an area between 62,520 and 93,781 km^2 (Ta et al., 2002). The study area covers the Mekong River from Kratie, Cambodia up to the seven main outlets at the East Sea (Figure 4.1). In Cambodia, it includes Tonle Sap Lake in the North East, which is connected via the Tonle Sap River (TSR) and confluences into the Mekong River at Phnom Penh. Here, at the apex, the Mekong River splits into the Bassac- and Tien River branches. The Tien river further divides into five outlets, in this study named: the Vamkenh, Binhdai, Anthuan, Bentrai and Mylong outlets. The Bassac branch is joined by the Vamn Nao River, connecting it with the Tien River, and continues as the Hau River. The Hau River splits into two outlets, in this study named the Dinhan (East) and Trande outlet (West). Besides these main river branches, the study area includes the adjacent floodplains in both Cambodia and Vietnam and an extensive network of smaller canals in Vietnam, indicated in grey in Figure 4.1. The study area is split up into three different sections: The upper delta, which includes the Mekong River and Tonle Sap River (TSR) up to the confluence with the Tonle Sap River at Phomn Penh, followed by the Middle delta, with its upstream border at Phomn Penh and downstream border at My Thuan, and the lower delta, which includes the seven main outlets downstream of My Thuan. The three different sections are based on the different hydrodynamic regimes described by Gugliotta et al., 2017 and further elaborated.

4.2. Hydrodynamic boundary conditions

The hydrodynamic character of the study area is determined by three main actors: 1) the highly seasonal discharge volumes at Kratie, 2) the buffering of effect on the discharge of Tonle Sap Lake, and 3) the increasing tidal influence towards the mouth.

4.2.1. Discharge

Discharge in the Mekong is highly seasonal and is modulated by two monsoon systems, the southwest Indian monsoon and the northwest Pacific monsoon (Cook et al., 2012). During the dry season (December to April) the natural discharge is controlled by snow melt and local precipitation from the upper basin in the Yunnan region of China(Cook et al., 2012). During the wet season (May to November), discharge is controlled by precipitation and the left-bank tributaries in Laos and Vietnam. In this period the total discharged volume of water ranges between 85-90%, with its peak discharge during the wet season ranging between 30.000 and 50.000 m^3/s and an average peak flow of 45.000 m^3/s at Kratie (Binh et al., 2020) (Figure 4.2). During the dry season, discharge can drop to 2000 m^3/s. Annually, approximately 416 km^3 of water flows through Kratie, of which an estimated 80% flows through the Tien River branch and 20% through the Bassac branch (Quoc Thanh et al., 2020). A large portion enters the Hau River downstream via the Vamn Nao River connection, after which the total discharge is almost equally distributed among both channels (Gugliotta et al., 2017) Binh et al., 2022).

From 1992 onward, large-scale hydro-power infrastructure has been put in place along the Mekong River. The effect of a changing climate and dam construction on river discharge on the Mekong's flow regime has been the subject of multiple studies (Binh et al., 2020)(Cook et al., 2012), (Lauri et al., 2012), (Lauri et al., 2012). After the construction of large reservoir lakes in 2001, a redistribution

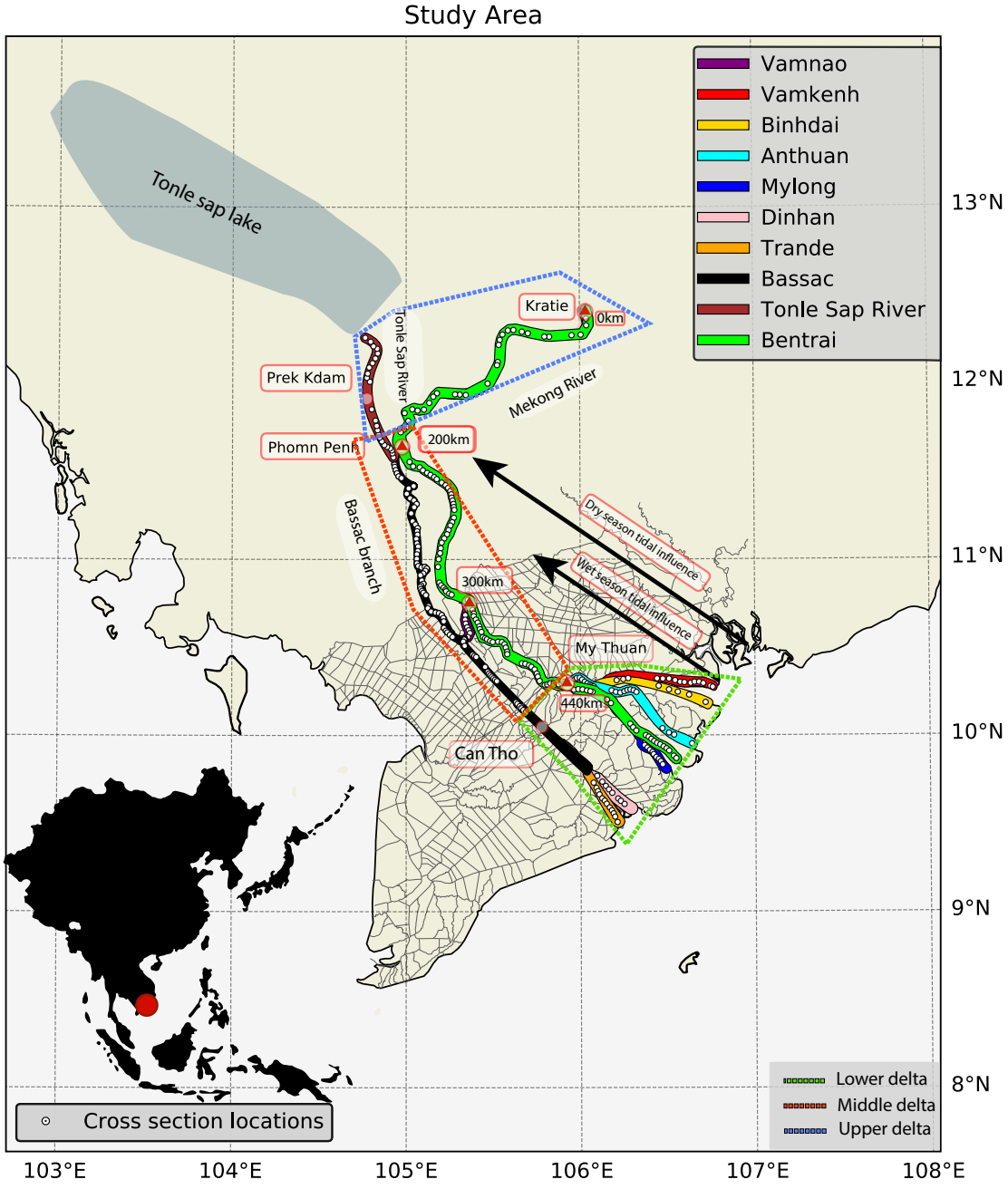

Figure 4.1: Study area. Grey indicates the canal network. The different branches defined for this study are indicated in the legend. The location of the observation cross sections is indicated as white dots. Arrows indicate the extent of the delta influenced by tides for both the wet and dry season (Gugliotta et al., 2017)

of flow between the wet- and dry season was measured as dams trap water during the wet season and release it during the dry season (Binh et al., 2020).MRC, 2017 shows that the wet season peak discharge is shifting towards later in the season as the lakes are filling up at the start of the season (Figure 4.3).

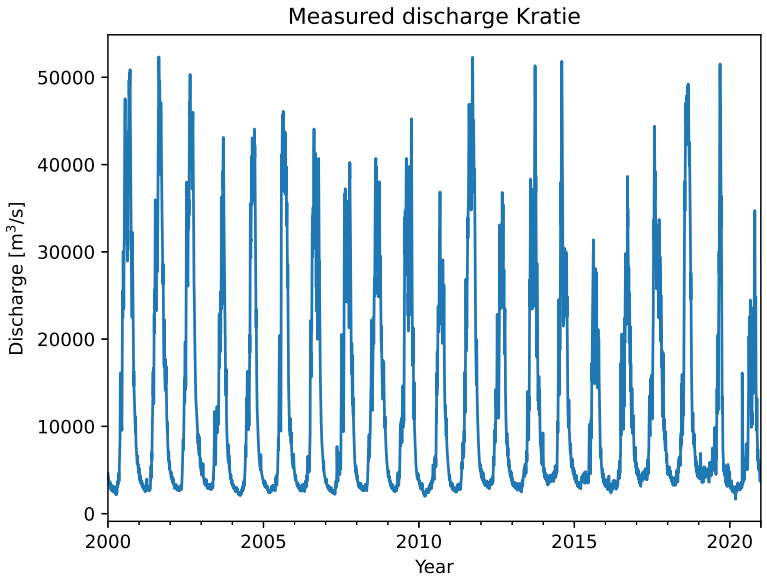

Figure 4.2: 20 years of measured daily discharge in the Mekong river at Kratie (MRC, n.d.)

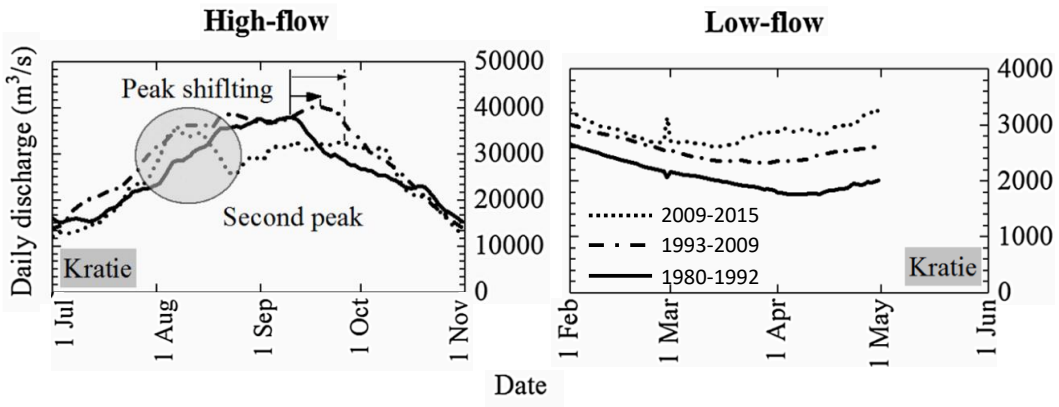

Figure 4.3: Long term alterations of the flow regime of the Mekong between 1980-2015 from Binh et al., 2020 at Kratie, Cambodia. The different markers indicate the different time periods. Here, due to the construction of dams, the peak discharge in the wet seasons shifts to a later period in the season. During the wet season, a clear increase in discharge is measured as water is redistributed over the seasons as dam operation causes water to be captured during the wet season and released during the dry season

Cook et al., 2012 and Lauri et al., 2012 simulated future discharge at Kratie for the period 2032-2042. It was found that the impact of climate change on discharge was highly uncertain. Changes in flow during the wet season range from -11 to +15%, and -10 to +13% for the dry season. The redistribution of flow over the seasons caused by dam operation was found to be of a larger influence on the flow regime for this time period, especially during the dry season, where a discharge of +25-160% was modelled.

4.2.2. Tonle Sap Lake

Tonle Sap Lake imposes a large influence on the hydrodynamics within the study area. Its catchment covers 85.790 km^2, which is 11% of the total Mekong basin (Barlow et al., 2003) while the permanent lake area is around 2400 km^2 during the dry season, where the water level is around 1.44m. During the wet season, water levels rise to 9.09m and the average lake area expands to 10.800 km^2 (Kummu and Sarkkula, 2008). Volumes of the lake vary between 1.8km^3 during the driest months and 58.3km^3 during the wettest months (Kummu and Sarkkula, 2008). Flow direction and magnitude in TSR are driven by its hydraulic gradient with the Mekong River. During the dry season, water levels are low and the lake discharges via the Tonle Sap River into the Mekong River. Discharge in this direction can reach up to 6000m^3/s at the start of the dry season and is greatest in shortly after the peak flow of the wet season. (Quoc Thanh et al., 2020). During the wet season, water levels at Phomn Penh rise up to 11m (Gugliotta et al., 2017). This results in the inundation of the floodplains on the west side of the Mekong River upstream of Phnom Penh. Via the floodplains, water enters the TSR. During this period, the Mekong River provides more than 50% of the annual inflow of the lake (Kummu et al., 2014). Average peak flow in the Tonle Sap river directed towards the lake can reach up to 8000m^3/s (Quoc Thanh et al., 2020). This results in a flattening of the peak discharge of the Mekong River downstream of Phnom Penh. Chua et al., 2022 estimated a drop in annual inflow from the Mekong River towards the lake from 48.7 km^3/y (averaged over 1962-1972)) to 31.74 km^3/y (2010-2018). Because of the flat topography around the lake, small increases in minimum water levels during the dry season result in a significantly larger permanently inundated area of the lake. Kummu and Sarkkula, 2008 estimated an expansion in the permanently inundated lake area of 2700-3200 km^2 increase for a 0.15-0.6m increase in minimum dry season water levels. Whether or not changes in the flow regime of the Mekong alter the hydrodynamics of TSL is under current debate. Wang et al., 2020 claims that Chinese dams have minimal impact on the inundation area of the lake and that the changes measured are mainly a result of changes precipitation. This was refuted in a response letter from Kallio and Kummu, 2021 that claims that precipitation plays a minor role and that the changes are mainly a result of upstream dam operation. Chua et al., 2022 claims that these changes were mainly attributed to local anthropogenic drivers such as water uptake in the Cambodian floodplains for irrigation and channel incision in the Mekong River.

4.2.3. Tidal characteristics

Water levels downstream of My Thuan are mainly dominated by tides from the East Sea Quoc Thanh et al., 2020 (Takagi et al., 2015). The average range of the mixed, semi-diurnal tide at the mouth is 2.2-2.6m (Wolanski et al., 1996)(Gugliotta et al., 2017) with a maximum of 3.2-3.8m. During the dry season, the tidal signal penetrates far into the delta (indicated in Figure 4.1). In this period, water level oscillation at centimetre to decimeter scale can be measured at Phomn Penh(Gugliotta et al., 2017), and tide-induced reversed flow occurs at the lower part of the delta (Ogston et al., 2017). Simulated flow volumes from (Binh et al., 2022) show maximum hourly discharge of −4780 m^3/s and −1850 m^3/s at Tan Chau and Chau doc respectively. The tidal amplitude inside the delta was found to increase by 2cm/y as water depths increase due to bed level incision (Eslami et al., 2019). The three different sections defined for this study area are based on the different hydrodynamic regimes described by Gugliotta et al., 2017. Here, an important distinction is made between the fluvial-dominated tract and the tide-dominated tract whose border is located at the My Thuan bifurcation.

4.3. General sediment dynamics

As the hydrodynamic regimes switch from a fluvial to a tide-dominated system (Gugliotta et al., 2017), sand transport mechanisms vary along the river. In the upstream part up to My Thuan, fluvial transport mechanisms mainly dominate (Gugliotta et al., 2017). In this region, the seasonal

Year	Location	Sediment load [Mt/yr]	Source
Last 3ka	VMD[1]	144 ±33.3	Ta et al., 2002
Predam	Mekong River[2]	160	Kondolf et al., 2014
Predam	VMD[3]	166.7±33.3	Binh et al., 2020
1993-2001	VMD[3]	68.41	Binh et al., 2020
1993-2001	VMD[3]	53.71	Binh et al., 2020
2008	Phomn Penh[4]	97	Lu et al., 2014
2009	Phomn Penh[4]	54	Lu et al., 2014
2010	Phomn Penh[4]	50	Lu et al., 2014
2012-2015	VMD[3]	43.1	Binh et al., 2020
2012-2015	VMD export[5]	40	Nowacki et al., 2015

Table 4.1: Estimated total sediment fluxes from the literature. [1]Total export sediment flux based on progradation rates retrieved from stratigraphies, [2]Total export sediment flux based on relation between river basin area and sediment yield.[3]Based on suspended sediment-discharge curve and discharge measurements at Chau Doc and Tan Chau. [4]Based on suspended sediment concentration field measurements [5]Interpolated based on water discharge distribution and suspended sediment measurements from Dinhan outlet.

variability in discharge translates to high seasonal variability in sediment transport rates. During the wet season, fluvial sediment transport- and seaward export rates are high. In this period, the suspended sediment concentration is high (50 to 300mg/l) across the delta (Wolanski et al., 1996) (Nowacki et al., 2015),(Gugliotta et al., 2017). During the dry season, sediment transport rates decline and only a small portion of the sediment load is transported during this period in this zone (Gugliotta et al., 2019).

Downstream of My Thuan, a tide-dominated system results in a more evenly distributed sediment transport load throughout the year. In the period with limited fluvial sediment supply, net transport at the Vamkenh, Binhdai, Anthuan and Mylong and Trande branches is directed land inward (Gugliotta et al., 2017) wheareas its directed seaward during the wet season. As the wet season sediment load exceeds the dry season load, net annual sediment transport is directed seaward (Xue et al., 2010), (Ogston et al., 2017). Of the total portion of sand coming in at Kratie, (Binh et al., 2022) estimated that 48-60% reaches the coast.

The annual sand volume transported has been in decline over the last decades due to sediment trapping of upstream dams (Anthony et al., 2015), (Bravard et al., 2013), (Brunier et al., 2014), (Lu et al., 2014). The construction of six mainstream dams in the upper Mekong Basin (also known as the Lancang cascade), resulted in an estimated 50-94% reduction in suspended sediment load in the lower Mekong River (Kondolf et al., 2014), (Manh et al., 2015). Another sixty-four dams resulted in a reduction of the suspended load by 74% inside the VMD (Binh et al., 2020). Kondolf et al., 2014 estimated that the total suspended sediment load would be reduced by 96% compared to the predam period (before 1993). Table 4.1 provides an overview of the estimated sediment loads from the literature. The reduced sediment availability from dams together with sand mining is causing a lowering of the river beds (Eslami et al., 2021), (Binh et al., 2021).

4.3.0.1.

Sand Although studies on sediment characteristics and transport inside the Mekong Delta are abundant, fewer have focused on the sand fraction. At Kratie, the total sand flux entering the Mekong Delta is 6.18 $\pm$ 2.01Mt/yr of which 0.18$\pm$ 0.07Mt/yr is transported as bedload. These estimates were made based on a relation between flow conditions, bed material and bedload transport constructed using observations made by repeat bathymetric surveys at six sites between Kratie en Phomn Penh between 2013 and 2014. Downstream of Kratie, measurements indicate that $\sim$ 7%

of the total suspended load contains sand (Hackney et al., 2020). The scarcity of survey sites introduces a higher degree of uncertainty to these estimates. Sand grain size measurements of the bed performed by Gugliotta et al., 2017 shown in Figure 4.4 display a fining seaward trend, where the last 150km displays an almost constant fine sand fraction. (Gugliotta et al., 2017). Sand trans-

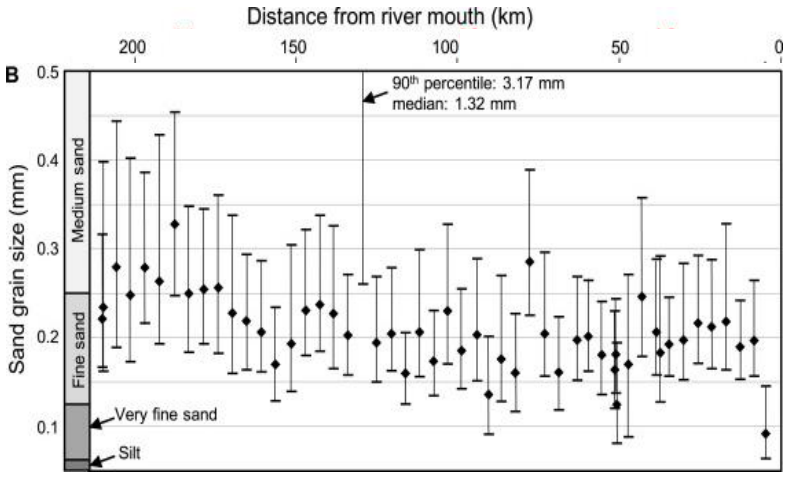

Figure 4.4: Sand grain size measurements of the bed from Gugliotta et al., 2017 for the 200km downstream part of the delta

port through the tidally influenced river section is primarily transported in the suspended load (Stephens et al., 2017). Bedload is transported in the form of propagating sand dunes on the river bed. In the river section where tides cause flow reversal, Allison et al., 2017 finds elongated ribbons of dune fields, which are especially distinct during the wet season, that suggest sand transport in the form of bedload present in these areas. Xing et al., 2017 studied sand transport mechanisms for both outlets (Dinhan and Trande) of the Hau River and found that both channels import sand landward during the dry season and export sand seaward during the wet season. Although field measurements from Gugliotta et al., 2017 have not measured sand import for these outlets. Studies that focus on the sand fraction in the Mekong Delta, have mainly focused on transport mechanisms on the most seaward side of the delta (Stephens et al., 2017), (Allison et al., 2017), (Xing et al., 2017) or on the effects of sand mining (Jordan et al., 2019), (Hackney et al., 2020), (Brunier et al., 2014). Until now, no delta-wide studies have been performed on sand transport processes in the Mekong Delta, which include both the river-dominated section of the Mekong and Hau rivers and the tidally dominated section at the mouth.

4.4. Anthropogenic drivers

4.4.1. Sand mining

Sand extraction from the river bed by mining practises is widespread along the Mekong River (Bravard et al., 2013), especially in Cambodia, where an estimated 60% of the total sand mining volume was extracted in 2011. In 2009, restrictions on sand export towards Singapore's land reclamation projects have been put in place by the Cambodian government. Vietnam followed the next year. These restrictions proved to be ineffective as mining practices boomed in the intervening years. This is partly attributed to the local sand consumption of the rapidly developing countries

and due to the inadequate enforcement of the restrictions put in place (WWF, 2018). Recent studies made to estimate sand mining volumes within the Vietnamese part of the Mekong range between 25 and 42Mm^3 Gruel et al., 2022, Jordan et al., 2019. These were based on bathymetric maps (Jordan et al., 2019) and sand mining vessel detection, using satellite imagery Gruel et al., 2022 (Figure 4.5).

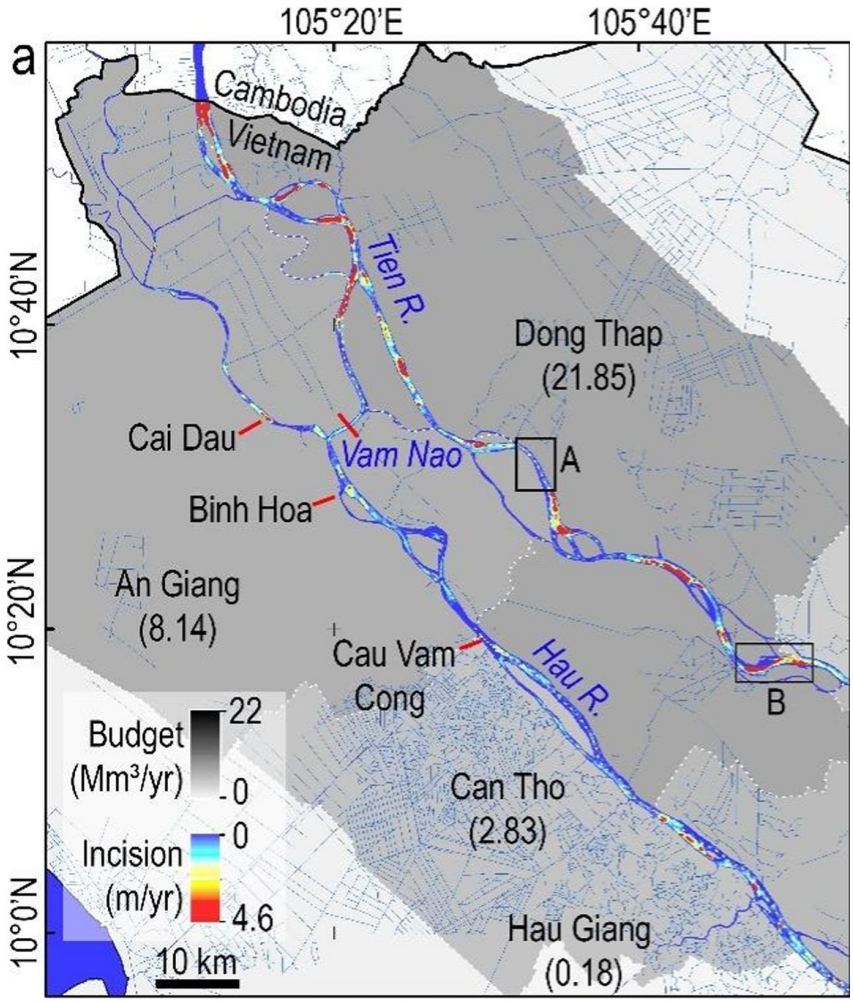

Figure 4.5: Incision rates along the Mekong River and the Bassac branch from Gruel et al., 2022.

Figure 4.6 shows the response of the river bed to sand mining by pit excavation. When sand is removed from the bed by pit excavation, two processes result in the incision of the river bed: head cutting and sand-depleted water ('hungry water'). Pit excavation results in increased water depth. As the cross-sectional area of the river increases the stream capacity of the river, causes flow velocities to decrease and deposition to increase locally. The sediment load will therefore decrease downstream of the mining site, resulting in increased erosion further downstream. This effect is also present downstream of dams (Abdulazeez, n.d.). Although sand mining is a local perturbation of the riverbed, the above-described processes cause the riverbed to incise almost evenly over a large area. Eslami et al., 2019 indirectly estimated a river bed lowering of the bed by 2-3m in the last 15 years, based on the increased propagation speed of the M2 tidal constituent. This equals a volume loss of 150-200Mm^3 per year. Which portion of this is attributed to sand trapping from the upstream dams or sand mining practices in Cambodia, Laos and China, remains unclear. As sand transport is slow, response to upstream dam construction and mining practices on sand availability inside the delta might still be absent. Furthermore, this estimate does not account for upstream

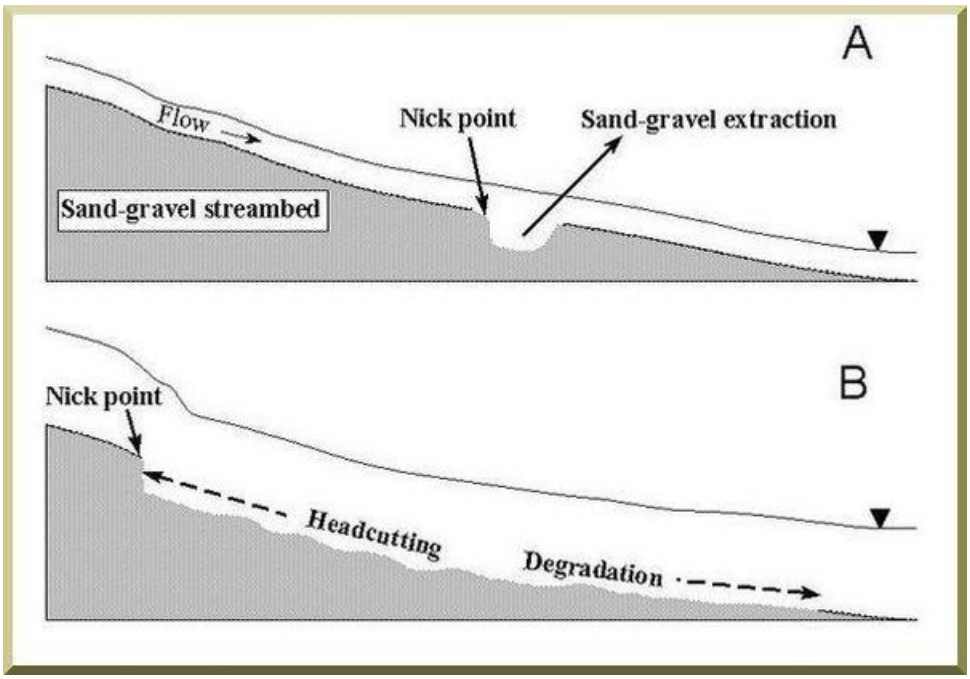

Figure 4.6: Effect of sand mining on bed morphology(Abdulazeez, n.d.)

sand mining practices in Cambodia, Laos and Thailand.

4.4.2. Subsidence and sea level rise

Sea level rise and subsidence both contribute to the high relative sea level rise the delta is experiencing. In the period between 1993 and 2008, SLR trends were in the order of 3mm/y (MONRE and Environment, 2016). Estimations on SLR for the year 2100 range between 26-59cm relative to the period 1980-1999, depending on the emission scenario taken. (MONRE and Environment, 2016). Figure 4.7 displays the trends for RCP 8.5 and 4.5 for the coming decades. Here, similar trends are seen up to 2035, where afterwards, RCP 8.5 starts to accelerate. Currently, human-induced land subsidence due to groundwater extraction is the main driver for relative sea level rise in the VMD and dwarfs sea level rise almost by an order of magnitude (Minderhoud et al., 2017). A growing agricultural, industrial and domestic groundwater demand, resulted in extraction rates increasing from 1986 onward. This accelerated subsidence rates up to 25 mm/yr, making it the main contributor to the delta-wide subsidence in the Mekong delta (Minderhoud et al., 2017). Future projections on subsidence rates for the VMD are based on policy scenarios (Minderhoud et al., 2020). Here it was estimated that increasing groundwater extraction by 4% every year would result in continuous subsidence up to 2078, with an average delta-wide rate of 12.9 mm y-1, with certain areas reaching rates up to 45mm y-1. On the other hand, if groundwater extraction is mitigated, future subsidence rates are also expected to decrease. In the case of an abrupt stop of groundwater extraction, average subsidence rates would drop to only 1.6 mm y-1 as a delta-wide average, with a maximum of 2.9 mm y-1. Therefore, the range in relative sea level rise (subsidence+sea level rise), is mainly dependent on future policy on groundwater extraction in Vietnam.

4.5. Goals of this study

Sand is of crucial importance for the VMD. When too much sand is extracted, large morphological changes are expected. Many of the problems inside the delta discussed previously reside from

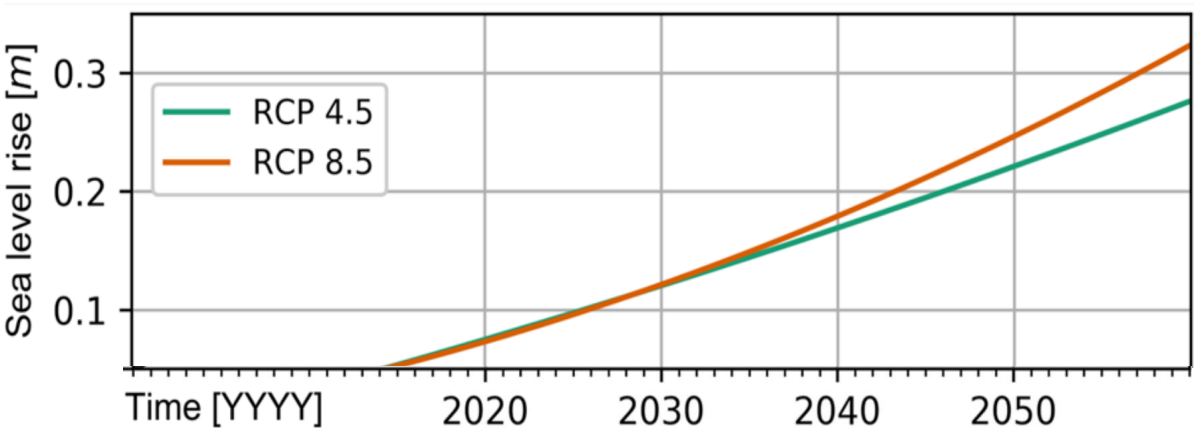

Figure 4.7: RCP 4.5 and RCP 8.5 SLR projections for the Mekong Delta. From Eslami et al., 2021

morphological changes inside the delta. It is therefore crucial to understand how much sand is transported in the delta and how this is influenced by changes system. The goal of this study is to provide an answer the following questions:

- To provide insight on the current system, the first question that needs to be answered is: How do the deltas current complex hydrodynamics drive the sand transport mechanisms inside the delta?
  - How is the water discharge distributed throughout the delta?
  - How does a highly seasonal discharge influence sand transport inside the delta?
  - What are the absolute sand transport rates throughout the delta?
  - What are the relative contributions of tidal and river currents on sand transport at different locations.
- Discharge alternation by dam operation, SLR, subsidence and the lowering of the river bed are ongoing and predicted future changes the delta is facing. Understanding how each separate actor contributes to changes in the deltas sand dynamics is useful for future policy making. To answer how the sand dynamics are impacted by each of these actors, the sensitivity analysis tries to answer the following question: What is the separate response of SLR, subsidence, river bed deepening and an altered discharge on the sand dynamics inside the delta. This is subdivided into the following questions:
  - How does the redistribution of discharge from the wet to the dry season affect sand transport in the delta?
  - What is the separate effect of SLR, subsidence and river bed lowering on sand transport?
  - How do the hydrodynamic changes explain the altered sand transport mechanisms for each of these perturbations?
- Since present-day changes in the deltas current morphology are happening on a yearly to decadal time scale, near-future predictions on sand dynamics will provide useful insight for policymakers. Therefore, the last goal of this study is to answer the following question: How are the 2040 sand transport mechanisms projected to change inside the delta? In order to encompass the uncertainty associated with predicting future sand dynamics, two 2040-scenarios have been incorporated: one extreme and one moderate. For each of these scenarios, the following questions are answered:

- What changes can be expected in sand transport rates for 2040, considering the current projections of discharge, river bed lowering, SLR, and subsidence? Specifically, how do these changes vary across the different hydrodynamic regimes within the delta?
- Are the results from the sensitivity analysis explaining the projected future changes in sand transport?

Chapter 5

Method

Until now, most studies focusing on sand in the Mekong Delta have used rough interpolation methods to quantify sand transport rates through the delta. This is mainly due to the lack of sand measurement data available for this region. To provide a detailed overview on current and future sand transport mechanisms inside the Mekong Delta, it was therefore decided to use a delta-wide, high resolution model to simulate the hydro- and sand dynamics throughout the delta.

5.1. General model description

In this study, hydro- and sand dynamics are modelled using DELFT3D FM (DFM) software developed by Deltares. The model set-up (grid, forcing, calibrated model parameters) were based on Q. V. Thanh, 2021 and further updated by Deltares. A more detailed description of the software is provided in Deltares, 2023.

5.1.1. Modelling principles

The model grid is displayed in Figure 5.1 and includes the Mekong River and all its tributaries from Kratie up to the mouth described in Section 4.1.. To include the river plume at the mouths, it extends for 80km over the shelf. The network of the main river channels and smaller canals definitions were retrieved from the 1-D hydrodynamic model (ISIS) from the Mekong River Commission (MRC).

The model integrates both 1- and 2D domains. The 2D domain contains the main branches of the Mekong River (Bassac branch, Vam Nao river, Tien River), the floodplains and the subaqueous delta. Water flow in the 2D-domain is simulated using depth averaged (2DH) shallow water equations, based on the finite volume numerical method described in Kernkamp et al., 2011. The smaller canals are modelled in 1D (Figure 4.1). How flow is modelled at transitions between the 1D and 2D domain is accurately described by Kernkamp et al., 2011.

To limit computation time where possible but, at the same time, capture the more complex, small-scale, processes, the 2D domain uses a spatially varying grid resolution. In the smallest channels and at channel junctions, grid cell resolution vary between 100-200 m, while in the main branches (Mekong River / Bassac branch / Vam Nao River) this is close to 700m. At sea and on the floodplains, coarser grid cells of 2000m are used. To follow the rivers path as accurate as possible, unstructured grid cells are implemented, including both triangular and curvilinear grid cells. For the 1D canals, the segments are uniformly separated at 400m.

As tides and river discharge are mainly governing sand transport, sand transport due to wave action at the seaward side is excluded. Also the effect of surges and wind have been excluded from the model.

The model applies the Van Rijn, 1993 sediment transport formulations, described in Deltares, 2023 (section 8.5.3). As the majority of the sand fraction is in suspension ($\sim$ 3%, Hackney et al., 2020) , and the model was unstable calculating bed load, the bed load fraction is treated as suspended load. This simulates sand transport according to 2D advection-diffusion (mass balance) equations:

$$\frac{\partial c}{\partial t} + \frac{\partial uc}{\partial x} + \frac{\partial vc}{\partial y} - \frac{\partial}{\partial x}\left[D_x \frac{\partial c}{\partial x}\right] - \frac{\partial}{\partial y}\left[D_y \frac{\partial c}{\partial y}\right] = 0$$

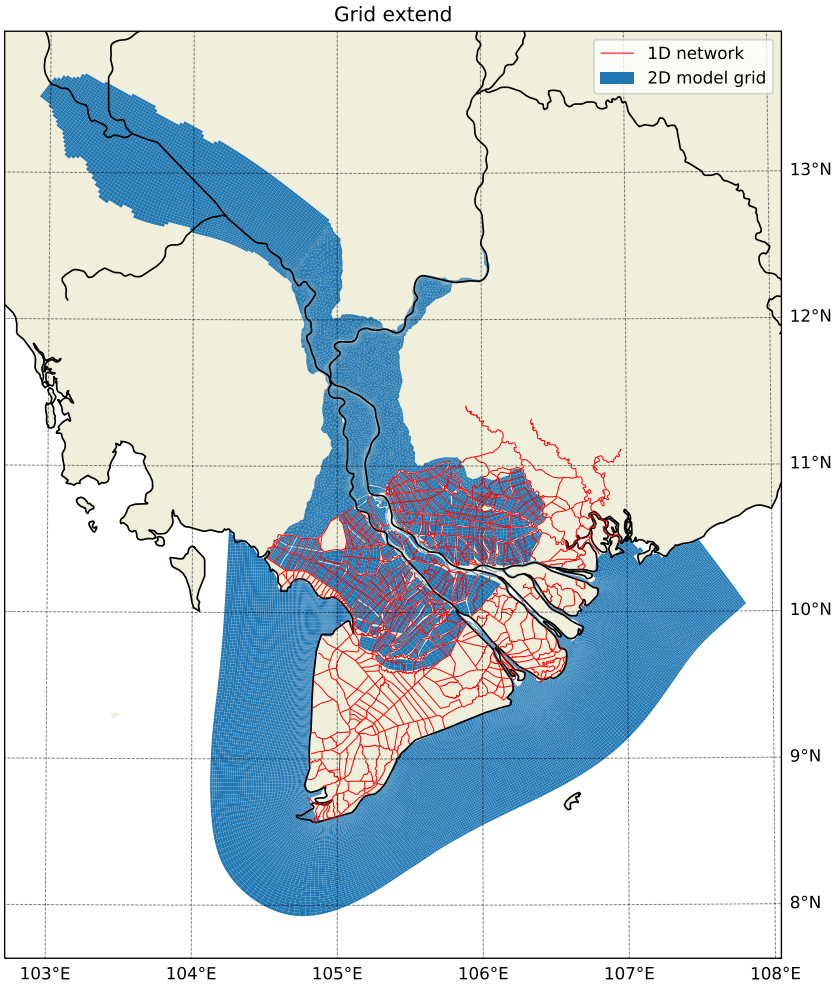

Figure 5.1: Model grid used in this study. The 2D model grid covers the main branches of the Mekong River (Bassac branch, Vam Nao river, Tien River), Tonle Sap River, Tonle Sap Lake, the adjacent floodplains and the subaqueous delta. The 1D domain contains an extensive network of canals present in the Vietnamese part of the delta.

Where: c is the mass concentration of the sediment (g/l) u and v are flow velocity components (m/s) D_x and D_y the diffusion coefficients in the x and y direction (m^2/s). The depth averaged sediment transport rate q_s is than calculated as function of the depth averaged flow velocity and depth averaged concentration. This includes the exchange of material in suspension and the bed is modelled as incoming (sink) and outgoing (source) fluxes from and to the bed.

$$-w_s c - D_z \frac{\partial c}{\partial z} = D - E$$

Where D_z depicts the diffusion coefficient in the z direction (m^2/s), $-w_s$ is the settling velocity (m/s), D and E the sediment deposition and erosion rates (kg/s). $-w_s$ is both a function of grain size and

concentration of sediment in the water column.

5.2. Calibration and validation

Hydrodynamic calibration and validation have been done by Deltares. This section outlines the key steps taken during this process.

5.2.1. Hydrodynamic calibration and validation

Initial roughness was extracted from Quoc Thanh et al., 2020 and Eslami et al., 2021. Further re-calibration was performed by spatially varying Manning's roughness coefficients in the 2D domain. Table 5.1 provides an overview of the different roughness values used for this study. For the 1D channels, a uniform roughness of 0.02 is used. Discharge and water levels were validated at six-

Location	**Manning**
Cambodian floodplains	0.042
Cambodian Mekong River	0.037
Tonle Sap Lake / River	0.032
Bassac branch Cambodia	0.039
Vietnamese floodplains	0.026
Vietnamese Mekong river	0.029
Bassac (Hau river) from border to Can Tho	0.026
Bassac outlets	0.024
Mekong outlets	0.026
East Sea	0.022

Table 5.1: Mannings's roughness coefficient used for different locations in the Mekong delta

teen different measuring stations in Cambodia and Vietnam. Model performance was tested with the Nash-Sutcliffe efficiency (NSE) formula NASH, 1970. Figures displaying the water levels and discharge measurements from 2022 against simulated data are displayed in the Appendix (A1). For all stations, an NSE higher than 0.5 was found, that, according to the classification of Moriasi et al., 2007, is considered as satisfactory. For water levels, at My Thuan, the lowest model performance is present. For discharge, this is at Chau Doc.

Due to the sparse data available on sand. No further calibration was performed on sand.

5.3. Model run overview

Table 5.2 provides an overview of the different model runs performed in this study. The different model runs are done to research three main topics: 1) Current sand dynamics; 2) separate response in sand dynamics under a changed discharge, SLR, subsidence and river bed lowering; 3) 2040 projections in sand dynamics for an extreme (CC85B2RB3) and a moderate scenario (CC45M2RB1). Each run has been done for one year using a spin-up time of 14 days starting on the 1st of May (start of the wet season).

5.4. Model input for this study

To investigate current and future sand dynamics in the Mekong Delta, this study modified the following variables: Bathymetry/topography, discharge boundary conditions, SLR, and sand proper-

Name	Subsidence	Mean sea level	River bathymetry	Discharge
Present-day	Present-day	Present-day	Present-day	Present-day
50cm SLR	Present-day	+0.5m	Present-day	2040
50cm Subsidence	-0.5m	Present-day	Present-day	2040
50cm RB	Present-day	-0.5m	Present-day	2040
2040 discharge	Present-day	Present-day	Present-day	2040
CC45RB1M2	M2 Minderhoud et al., 2020	+0.116m Eslami et al., 2021	-1.0m Eslami et al., 2021	2040 discharge MRC, 2017
CC85RB3B2	B2	+0.194m Eslami et al., 2021	-3.0m Eslami et al., 2021	2040 MRC, 2017

Table 5.2: Model run overview. Subsidence from Minderhoud et al., 2020 displayed in Figure 5.4. Discharge for present-day and 2040 displayed in Figure 5.3. Present day river and delta bathymetry are elaborated in Table 5.3 and Section 5.4.1.

ties. Pre-process scripts from Eslami et al., 2021 have been provided to modify the bathymetry/topography and SLR. Table 5.3 provides an overview of the input data used in this study.

Data type	Source	Description
*Bathymetry data river*s	Vasilopoulos et al., 2021, (WWF),	Interpolated and incorporated by Eslami et al., 2021, varying resolution
Bathymetry data canals	MRC	From 1D-ISIS model, 400m resolution, Constructed in 1998, updated in 2015 by Quoc Thanh et al., 2020
Bathymetry offshore	ETOPO	1km resolution
Floodplain topography	MRC	DEM of 250m resolution
Discharge at Kratie	MRC, n.d.	20-year daily discharge data from Kratie measuring station (Figure 4.2)
2040 discharge	MRC, 2017	Monthly changes in discharge for 2040 from MRC, 2017
Subsidence rates	Minderhoud et al., 2020	Delta wide subsidence according to the B2 and M2 scenario
SLR	Anh et al., 2018	SLR according to RCP4.5 and RCP8.5
River bed lowering	Eslami et al., 2021	Channel deepening according to RB1 (-1.1m) and RB3 (-3.3m) scenarios

Table 5.3: Data overview table

5.4.1. Topography and Bathymetry

Since bathymetry data for the Mekong Delta is sparse, the incorporated bathymetry of this study is composed from different sources and time periods. This study uses the in 2018 measured bathymetry from Vasilopoulos et al., 2021. In several areas in the Mekong River in Vietnam, this is updated using bathymetry data collected in 2022 by The World Wildlife Fund. The bathymetry of the river mouths was updated following Eslami et al., 2021. The upstream bathymetry, especially in the Cambodian section, is outdated and of lower resolution compared to the bathymetry at the mouth. Further in this research, this proved to affect the results on the annual sand transport quantities. The floodplain topography contains a digital elevation model of 250m resolution from the MRC. Offshore, the bathymetry was obtained from ETOPO (1km resolution).

5.4.1.1. Interpolation of bathymetric data

In parts of the 2D channels, river bathymetry measurements were linearly interpolated. Detailed reasoning for this interpolation method is described in V. Q. Thanh et al., 2020. Since a river bathymetry is more variable in the across-flow direction than in the along-flow direction, another correction for the along flow trends in bathymetry was performed by V. Q. Thanh et al., 2020. This proved to be useful in interpolating the geometry of the thalweg and the river banks. In the downstream areas,

5.4.1.2. 2040 Topography/bathymetry

To incorporate the effects of sand mining (and potential sand trapping by upstream dam construction), the river bed of the main channels is uniformly lowered throughout the delta, leaving the bank and floodplain elevation unchanged (Figure 5.4). For the sensitivity study the bed is lowered by 0.5m. In the future scenarios, channel incision rates from Eslami et al., 2021 were used. The RB3 scenario from Eslami et al., 2021 is incorporated as a -3.3m (0.15m/y, total 3Gm^3 eroded) lower riverbed in 2040 compared to 2018. For RB1 this is -1.1m (0.05m/y, total 1Gm^3 eroded) (figure 5.4). Only around Can Tho, no significant river bed changes have been estimated Eslami et al., 2019 or measured Allison et al., 2017. Therefore, in this region, bed level was not changed. To study the sensitivity to subsidence, a constant delta wide lowering of 0.5m was implemented. For the future scenarios the M2 (mild) and B2 (extreme) scenarios from Minderhoud et al., 2020 are incorporated. These subsidence scenarios are based on future groundwater extraction projections. B2 represents the worst-case scenario, where daily groundwater extraction is increased by 4% every year. M2 represents a mitigation scenario, where groundwater extraction is reduced at a rate where the present hydraulic head is maintained in the delta. Based on these spatially varying subsidence rates, the total subsidence for 2040 relative to 2018 was calculated throughout the delta (Figure 5.4). As subsidence due to groundwater extraction is a delta wide process, both river bed and the adjacent banks, floodplains and canals are lowered due to this.

5.4.2. Hydrodynamic boundary conditions

5.4.2.1. Upstream river boundary conditions

Present day discharge The upstream discharge boundary is located at Kratie. Here an annual hydrograph containing daily averaged discharge data is defined. A hydrograph that is representative for the present day situation is constructed based on daily average discharge measurements between 2002 and 2021 provided by MRC, n.d. To avoid seasonal over- and underestimations in total discharge volumes, total discharge volumes for both wet- and dry season were calculated and compared for every year between 2002 and 2021 (Figure 5.2). The orange line in Figure 5.2 indicates the mean total discharge between 2000 and 2020 for the wet season and between 2001 and 2019 for the dry season. For the dry season, the year 2001 and 2015 approaches this mean, for the wet season 2004 and 2014. For both cases, the most recent year is picked (figure 5.3). The representative hydrograph therefore starts with the 2015 dry season and is followed by the 2014 wet season.

2040 discharge Discharge projections from MRC MRC, 2017 were used to construct a 2040 discharge. In the MRC study, dam development and a wide range of climate models are incorporated in their future discharge estimations. In MRC, 2017 average monthly changes in discharge for 2040 are presented. The constructed present day discharge (described above) is modified according to these monthly changes for 2040 (Figure 5.3) (blue line). The resulting 2040 hydrograph includes the projected shift in peak discharge described in the background. Furthermore, a redistribution of discharge is included, as the total discharge volume during the wet season was decreased by 18% while during the dry season, this increased by 12%.

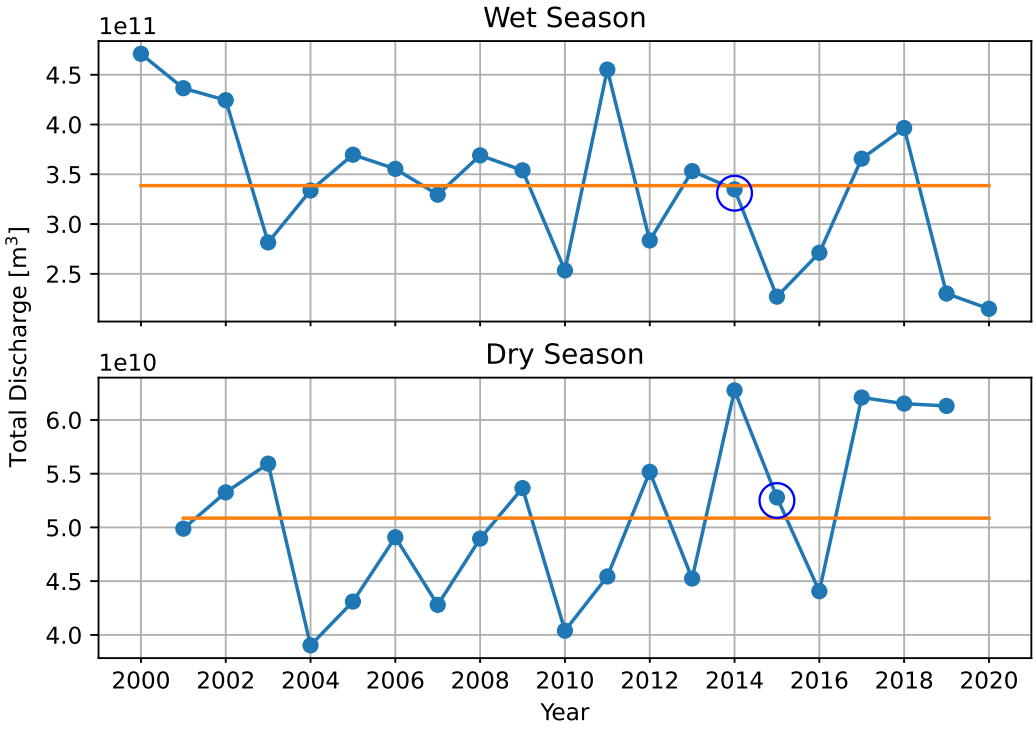

Figure 5.2: Cumulative discharge for the wet and dry seasons at Kratie. The orange line indicates the 20-year mean for each season

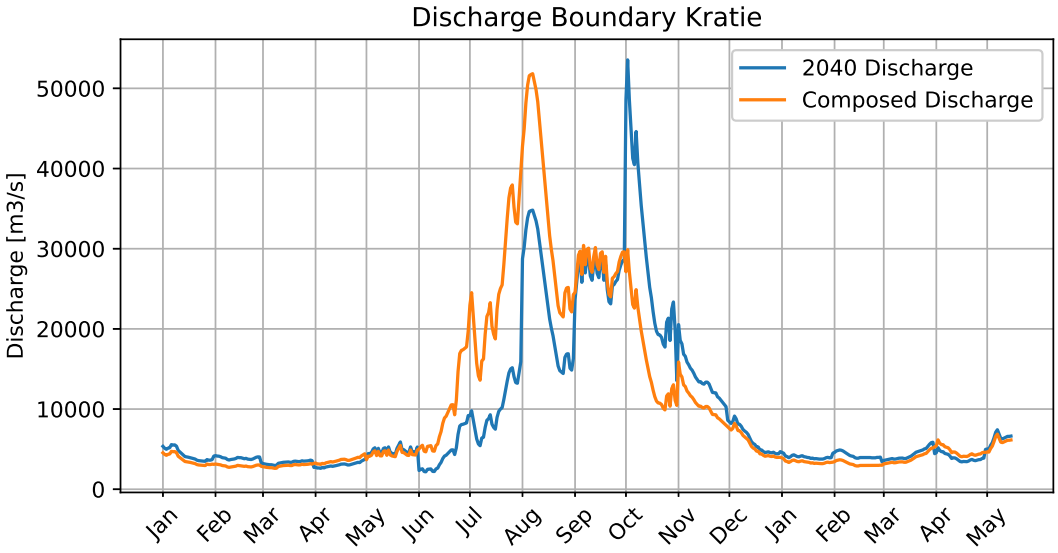

Figure 5.3: The discharge boundary at Kratie is used for present-day (orange) runs and future (blue) runs

5.4.2.2. Seaward boundary conditions

At the ocean side, astronomical tidal constituents (M2, S2, N2, K2, K1, O1, P1, Q1) were prescribed on the shelf as water level variation. Amplitude and phase are extracted from a global tidal model Egbert and Erofeeva, 2002. To account for cross-shore transport, water level gradients according to Neumann were prescribed for cross-shore transects. Projected sea level rise from Anh et al., 2018 was used to construct both RCP 4.5 (moderate 12cm), and RCP8.5 (extreme, 19cm). Variation in tidal forcing at the shelf due to SLR were tested but showed very limited variation and is thus assumed constant for future projections.

5.4.3. Sand boundary conditions

Due to a lack of sand transport measurements open Neumann boundaries were defined at Kratie and at sea. Here, the gradient of the concentration is specified normal to the boundary ($dc/dn = 0$). This allows a near-perfectly adapted flow, preventing high accretion or erosion rates at the inflow boundary.

5.4.3.1. Sand properties

A uniform bed of 10m thickness is defined for every channel. Although no morphological updates were considered, changing sand availability in the bed was accounted for by the model. A single grain size of 200μ is chosen based on the findings of Gugliotta et al., 2019, displayed in figure 4.4. In order to test whether fundamentally different processes occurred for other grain sizes, the model is run for very fine (62μ) and coarse sand (1500 μ). While transport volumes drastically differed, no large differences in transport mechanisms occurred. For the sake of brevity and time, it was decided to only include 200μ in the model runs.

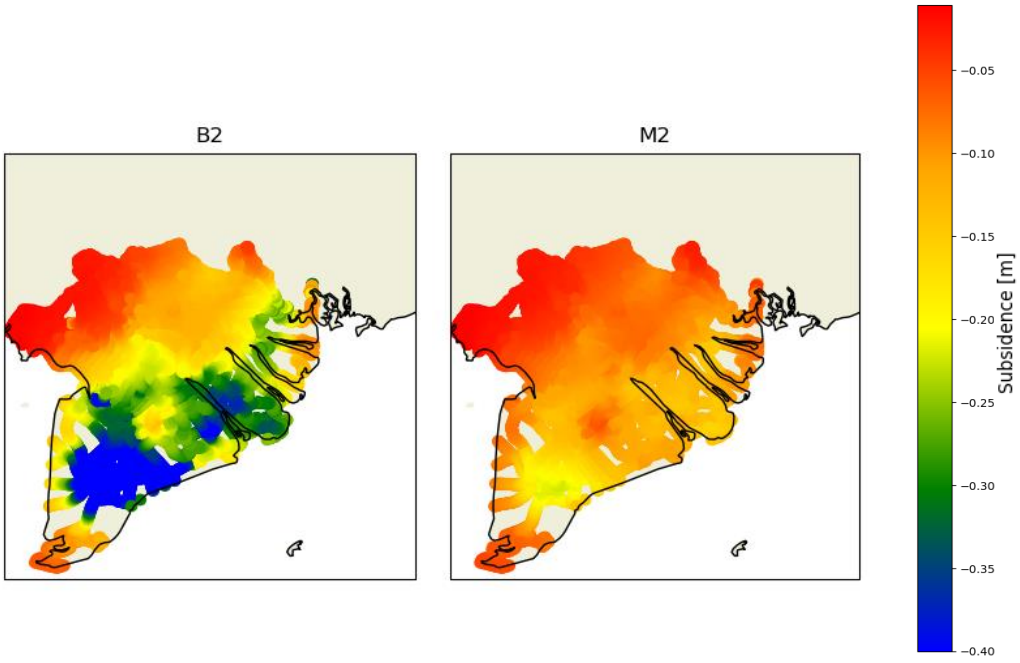

Figure 5.4: River bed lowering (RB) location, and adjusted bathymetry compared to the 2018 bathymetry from Q. V. Thanh, 2021 in meters for scenarios B2 (worst-case) and M2 (mitigation) from Minderhoud et al., 2020 for 2040

5.4.4. Model output and post-processing

In the 2D branches, cross sections were defined for every 2-4km. The cross-section is taken over the total width of the channel and its shape and area are determined by the geometry of the river at that location and the time-varying water level. Observation points to obtain water heights and water depths were placed inside the thalweg of the Mekong River from Kratie up to Bentrai. At bifurcations, where river islands are formed, no cross sections were placed in the separate branches, as this would complicate results due to the variability in discharge in each of these branches.

Model data output at cross sections includes (cumulative) discharge-, (cumulative) sand transport volumes and depth average flow velocities ($U = Q/A$). Volumes of sand were converted to masses using a density of quartz (2650 kg/m^3). Figure 4.1 displays the locations of the cross sections and names for each of the branches used in this study.

In this study, tidal analysis is performed using the Hatyan tool from Deltares, for further documentation consult “GitHub - Deltares/hatyan: Harmonic tidal analysis and prediction”, n.d. Tidal signals were filtered using a Godin filter function Godin, 1972 from the open earth toolbox “OpenEarth”, n.d., which was converted from MATLAB to Python for this study. This filter allows to depict the 24h-tidally averaged sand transport rates or flow velocity by applying multiple filter windows of different durations (24/25 hours) to the input data set. It calculates the mean value within each window, progressively filtering out the tidal component of the data.

To display the results, transects are plotted where distances are calculated from Kratie (x=0) up to the mouth (distance at the mouth varies for every outlet). Here, the distances between every next point, starting from Kratie and going downstream, were summed consecutively.

Chapter 6

Results

6.1. Present-day setting

To understand how the present-day complex hydrodynamics drive the sand transport mechanisms inside the Mekong Delta, both subjects are discussed separately in this section. The first part of this section is therefore committed to providing an overview of the present-day hydrodynamics inside the delta. The second part uses this insight and connects this to the present-day sand transport processes present in the delta.

6.1.1. Hydrodynamics

6.1.1.1. Discharge distribution

Figure 6.1 depicts the discharge distribution through the delta. At Kratie, an annual total discharge of 400Gm^3 is defined. At the Phnom Penh confluence (PPC), around 8% of the Mekong's annual water budget is contributed to the Bassac branch. Further downstream almost one-third (120Gm^3) of its total discharge flows through the Vamn Nao River to the Hau River. At the mouth, the smaller estuaries, Vamkenh, Binhdai, Anthuan and Mylong discharge 2.8%, 6.8%, 10.25% and 6.5% of the annual incoming discharge at Kratie. The larger estuaries are the Bentrai, Dinhan and Trande outlet, that discharge 16.5%, 32.5% and 16%.

6.1.1.2. Hydrodynamic parameters

Figure 6.2 shows water levels (WL), cross-sectional area (A), discharge (Q), (maximum and minimum) flow velocities (U) and the tidal velocity and water level amplitudes of the main tidal constituent M2 along the Bentrai transect from Kratie (x=0) up to the mouth (x=550) (lime branch in Figure 4.1). August is chosen to represent the peak discharge in the wet season. To represent the dry season discharge, February is chosen (Figure 5.3 orange line). Hourly output is plotted to display the range of values within each month.

The mean discharge in August at Kratie is around 30.000m^3/s (Figure 6.2A). The hourly output for this month ranges between 20.000 and 50.000m^3/s. This is a result of the varying discharge during this month (Figure 5.3). In February, a mean discharge of 5000 m^3/s is defined.

Along its flow path, water leaves the Mekong to connected branches at the Bassac bifurcation at Phnom Penh (200km), Vamn Nao river bifurcation at 300km and the My Thuan bifurcation at 440km (locations indicated in Figure 4.1). While discharge up to the Bassac bifurcation (200km) shows a high discrepancy for both months this difference is less distinct in the lower reaches. At Phnom Penh, the buffering effect of Tonle Sap Lake can be noted. Here, the variability in hourly discharge output for August suddenly drops from 35,000-18,000 m^3/s to 26,000-16,000 m^3/s. This means that, for a discharge of 35.000 m^3/s upstream of Phnom Penh, about 9,000 m^3/s is lost from the Mekong River here. A portion of this ends up in the Bassac branch (Figure 6.1) but most of it flows through the Tonle Sap River (TSR) towards Tonle Sap Lake (TSL). This is shown in Figure 6.3 that depicts the simulated discharge time series of TSR at Prek Kdam. In August, discharge values towards TSL of up to 10,000 m^3/s can be seen. From October onward, the flow direction reverses and the TSR contributes an almost constant discharge to the Mekong River during the dry season. Water levels (Figure 6.2A) for the Cambodian section / Upper Delta (0-300km) are twice as high in August compared to February. In this region, the range in water levels in August is attributed to

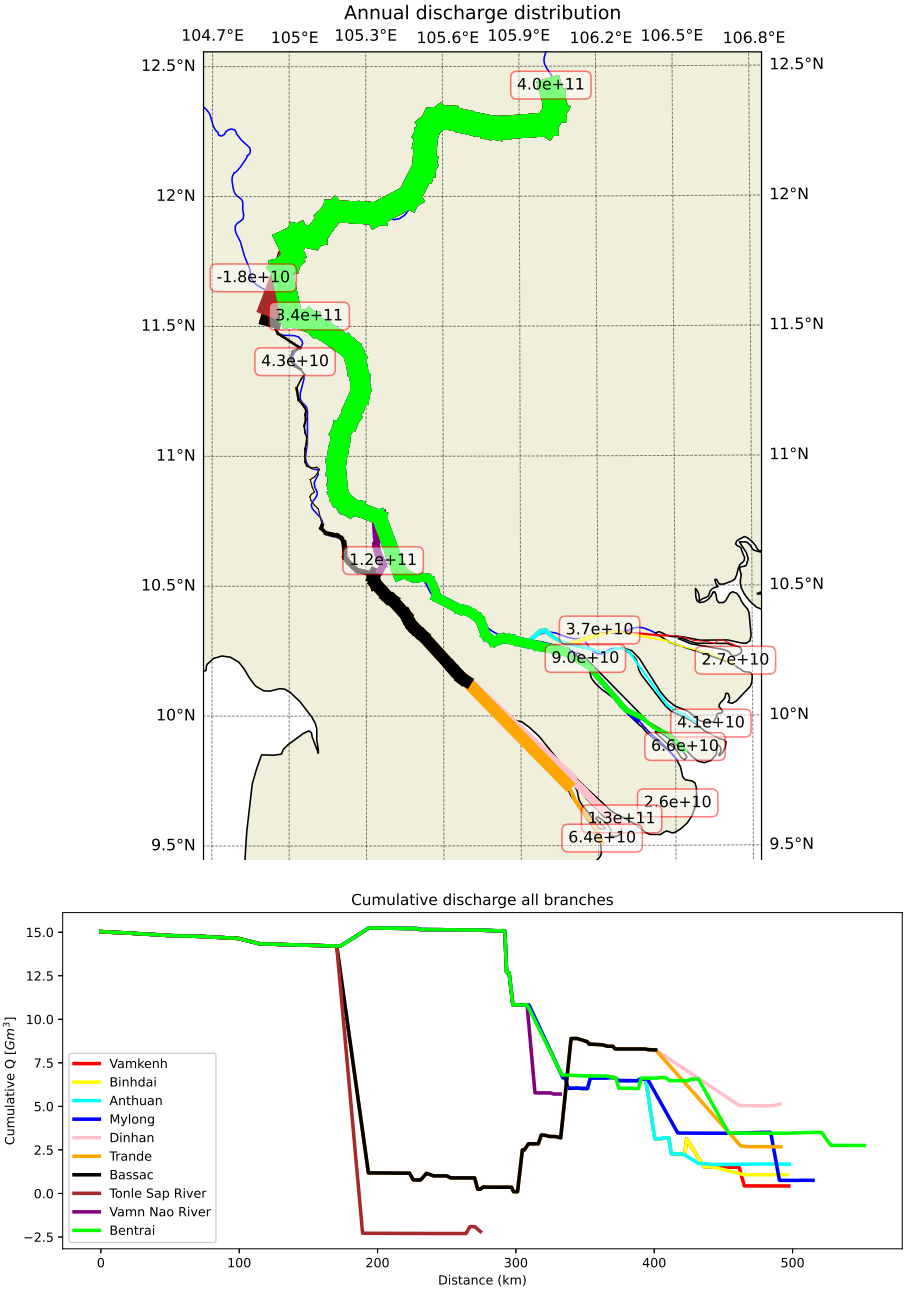

Figure 6.1: Discharge distribution through the VMD. The numbers indicate cumulative discharge in [m^3] for one year. The coloured lines indicate the different branches defined in this study, where the line thickness is indicative of the relative cumulative discharge compared to incoming discharge at Kratie. In the lower graph, absolute discharge fluxes are plotted for each branch where each colour indicates the branch. Distances on the x-axis are calculated from Kratie (x=0) up to the mouth for each branch.

the range in discharge variation in this period. Downstream of the Vamn Nao bifurcation (300km), the delta's topography flattens and along channel water level gradients drop to almost zero. In the Lower Delta (>440km), variation of the seasonal discharge has only marginal effects on the water levels as these are predominately regulated by tides.

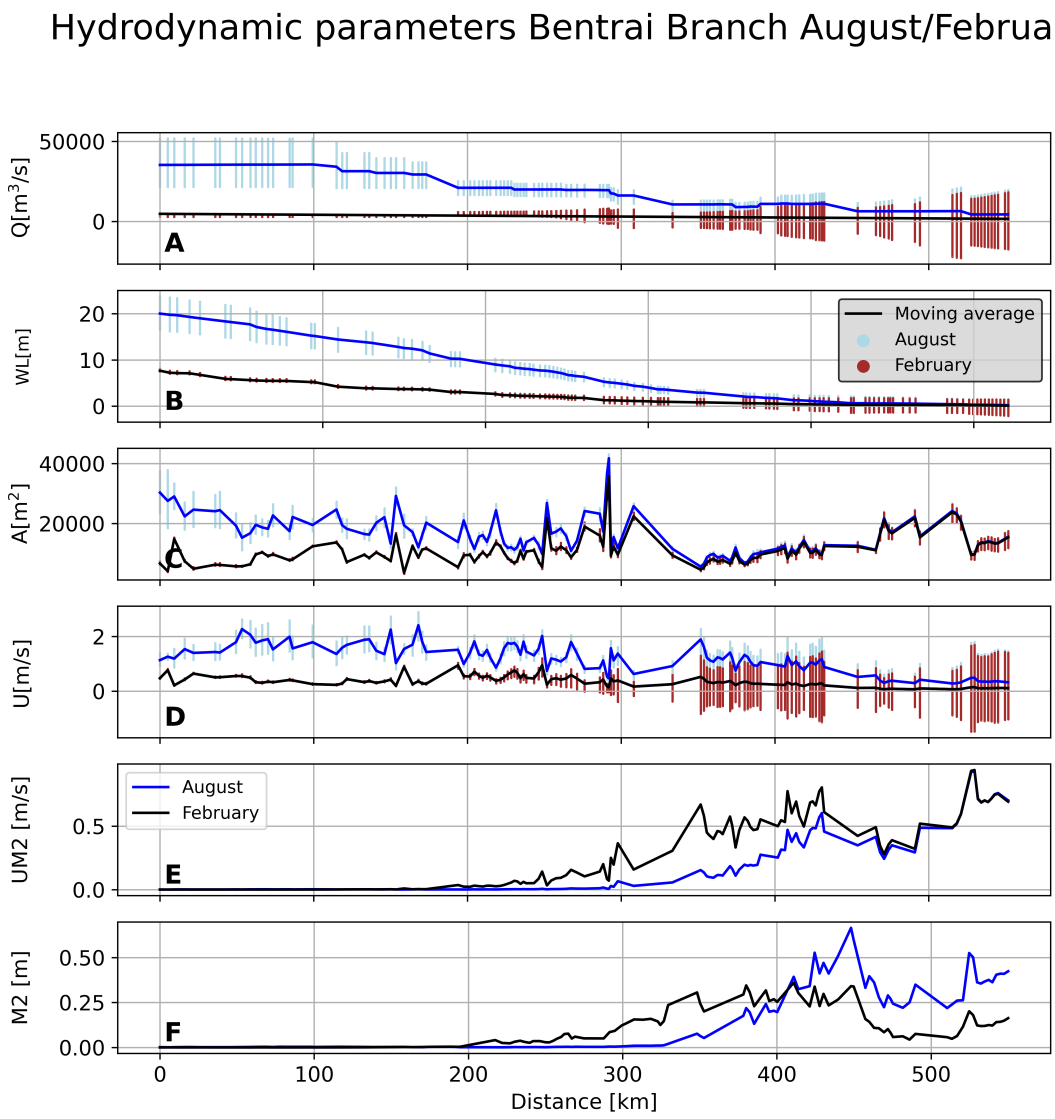

Figure 6.2: A) Discharge (Q), B) Water levels (WL), C) cross-sectional area (A), D) flow velocities (U), E) Flow velocity amplitude M2 tide, F) Water level amplitude M2 tide. Transect is taken from Kratie (x=0) via the Mekong River up to the Bentrai outlet (x=550) (lime in Figure 6.1) for all hourly output in August (light blue, wet season) and February (brown, dry season). The blue (August) and black (February) lines in each panel indicate the mean values for the hourly output of both months. Tidal signals shown in panels E & F are based on a one-month harmonic analysis.

The mean cross-sectional areas displayed in Figure 6.2C) shows high local variability. This is especially true for the Cambodian section (0-300km). This can be attributed to the lack of measurement data present in this region, resulting in incorrect interpolation between the measured data points. After the Vam Nao bifurcation at 300km, the river's channel cross-sectional area declines as the river becomes narrower. Note the slight increase after the My Thuan (at 440km) as the river widens again after the bifurcation. The decrease in cross-sectional area at 520km marks the Mylong/Bentrai bifurcation.

As mean discharge is relatively constant for the Cambodian section (0-300km), the high local vari-

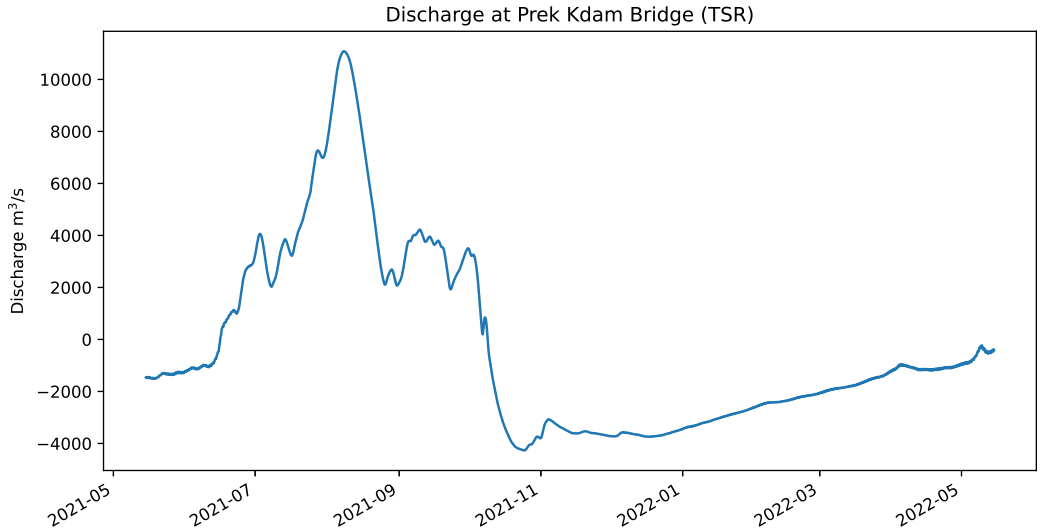

Figure 6.3: Discharge at Prek Kdam Bridge (Cambodia). Negative values indicate flow directed towards the sea, while positive values indicate flow directed towards TSL.

ability in mean cross-sectional areas drives local flow velocity variations (since $U = Q/A$). In this region, large discrepancies in mean flow velocities between both months can be seen. In August, flow velocities in this section are mainly around 2 m/s, while in February this is less than 1 m/s. Variation in the hourly output in the Upper Delta in August is attributed to the varying discharge at Kratie during this month (Figure 6.9A&B .

From Figure 6.9E, it can be seen that the M2 signal penetrates up to Phnom Penh (x=200km) in February and up to the Vamn Nao bifurcation (x=300km) in August. This is also depicted in Figure 6.2E which shows the water level amplitudes of the main tidal constituent M2. In Figures 6.2E & F, large tidal velocity and water level amplitudes are shown at My Thuan (440km). Here, convergence is strong as the river narrows in a landward direction between 450 and 350km.

Figure 6.4 shows the mean peak ebb and flood velocities from Phnom Penh up to the mouth for both months. Mean peak ebb velocities are directed landward from 320km onward in February. In August, mean peak ebb velocities are landward from 490km onward.

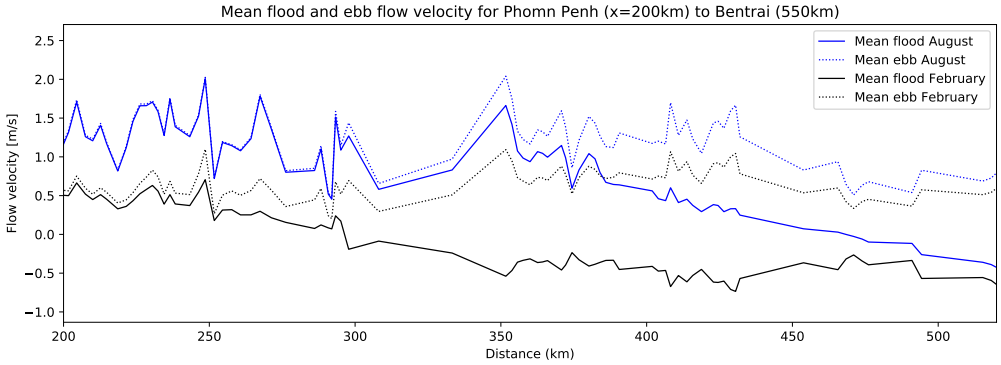

Figure 6.4: Mean flood (solid) and ebb (dotted) currents for August (blue) and February (black) from Kratie (x=0) via the Mekong River up to the Bentrai outlet (x=550km). Means were calculated by averaging the peak flood and ebb flows for one each month at every cross-section.

6.1.2. Sand Dynamics

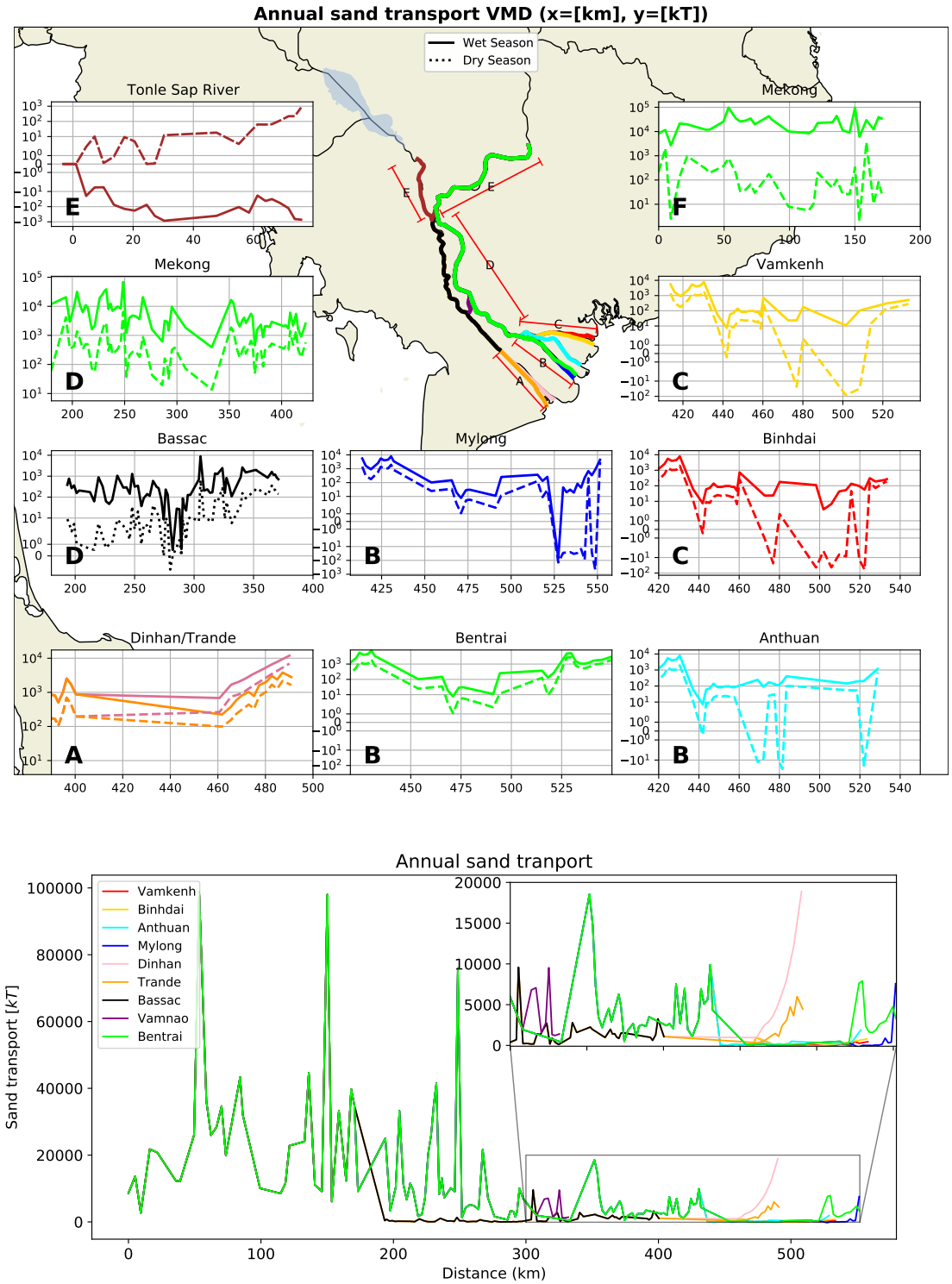

Figure 6.5: Wet season (solid) and dry season (dotted) total transport volumes for each branch. Distances are calculated from the most upstream location in Cambodia (Kratie). Distance 0 for TSR is at TSL. Sand transport quantities indicated in the graphs are in [kT] and positive in the seaward direction. The lower figure compares the annual sand transport volumes for each branch.

Figure 6.5 depicts cumulative sand transport in kT for both the wet and the dry season. In the graph from Figure 6.5, annual sand transport volumes for the whole year are plotted. To show the sand transport trends and directions (landward or seaward) present in the delta, sand fluxes are plotted logarithmic scale. To better compare the different quantities of sand transport present inside the delta, the lower graph and Appendix Figure 9.5 show the absolute sand transport values.

Within the study area, large spatial differences in annual sand transport occur. At the Cambodian section, annual transport in the range of 20-40Mt (with outliers up to 100Mt) is modelled where sand transport volumes during the wet season outnumber those of the dry season by an order of magnitude. From the graph below, it can be seen that local variability in net annual sand transport is extremely high in this region.

The TSR transect shows sand transport directed towards the lake during the wet season but only a limited amount leaves the lake during the dry season (Appendix Figure 9.5). Therefore, on an annual basis, the lake imports sand.

Downstream of Phnom Penh (200km), sand transport volumes for the Mekong (transect B, lime) are significantly higher than for the Bassac branch (transect B, lime). This follows the discharge distribution presented in Figure 6.1.

In the lower estuaries, sand transport during the wet season decreases by one or two orders of magnitude compared to the upper delta. The smaller estuaries Binhdai, Vamkenh, Mylong and Anthuan show landward sand transport during the dry season, while the estuaries that receive a larger fraction of the total discharge (Bentrai, Trande, Dinhan) show net seaward sand transport for both seasons. The opposing directions of sand transport for both seasons in the smaller estuaries result in small seaward transport volumes on a yearly basis, which are negligible compared to the annual sand transport volumes in Cambodia.

As sand transport in the estuaries is directed landward during flood tide and seaward during ebb tide, tidally averaged sand transport rates are calculated using a Godin filter (see method). Figure 6.6 shows filtered (blue) and unfiltered (orange) time series of the sand transport rates for three locations in the delta. The figure indicates the seasonal character of sand transport at Phnom Penh. At My Thuan, this seasonality in sand transport declines while at Bentrai, the seasonal character has almost vanished as sand transport rates are similar for both seasons. Here variation in sand transport rates are mostly governed by the tides. Sand transport rates at Phnom Penh reaches more than 4m^3/s during the wet season, while during the dry season, it approaches 0m^3/s. At My Thuan sand transport rates are significantly lower, with a peak rate of 0.5m^3/s during the wet season. In order to illustrate the tidally averaged sand transport rates present in the lower estuaries, Figure 6.7 displays the Godin filtered sand transport rates ($< q_s >$) from Figure 6.6 for all Tien river estuaries after My Thuan. Between 440 and 520km, only very small tidally averaged sand transport rates are present, with values ranging between 0.01 m^3/s and -0.01 m^3/s for both months. Close to the mouth, higher sand transport rates of 0.1-0.2 m^3/s and of 0.05-0.1 m^3/s can be found for the Bentrai branch (lime) and the Mylong branch (blue) respectively. In October, net sand transport rates are mainly directed towards the sea, while in February, the smaller estuaries show overall negative (or landward) sand transport rates.

When comparing the graphs in Figure 6.5 and Figure 6.7 to the cross-sectional area plotted in Figure 6.9C, it becomes apparent that the significant fluctuations in sand transport rates primarily stem from the variations in cross-sectional area. This observation highlights the remarkable sensitivity of sand transport to changes in flow velocity caused by alterations in the river channel geometry. Given the substantial variability observed among neighbouring measuring locations, it can be concluded that sand does not remain suspended for a long period. The characteristics of sand transport differ significantly from the patterns observed in the discharge shown in Figure 6.2. When flow velocities are high, sand is transported locally, but it quickly settles once the flow velocities decrease.

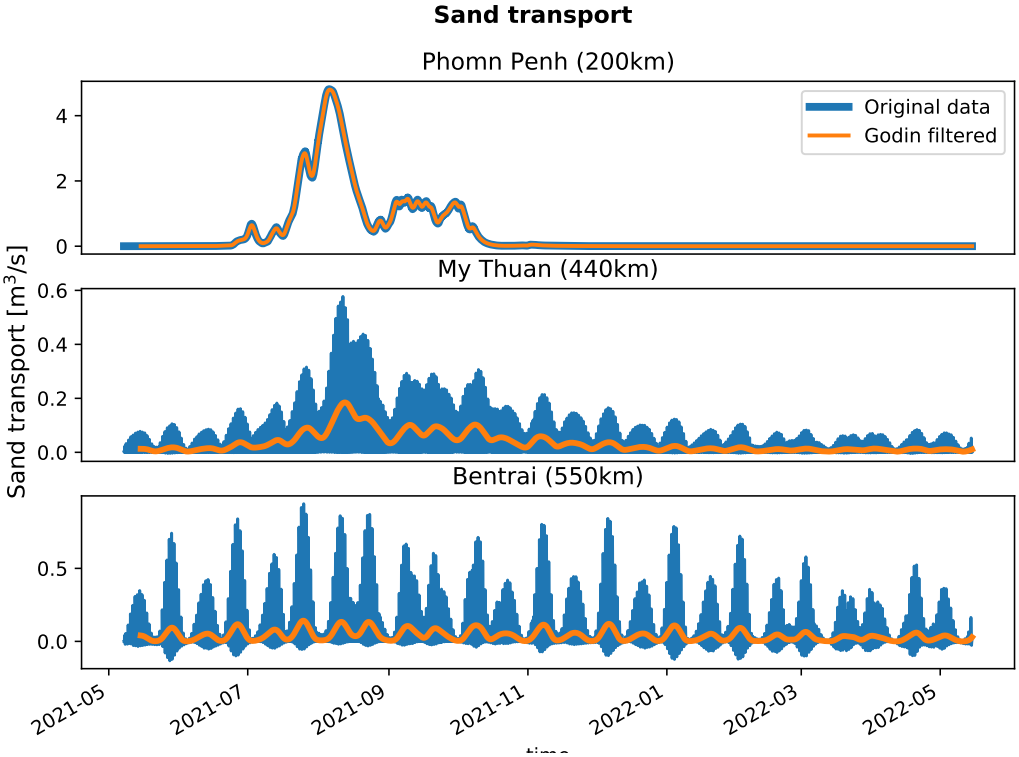

Figure 6.6: (Godin filtered) sand transport rates [m^3/s] for Phnom Penh (Cambodia), My Thuan (middle delta) and Bentrai (mouth).

6.1.2.1. River, river-tidal and tidal influence on sand transport

From these observations, one can conclude that local flow velocities are modulating the sand transport rates and that settling lag effects (present for fines) (see Gatto et al., 2017) are therefore considered small. As flow velocities are altered by both river currents and tidal currents, separating these signals will ultimately explain which process (river currents or tidal currents) are responsible for the transport of sand. To show the role of river flow and tides on sand transport, a heuristic sediment transport formula is used and analysed. For this, cross-sectional averaged flow velocities $U(x,t)$ are decomposed as:

$$U(x,t) = < U(x,t) > + U_{\text{tide}}, \tag{6.1}$$

where $< U(x,t) >$ are the Godin filtered flow velocities, and U_{tide} are the non-filtered tidal currents. Sediment transport is commonly characterised by a nonlinear relationship with the local flow velocity. Depending on the sediment transport formula used, this relationship can follow a power law with exponents ranging from 2 to 5. To gain a better understanding of modelled sand transport, the heuristic predictor assumes $< q_s > \sim < U(x,t)^3 >$, where $<>$ represents Godin filtering. Here, the filtered time series of the flow velocity U is raised to the power of 3 to estimate the sand transport rate q_s. To show that the assumption $< q_s > \sim < U(x,t)^3 >$ is justified for sand transport, Figure 6.8 shows the correlation between $< q_s >$ and $< U(x,t)^3 >$ Phnom Penh, My Thuan and at the mouth of the Bentrai estuary. At Phnom Penh and My Thuan, these strongly correlate. Although some settling lag effects are noticeable at the estuary mouth, they do not significantly impact the correlation.

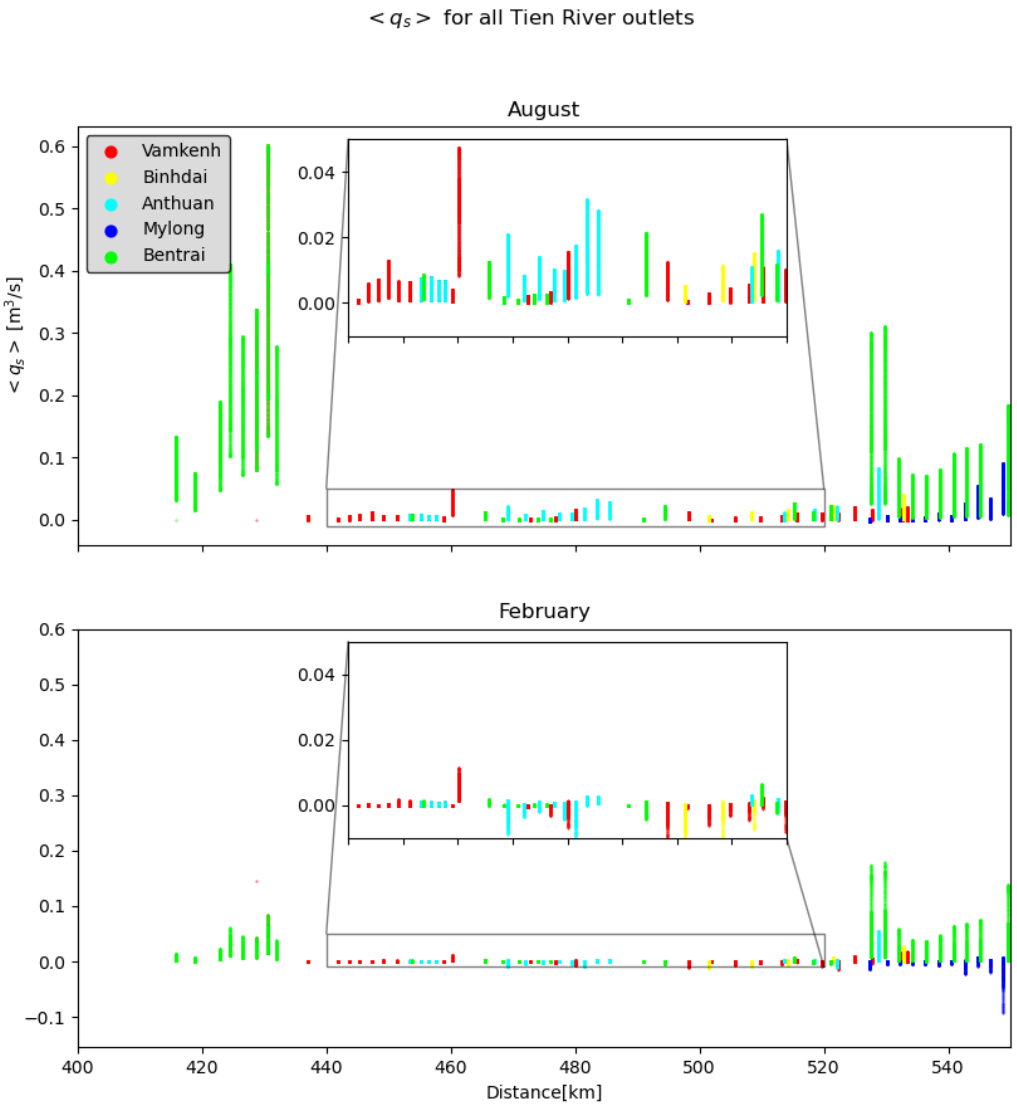

Figure 6.7: All hourly Godin filtered sand transport rates at every cross-section along all the Tien River estuaries after My Thuan for the months of February (upper) and October (lower). Distances are from Kratie, where x=0 is at Kratie. The different colours depict the different estuaries connected to the Tien River.

Therefore Equation 6.1 becomes :

$$< U(x,t)^3 > \sim < (< U(x,t) > + U_{\text{tide}})^3 > \tag{6.2}$$

Solving this:

$$< U(x,t)^3 > \sim << U(x,t) >^3 + 3U_{\text{tide}} < U(x,t) >^2 + 3U_{\text{tide}}^2 < U(x,t) > + U_{\text{tide}}^3 >> \tag{6.3}$$

U_{tide} represents the symmetrical tidal component where differences between peak ebb and peak flood are subtle. As $< U(x,t) >^2$ does not fluctuate on a tidal timescale, multiplying this with U_{tide}

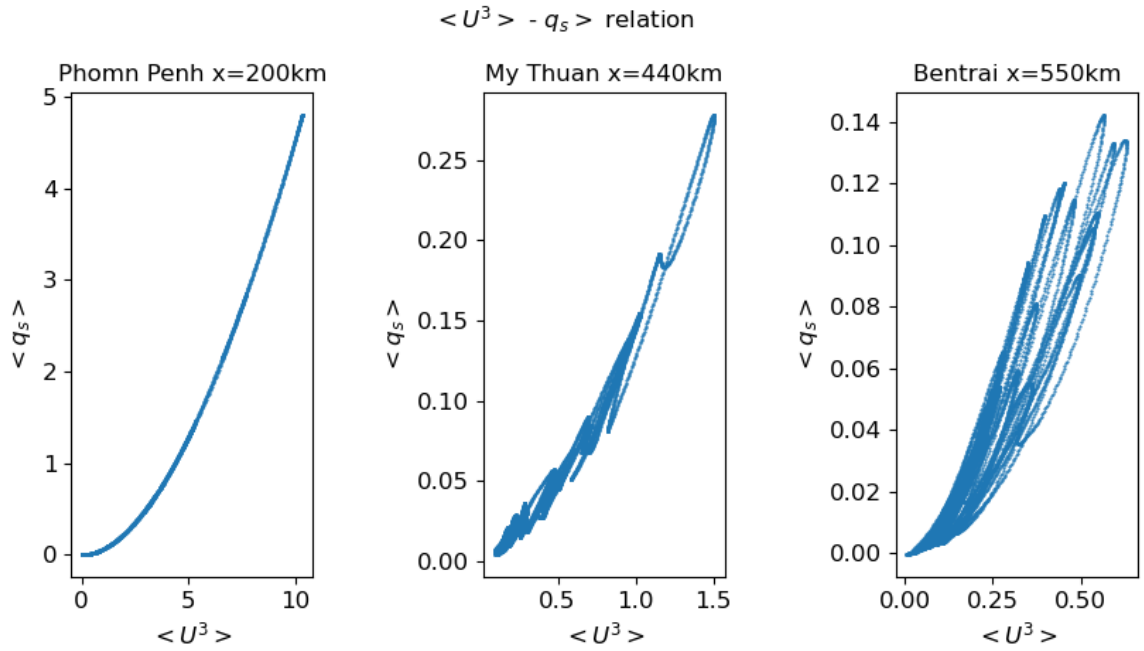

Figure 6.8: Relation between $< q_s >$ and $< U(x,t)^3 >$ at Phnom Penh, My Thuan and at the mouth of the Bentrai estuary.

makes it both symmetrical and fluctuating on a tidal timescale. Therefore, Godin filtering this term will make it zero. Equation 6.3 can therefore also be written as:

$$< U(x,t)^3 > \sim < U(x,t) >^3 + 3 < U_{tide}^2 >< U(x,t) > + < U_{tide}^3 > \quad (6.4)$$

Here $< U(x,t)^3 >$ is a measure for tidally averaged sand transport rates that include both transports by river currents and tidal currents. Further assigned as $U(x,t)^3$. The first term on the right-hand side of equation 6.4, $< U(x,t) >^3$, indicates transport by river only. The second term represents the combined effect of river flows and tides on sediment transport where the transport direction is determined by the river flow. $<U_{tide}^3>$ represents net sand transport due to tidal asymmetry inside the delta. This term can be both positive and negative and the subtle differences between peak flood and peak ebb are exaggerated and will therefore be present after Godin filtering it.

To show the relative importance of each of the components from equation 6.4, each component is plotted separately as U_{river}^3, $U_{river+tide}^3$ and U_{tide}^3 respectively in Figure 6.9. Table 6.1 displays the different parameters used to quantify the transport by the river and tidal currents.

For the first 300km sand is solely transported by river currents 6.9A. This logically follows the results from Figure 6.2E & F as tidal influence can be seen from Phnom Penh onward. As the Mekong bifurcates at Phnom Penh (200km) and Vamn Nao (300km), river sand transport is reduced stepwise at these locations.

From 300km onward, tidal velocity amplitudes start to grow (Figure 6.2) causing U_{tide}^3 and $U_{river+tide}^3$ to increase in magnitude. The region between 350 and 440km distinguishes itself with significant river-induced transport, while at the same time, the highest tidal flow velocity amplitudes are present here. As a result, $U_{river+tide}^3$ is predominantly driving seaward sand transport in this region.

As the river bifurcates at My Thuan (440km) U_{river}^3 fades as its discharge is divided over the two estuaries. Between 440 and 510km, the cross-sectional areas increase (Figure 6.2B) as the channel

Term	Further denoted as	Description
$< U(x,t)^3 >$	$U(x,t)^3$	Dimensionless measure for tidally averaged sand transport
$< U(x,t) >^3$	U^3_{river}	Dimensionless measure for sand transport by river currents
$3* < U^2_{tide} >< U(x,t) >$	$U^3_{river+tide}$	Dimensionless measure for sand transport by river-tide interaction
$< U^3_{tide} >$	U^3_{tide}	Dimensionless measure for sand transport by tidal asymmetry effects

Table 6.1: Definition of the different sand transport parameters that quantify the tidal and river contribution to sand transport.

widens. This reduces both U^3_{river} and $U^3_{river+tide}$ (Figure 6.2)A & B. As a result, low tidally averaged transport rates can be found in this region (Figure 6.7).

Along the transect, seaward sand transport due to tide-river interaction dominates over the opposing flood-dominant U^3_{tide}-term. From this, it can be deduced that the flow reversals from Figure 6.2 do not result in large landward net sand transport fluxes for the Bentrai branch. This confirms the findings from Figure 6.5, where sand transport is seaward for both seasons for the Bentrai (lime) branch.

In the estuaries that show smaller river flows (Anthuan, Vamkenh and Binhdai), landward sand transport fluxes were seen in Figure 6.5. This suggests that, during the dry season, the flood-dominant U^3_{tide}-term is dominant over $U^3_{river+tide}$ and U^3_{river}.

6.1.2.2. Definition of the different zones

From the results of Figures 6.9 & 6.5, three different hydrodynamic and related sand transport regimes can be defined. In Cambodia and the Upper Delta, river sand transport (U^3_{river}) predominantly governs annual sand transport volumes (Figure 6.9) while tide-river interaction ($U^3_{river+tide}$) becomes the dominant driver after 350km. After My Thuan (440km), in the larger estuaries, $U^3_{river+tide}$ dominates over U^3_{tide} for both seasons. In the smaller estuaries, the flood-dominated U^3_{tide} term results in net landward sand transport during the dry season. From these observations, three different hydrodynamic regimes can be defined. A river-dominated section from Kratie up to 300km, a transition zone from 300km up to 440km, whose downstream border for the Tien River is located at the My Thuan bifurcation and a tide-dominated region, present within each estuary downstream of the My Thuan bifurcation. Figure 6.10 defines these regions on a map.

6.2. Sensitivity Analysis

6.2.1. Set-up

This analysis focuses on the separate effects of an altered discharge, SLR, river bed lowering (RB) and subsidence. An overview of the model runs performed can be found in Table 5.2.

Due to the buffering effect on peak flow by dam reservoirs that causes a redistribution of flow between the wet- and dry seasons, cumulative 2040 wet season discharge is estimated to be 18% smaller than the current. Cumulative dry season discharge is estimated to be 12% larger in 2040 than in the present day. To test how this redistribution affects sand transport inside the delta, Section 6.2.2. compares both the wet and dry season of 2040 to the present-day wet and dry season.

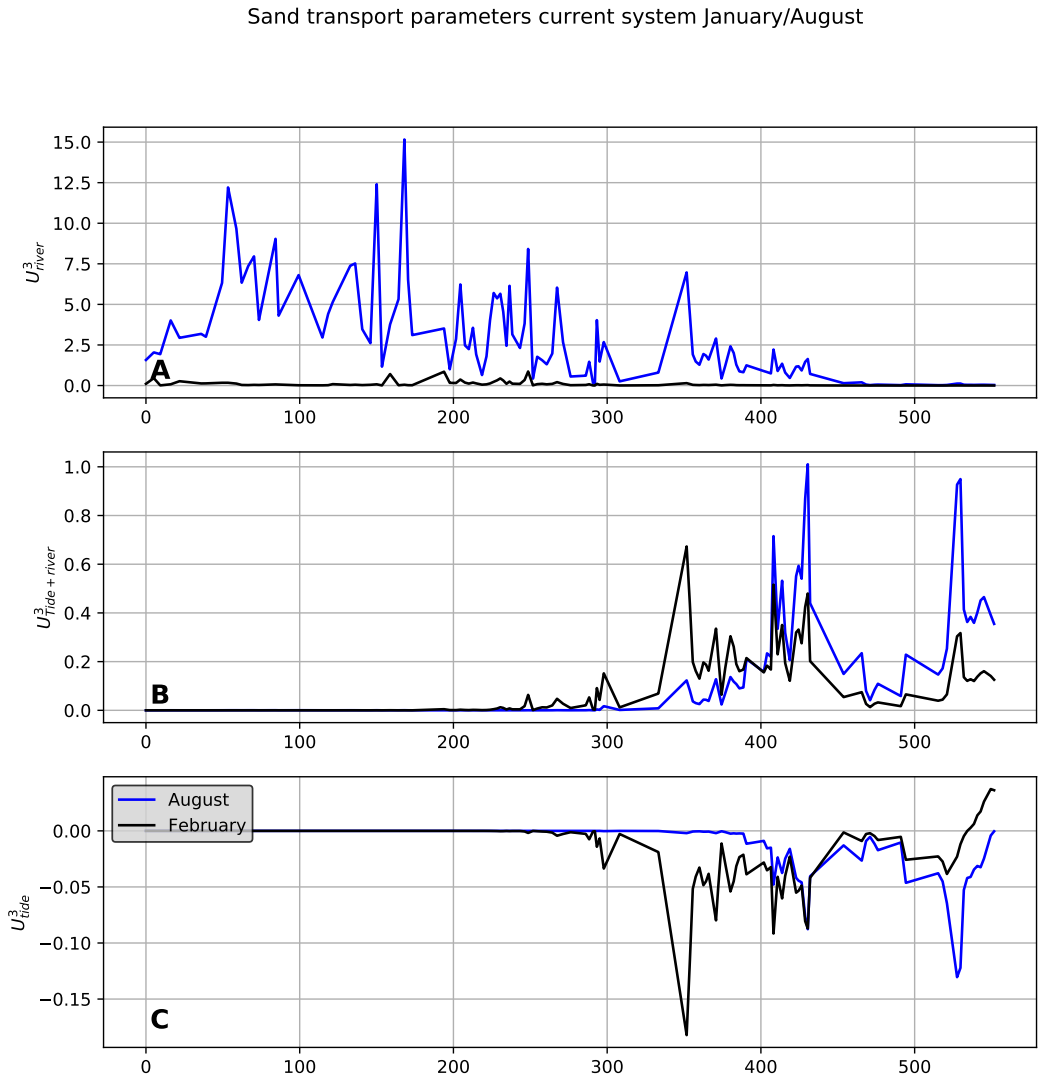

Figure 6.9: Monthly mean A) river sand transport (U^3_{river}), B) tide-river sand transport ($U^3_{river+tide}$), C) tide sand transport (U^3_{tide}). The transect is taken from Kratie (x=0) up to the mouth at Bentrai (x=550) (lime in Figure 4.1). The blue and black line indicate the moving average along the transect for August and February respectively.

To study the separate effects of SLR, RB and subsidence on sand transport, the model is run independently for 50cm of RB, SLR and subsidence. Each of these simulations is done for one year with the 2040 discharge. A comparison is made between the SLR, RB, and subsidence runs and a 2040 discharge run, excluding each of these factors (named: 'No change'). In this comparison, cumulative sand transport, the transport parameters from Table 6.1 and M2 tidal velocity amplitudes are analysed. Due to the high number of branches in the delta and the complexity arising from seasonal variability in discharge this analysis focuses on two transects: The Bentrai branch (from Kratie (x=0) up to the mouth (x=550km) (indicated in lime in figure 4.1) and the Binhdai estuary from My Thuan (x=440km) up to the mouth(x=520km) (indicated in red in Figure 4.1). For the Bentrai branch, only the month of October (peak discharge 2040, Figure 5.3) is analysed, while for the Binhdai branch, both February (dry season) and October were analysed. Choices for these months and locations

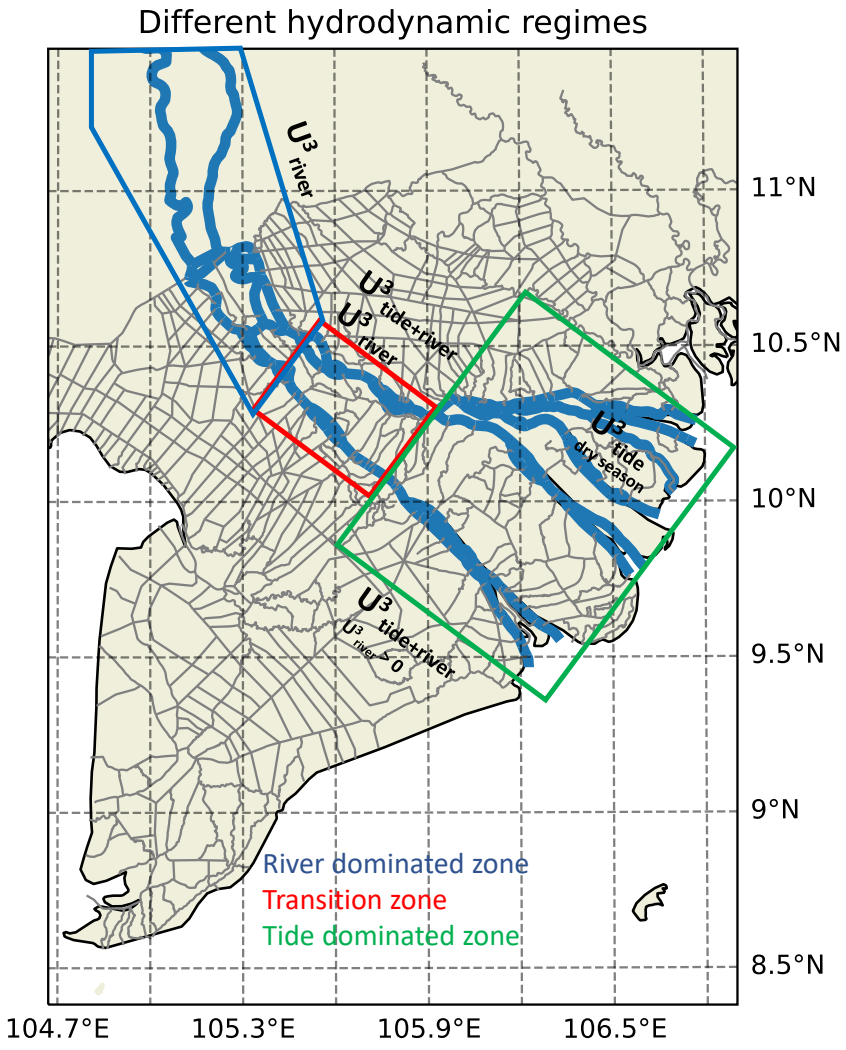

Figure 6.10: The different hydrodynamic regimes that govern sand transport based on the analysis of Figure 6.9

are based on the following argumentation:

- 1) Sand transport during the wet season for the Cambodian section and Upper delta dwarfs the transport during the dry season (Figure 6.5), therefore, the wet season response to RB, SLR and subsidence determines the annual cumulative sand transport response in this region.
- 2) for the Bentrai outlet, although quantities in sand transport between both seasons differ, the trends seem similar (Figure 6.5 & 6.6). It is therefore assumed that the response to RB, SLR and subsidence are similar for both seasons for this estuary.
- 3) The smaller estuaries (Binhdai, Vamkenh and Anthuan) show similar sand transport trends (Figure 6.5), therefore the Binhdai estuary is considered representative for these estuaries. As

sand transport rates in both seasons are low, subtle changes within a season can determine annual transport directions. This makes studying both months for this estuary relevant.

6.2.2. Sensitivity to seasonal discharge variation

6.2.2.1. Sand transport response

The reduced wet season discharge reduces sand transport rates drastically from Kratie (0km) up to My Thuan (440km) (Figure 6.11). The increased sand transport rates during the dry season are negligible compared to the decreased wet season sand transport. Changes are in the range of a 30-40% decrease (Figure 9.7) for the wet season. Appendix figure 9.7 displays the changes for the Bentrai estuary (440-550km). Here, the same trends can be seen, where sand transport decreases mainly during the wet season.

6.2.3. Sensitivity to 50cm of SLR, river bed deepening and subsidence

6.2.3.1. Sand transport response

Bentrai branch October In Figure 9.8 (Appendix), it can be seen that for the Cambodian section/Upper delta (0km to 300km), no large differences in sand transport are visible for SLR and subsidence, while for RB, river sand transport rates increase. Figure 6.12 indicates that, in the river-tide transition zone (between 350-440km, defined in Figure 6.10), the increased M2 tidal flow velocities result in increased seaward sand transport rates for RB, while for subsidence and SLR, the increased tidal flow velocities do not result in higher sand transport rates. For RB, river sand transport (U^3_{river}) remains fairly constant. Therefore, the changed UM2 causes the sand transport rates to increase in the transition zone. For SLR and subsidence, river transport decreases, which causes the sand transport rates to decrease as well. In the tide-dominated zones (between 440-550km), no significant changes in transport can be noted. The small decrease at 520km is a result of decreased tidal flow velocities. As the tidal signal that enters the estuary from the shelf is equal, but water depth (and cross-sectional area) at the mouth is increased, flow velocities decrease at the entrance for all sensitivity runs. For each zone, changes in tidal asymmetry (U^3_{tide}) are negligible for all runs.

Binhdai branch October In Figure 6.13 no significant changes in sand transport rates are seen in October in the Binhdai estuary. Between 460km and 520km, the increased tidal flow velocity is not large enough to cause noticeable changes in sand transport.

Binhdai branch February In February, a slight decrease in sand transport can be seen for the Binhdai branch (Figure 6.14A). Since the sand transport direction is landward in the dry season (Figure 6.5), this means that a larger landward transport is simulated. The decreased sand transport rates from 460km onward correspond to the decreased $U^3_{river+tide}$ (Figure 6.14B). Trends in $U^3_{river+tide}$ cannot be explained by the UM2 character as these are opposite (Figure 6.14C). Also, the lower bed levels and subsidence cause the tide to be more flood-dominated, while for sea level rise, this remains practically unchanged.

From the results above the most important observations are:

- The reduced wet season discharge causes sand transport rates to decrease drastically (5-10Mt) in the river-dominated section. This reduction is not compensated by the dry season increase in sand transport. In the tide-river zone (300-440km), no large changes are seen
- RB results in a slight increase in sand transport in the upstream parts as river transport increases. In the tide-river transition zone (300-440km), overall sand transport rates increase

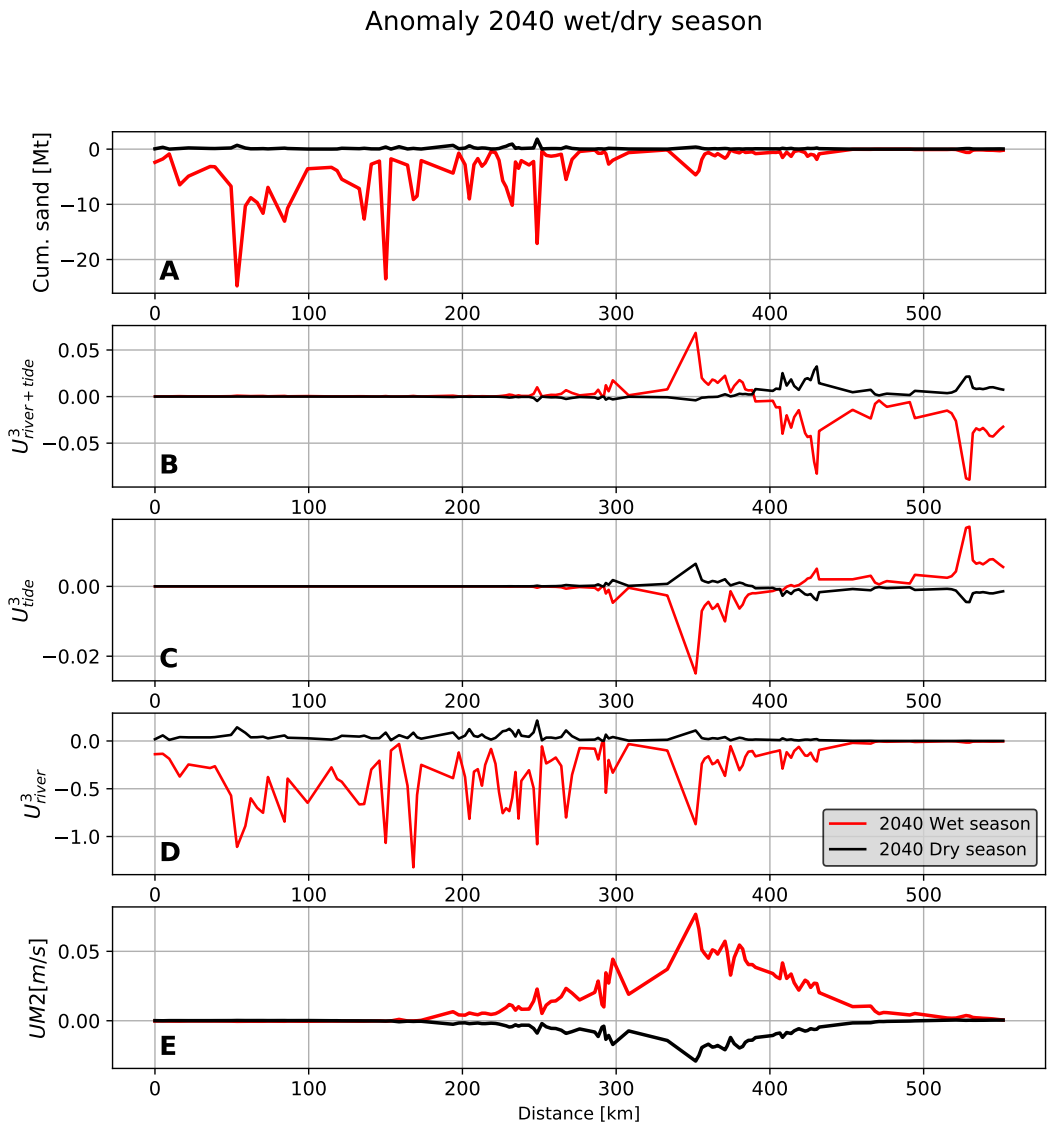

Figure 6.11: Sand transport anomalies for the wet and dry seasons of 2040 compared to the present wet and dry season. The model is run for one year with a 2040 discharge and compared to the present-day discharge simulation for both seasons. The transect is taken from Kratie (0km) to the Bentrai outlet (550km) (lime branch in Figure 4.1).Panels indicate anomalies for A) Cumulative sand transport [Mt], B) Sand transport by tide-river interaction, C) Sand transport due to tidal asymmetry, D) Sand transport by river currents, E) M2 velocity amplitude UM2. The figure shows a large decrease in sand transport in the river-dominated section for the wet season, while an increase int the the dry season does not influence total transport rates significantly).

due to tidal amplification. Tidal amplification in the tide-dominated zone (>440km) is small and does not lead to changes in sand transport.

- SLR and subsidence show a similar response with decreased river flow in the river-dominated and tide-river zone, leading to decreased sand transport rates. Although tidal amplification is more pronounced than for RB in the tide-river zone and tide-dominated zone, it does not lead to changes in sand transport. This is mostly due to the decreased river currents. The only

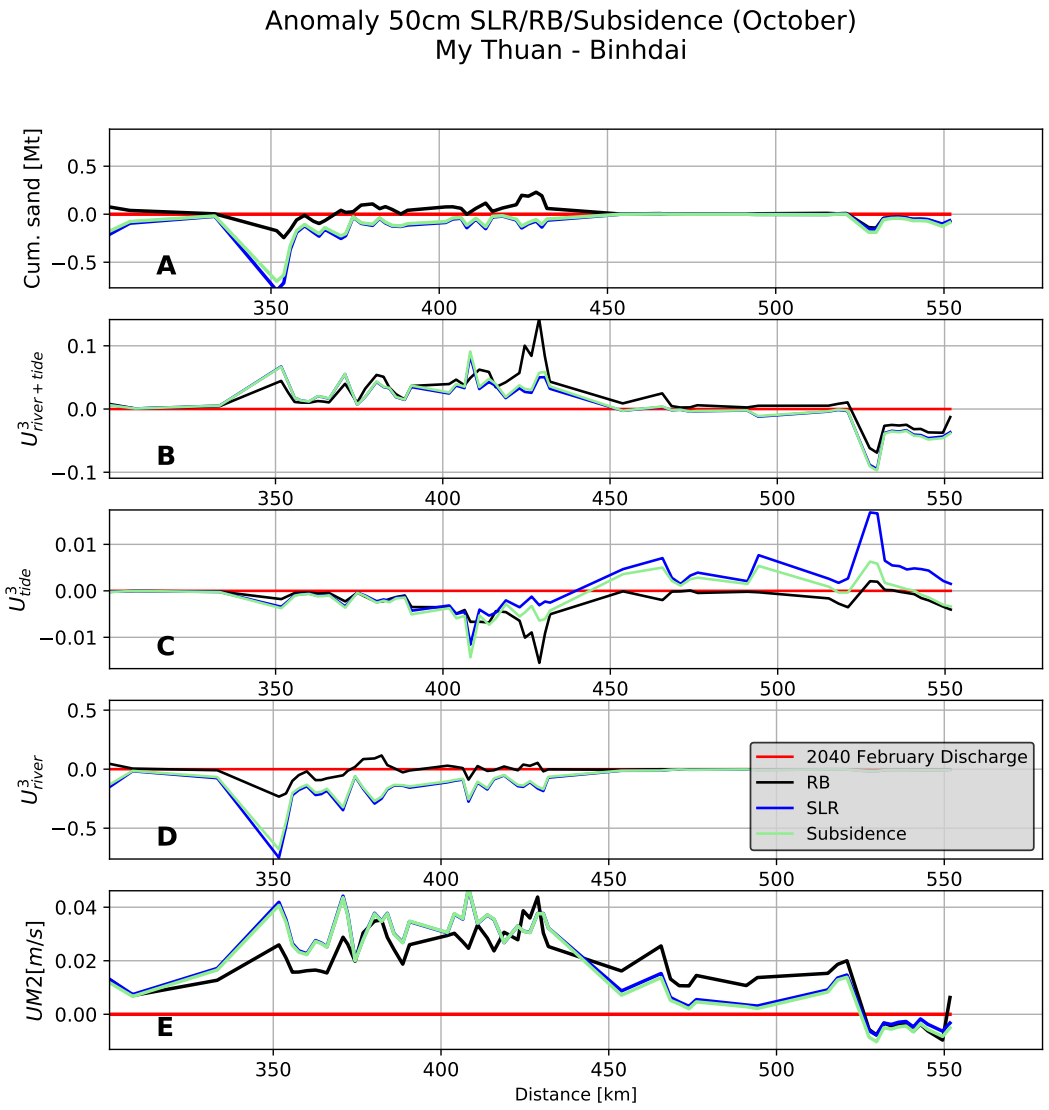

Figure 6.12: Anomalies 50cm of SLR (blue), subsidence (lime) and RB (black). The model is run for one year with a 2040 discharge. Results for the month of October are displayed in this Figure. The transect is taken from the border with Cambodia (300km) via the Tien River up to the Bentrai outlet (x=550). A) Cumulative sand transport [Mt], B) Sand transport by tide-river interaction, C) Sand transport due to tidal asymmetry, D) Sand transport by river currents, E) M2 velocity amplitude UM2. The Figure shows that sand transport for RB correlates with UM2 anomalies, while for SLR and subsidence no increased or decreased sand transport rates can be noted as river currents decreases.

remarkable difference between SLR and subsidence is the increased ebb dominance due to SLR.

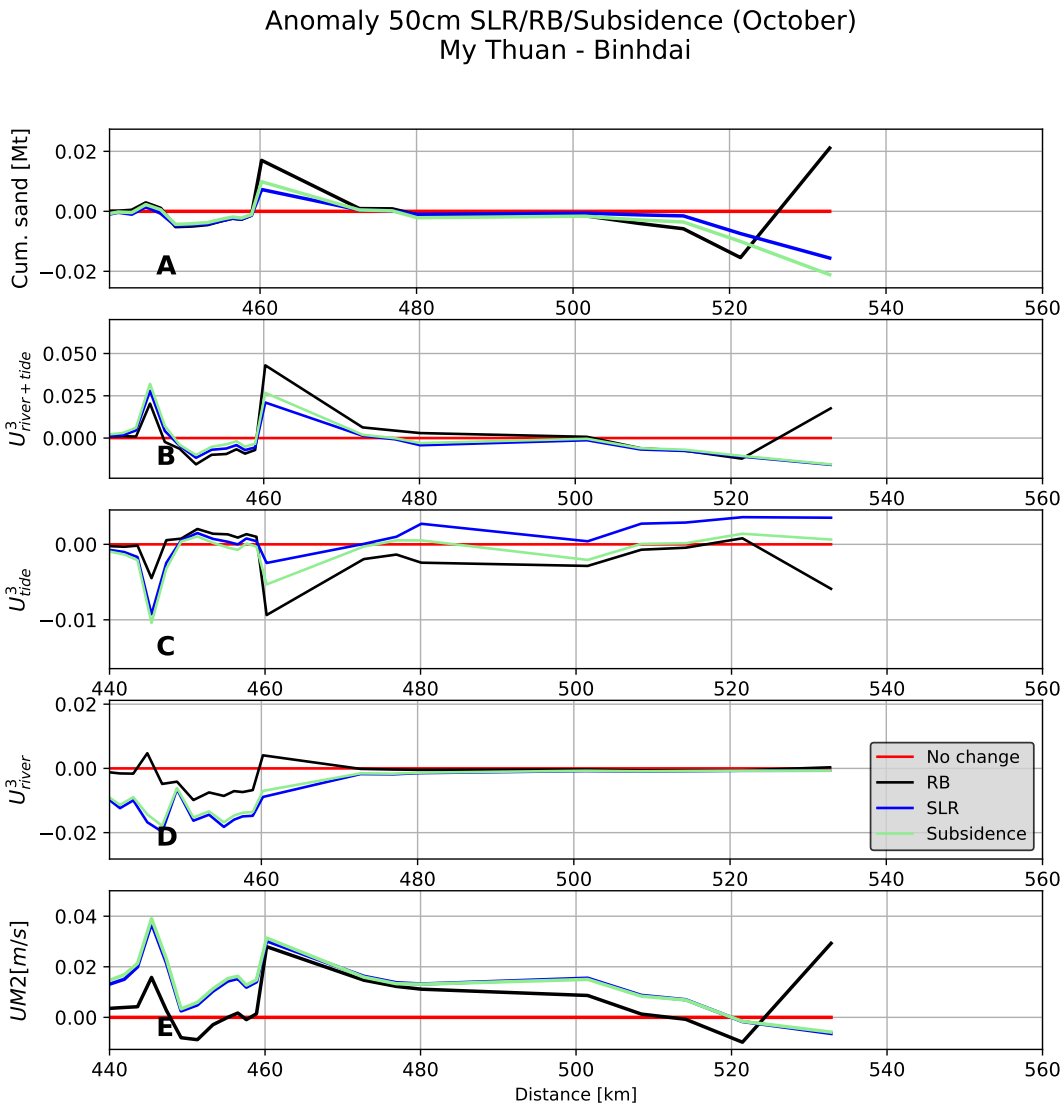

Figure 6.13: Anomalies 50cm of SLR (blue), subsidence (lime) and RB (black). The model is run for one year with a 2040 discharge. Results for the month of October are displayed in this figure. The transect is taken from My Thuan (440km) to the Binhdai outlet (520km). A) Cumulative sand transport [Mt], B) Sand transport by tide-river interaction, C) Sand transport due to tidal asymmetry, D) Sand transport by river currents, E) M2 velocity amplitude UM2. The figure shows no significant changes in sand transport for October in the Binhdai estuary.

6.2.4. Hydrodynamic response sensitivity analysis

The shifts in sand transport are mainly attributable to changes in river flow and river-tide interaction. Tidal asymmetry effects are negligible. While changes in sand transport due to increased and decreased discharge for the dry- and wet seasons are relatively straightforward to understand, the changes in sand transport due to RB, SLR and subsidence are more complex. The next sections will therefore provide insight into the hydrodynamic response that leads to the altered sand transport for RB, SLR and subsidence.

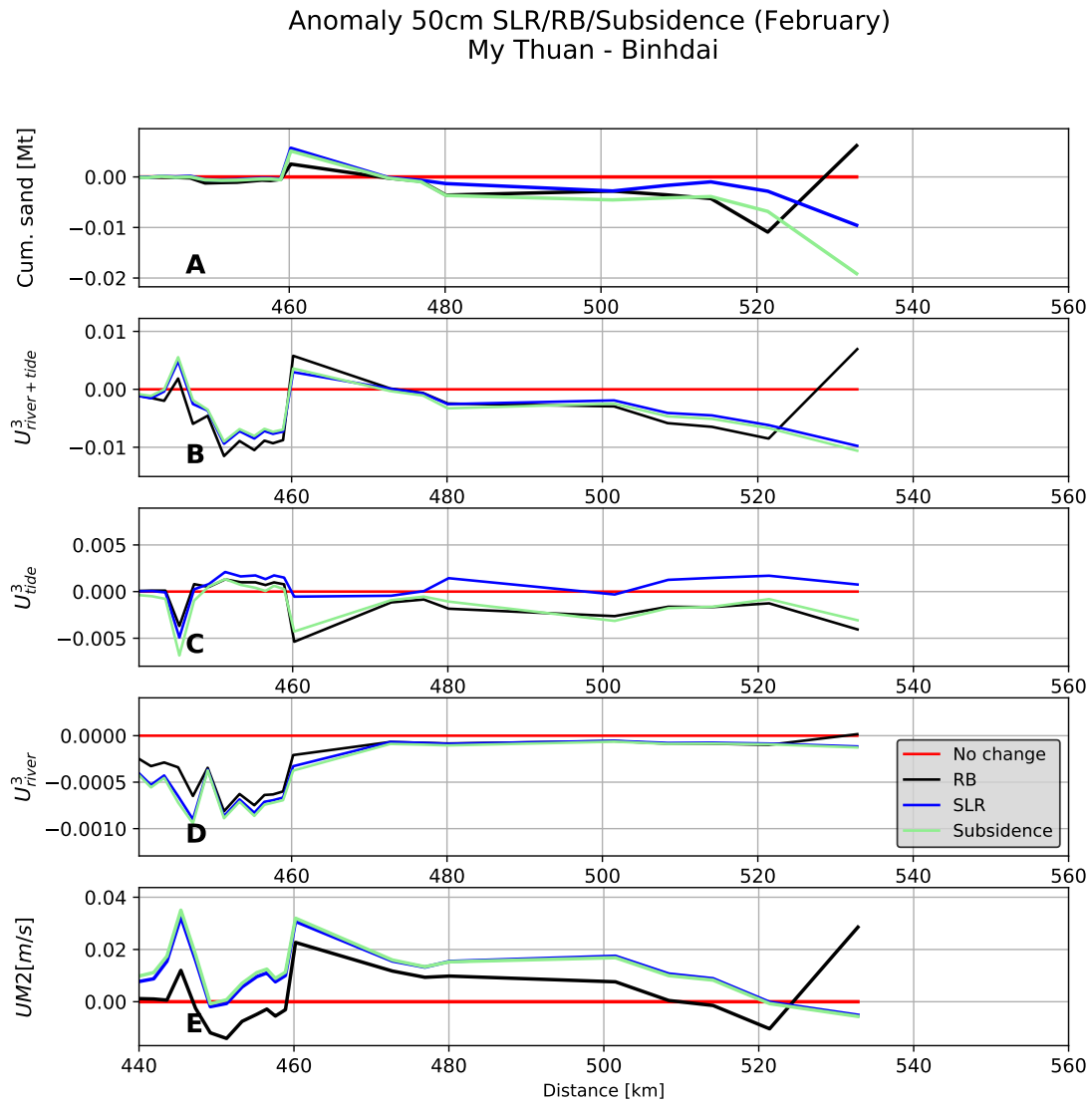

Figure 6.14: Anomalies 50cm of SLR (blue), subsidence (lime) and RB (black). The model is run for one year with a 2040 discharge. Results for the month of February are displayed in this figure. The transect is taken from My Thuan (440km) to the Binhdai outlet (520km) . A) Cumulative sand transport [Mt], B) Sand transport by tide-river interaction, C) Sand transport due to tidal asymmetry, D) Sand transport by river currents, E) M2 velocity amplitude UM2. The figure shows a slight decrease in sand transport for the Binhdai estuary.

6.2.4.1. Floodplains and canals

As U^3_{river} is related to river discharge, the changes in monthly cumulative discharges were studied. To explain the changes in U^3_{river} for RB, SLR and subsidence seen in Figures 6.12 & 6.13, cumulative discharge anomalies for October are displayed in Figures 6.15. To show that similar trends in U^3_{river} can be expected in other branches, the cumulative discharge anomalies for each branch are included.

The reduced cumulative discharge for SLR (blue) and subsidence (lime) from 300km indicate in-

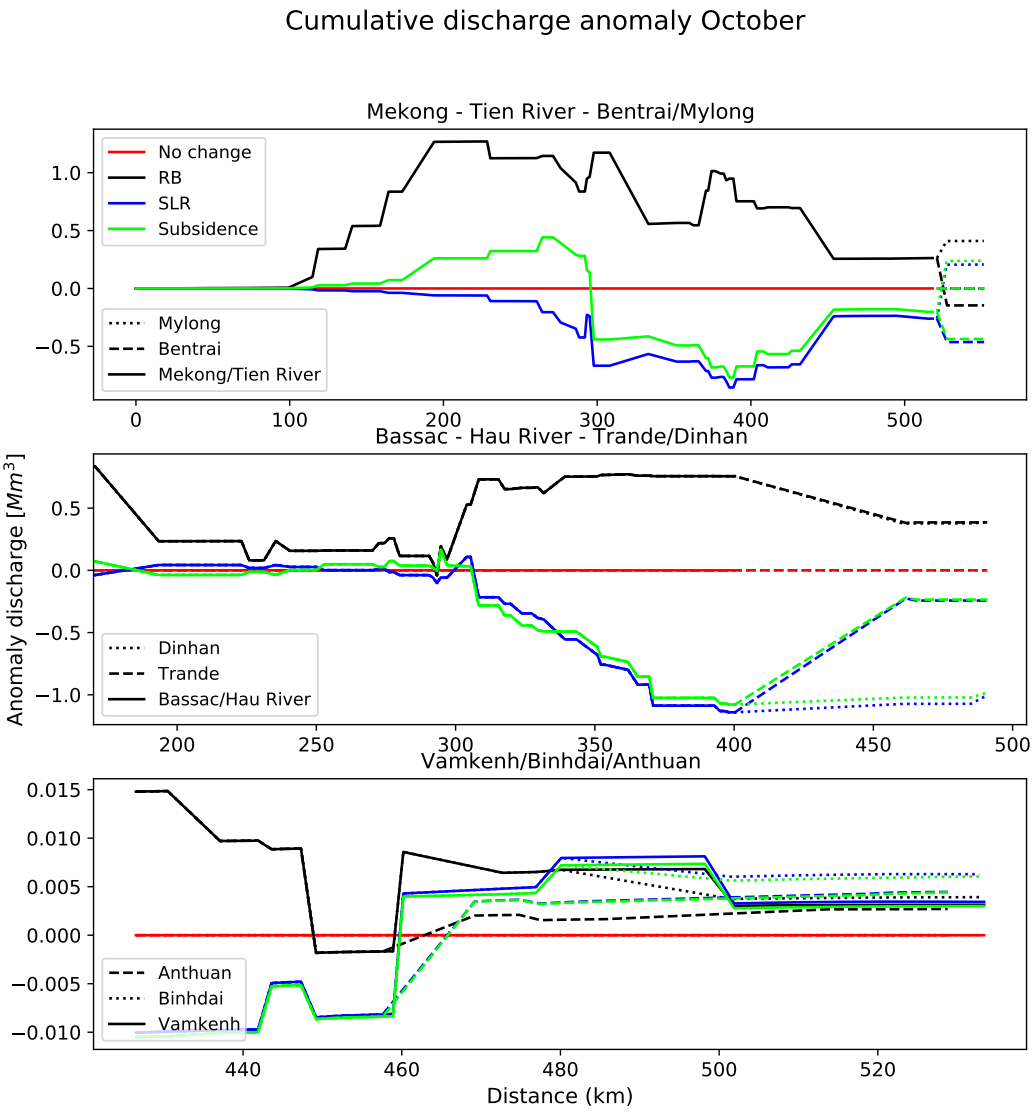

Figure 6.15: Cumulative discharge anomaly October for 50cm of river bed RB (black), SLR (blue) and subsidence (lime) compared to 2040 discharge (red). The upper figure covers the estuaries Vamkenh (solid), Binhdai (dotted) and Anthuan (dashed) from My Thuan (x=420). The middle figure includes the Mylong (dotted) and Bentrai (dashed) outlet from Kratie via the Mekong and Tien River (solid) from Kratie (x=0) up to the mouth. Lower figure shows the Trande (dashed) and Dinhan estuaries up to Kratie from Phnom Penh. The different markers indicate the different branches. All distances are relative to Kratie (x=0). The results show water captured more effectively inside the channels for the RB case, while subsidence and SLR cause increased water spillage towards the adjacent canals and floodplains.

creased water outflow from the channels to the adjacent floodplains and canals explaining the decreasing trends for U^3_{river} for SLR and subsidence seen in Figure 6.12. On the contrary, for RB, increased cumulative discharges are simulated from 100km (Figure 6.15). This can be interpreted as decreased water outflow to the Cambodian floodplains (between 100-200km) and towards TSR (200km).

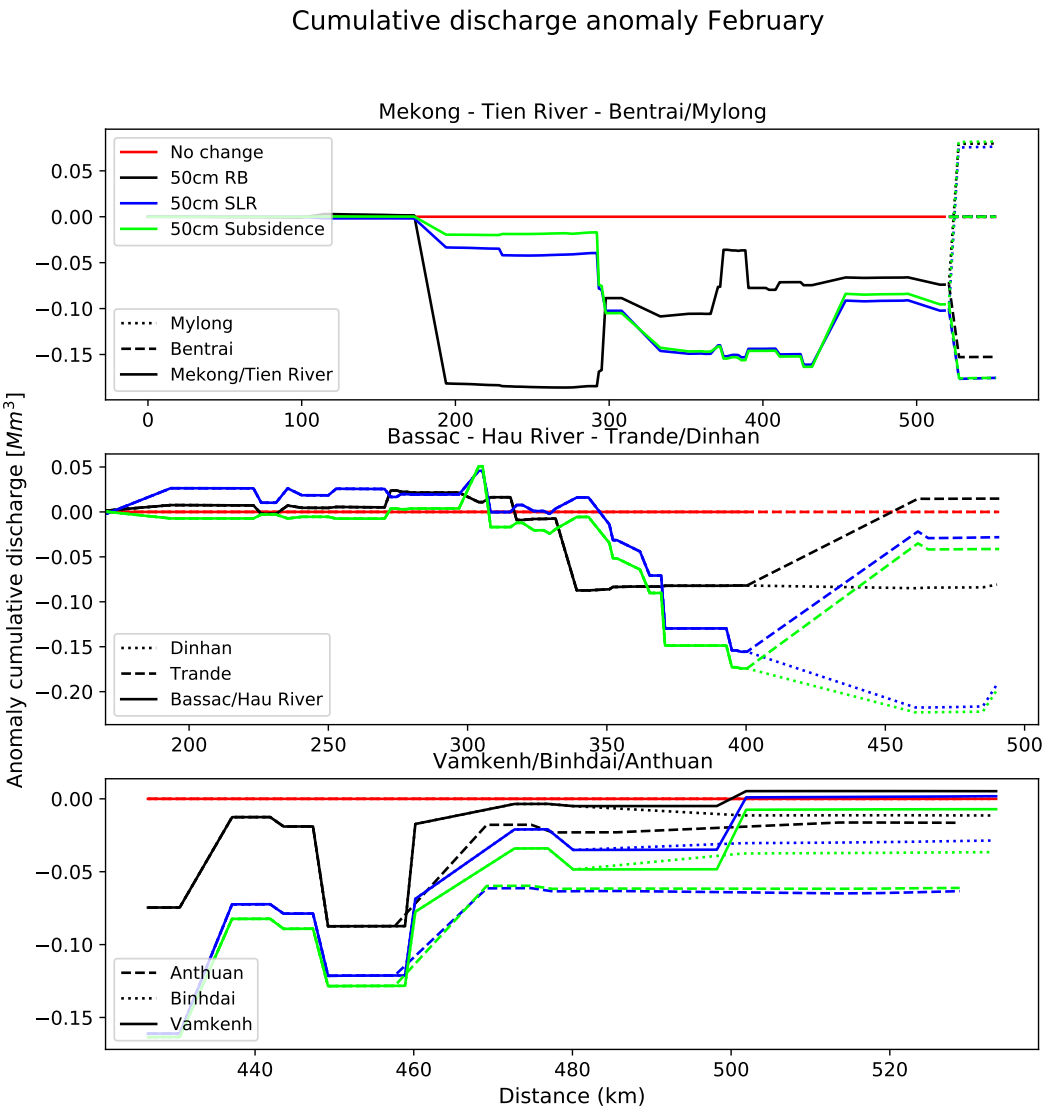

Figure 6.16: Cumulative discharge anomaly February for 50cm of RB (black), SLR (blue) and subsidence (lime) compared to 2040 discharge (red). Upper figure covers the estuaries Vamkenh (solid), Binhdai (dotted) and Anthuan (dashed) from My Thuan (x=420). Middle figure includes the Mylong (dotted) and Bentrai (dashed) outlet from Kratie via the Mekong and Tien river (solid) from Kratie (x=0) up to the mouth. Lower figure shows the Trande (dashed) and Dinhan estuaries up to Kratie from Phnom Penh. The different markers indicte the different branches. All distances are relative to Kratie (x=0). The results show that, mainly for RB, TSL is delivering less water to the Mekong River (at 200km).

Comparing 6.12 with the upper panel of Figure 6.15, shows that increased discharge does not lead to an increased U^3_{river}. Since $U = Q/A$, the increased cross-sectional area from the lower river bed and greater water depths (Figure 6.17) offsets the increased discharge, thereby maintaining relatively constant river flow velocities.

For the Bassac branch (middle Figure 6.15), similar processes can be noted in October. Here an increased discharge for the RB case is present up to the mouth while for SLR and subsidence, neg-

ative annual discharge anomalies from 300km onward are simulated suggesting increased water outflow to the adjacent floodplains and canals of the Bassac branch.

The lower panel shows increased discharges for the smaller estuaries of Vamkenh, Binhdai and Anthuan. Again, the inconsistency between increased discharge and unchanged values for U^3_{river} shown in Figure 6.12 indicates that the increase in cross-sectional area offsets the corresponding increase in discharge.

In February, due to the low discharge and water levels in the dry season (Figure 6.2), no water enters the Cambodian floodplains in this period. Therefore, between 0 and 180km, no changes are seen for RB during this period (Figure 6.16). At Phnom Penh (200km), a decrease is seen for RB in February, suggesting less inflow from TSR. This will be elaborated later.

The discharge anomalies for RB, SLR and subsidence can mainly be attributed to the changes in water levels (Figure 6.17) relative to the river banks throughout the delta. Figure 6.18 schematises this. For sea level rise, water levels for the Middle/Upper and Lower Delta rise, while for subsidence and RB, due to the lower river bed, water levels lower throughout the delta (Figure 6.17 A). For subsidence, both the banks and the river bed are lower. For RB only the river bed lowers, while the banks remain at the same height. As a result, only for RB water levels lower relative to the surrounding banks, while for SLR and subsidence, water levels rise compared to the surrounding banks. As a consequence, during periods with high water levels in the delta, water is more effectively captured inside the channels for RB, while for subsidence and SLR, more water spills over the banks onto the surrounding floodplains.

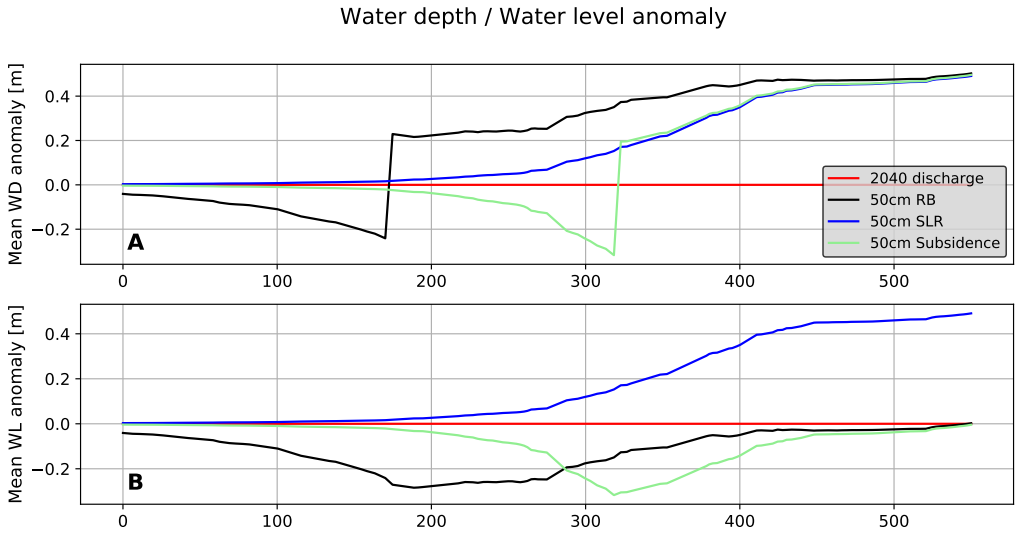

Figure 6.17: Mean water depth and water level anomalies for the Bentrai branch (lime in Figure 4.1) for 50cm of RB, SLR and subsidence. The sudden steps in water depth at 180km and 310km for RB and subsidence mark the location from where the bathymetry is lowered.

6.2.4.2. Buffering effect TSL

The changed water levels inside the delta due to RB, SLR and subsidence cause the buffering effect of TSL on the delta's peak discharge to change. Since the filling and emptying of TSL depends on the water level differences between the lake and the delta, changing the delta's water levels will alter this process. For subsidence and RB, water levels inside the delta are lower compared to the water levels of TSL. As a result, a higher discharge is needed to reach a water level gradient where water

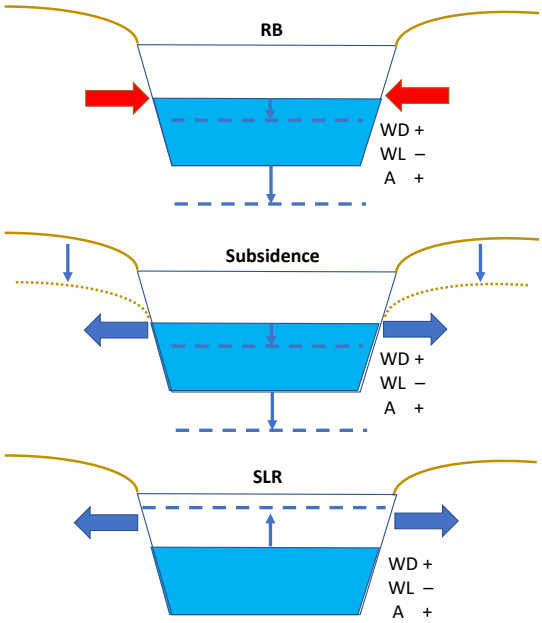

Figure 6.18: Schematic representation of the water level and water depth results from Figure 6.17 where the effects of RB, SLR and subsidence are shown with regard to water level height relative to the banks. While RB, SLR and subsidence result in greater water depths (WD) and greater cross-sectional area (A), the water levels (WL) relative to the surrounding banks differ per case. As the difference between water levels to the surrounding banks is lowered, more outflow of water to the adjacent floodplains and canals is modelled.

flows from the Mekong towards TSL. For SLR the opposite happens. Here, the delta's water levels rise compared to those of TSL. Therefore, a smaller discharge is needed to allow water to flow from the Mekong to TSL. For the RB case, this is more pronounced as the water transport capacity of the Mekong and Bassac channels increases because of the lower river bed, maintaining the steeper water level gradient between TSR and the VMD.

Figure 6.19 displays this mechanism by presenting the discharge anomalies at Prek Kdam, in TSR. For SLR and subsidence, this effect is subtle. For future scenarios, almost no effect can be expected since SLR and subsidence do not exceed 0.5m elevation changes. For RB on the other hand, this effect will become more pronounced as the bed is lowered by 1 and 3m.

Response Tidal velocity amplitude The amplified tidal flow velocities (Figure 6.12E) are a result of increased water depths for each run. As water depth increases and the water column is larger, the friction of the bed on water flow is less effective in reducing the depth-averaged flow velocities. According to Friedrichs, 2010 the friction term (r) can be written as:

$$r = \frac{c_d * 8U}{< h > *3\pi}$$

c_d represents the bottom drag coefficient, h denotes the water depth, where <> indicates a tidal average, U represents the tidal velocity amplitude, r decreases as water depth increases.

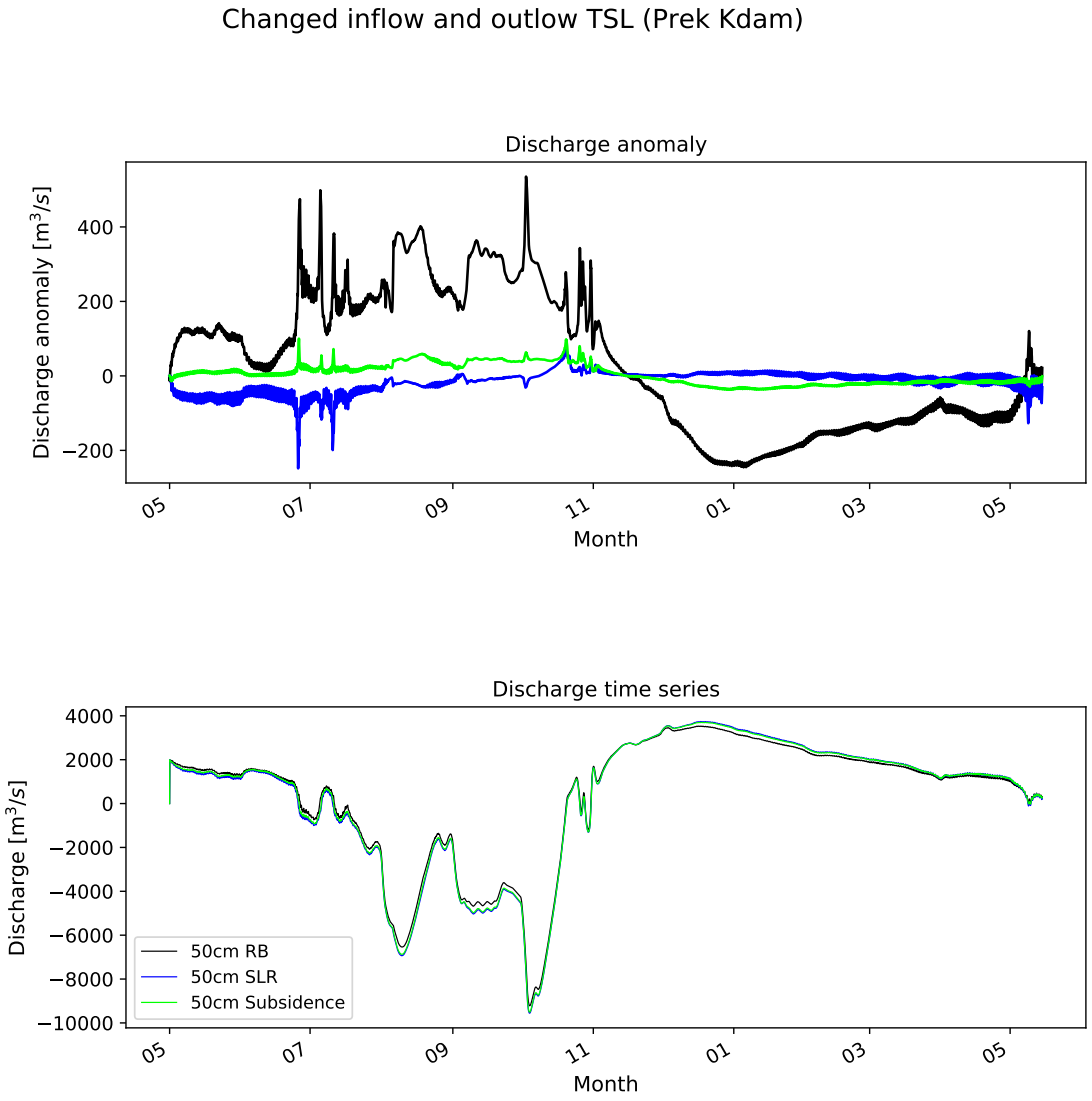

Figure 6.19: One year discharge time series. The upper plot indicates the anomalies for SLR (blue), RB (black) and subsidence (lime). Flow direction is positive towards the sea. The Figure shows that for RB, less water flows towards TSL during the wet season and less water enters the Mekong River during the dry season, decreasing the buffering effect of TSL on the seasonal discharge variations.

This effect strengthens further along the channel, as the tidal wave experiences less friction for a longer distance. Together with the high tidal flow velocity amplitudes already present at My Thuan (Figure 6.9, makes the tidal velocity amplitude at this site sensitive to changes in the water depth in the downstream estuaries.

6.3. 2040 results

For the 2040 runs, all of the tested parameters from the sensitivity analysis are combined for one-year simulations. For this, a moderate and an extreme scenario are tested (see Table 5.2) One of

the goals of this study is to provide insight into the separate effects of each of these perturbations. Therefore, for the sensitivity analysis, each of these perturbations is compared for the same rate of change. For the 2040 analysis, the projected changes for each are included based on the current literature. Here, RB will become relatively more important as incision rates outnumber SLR and subsidence by an order of magnitude for 2040 (Table 5.2). In this section, the 2040 results are compared to the present-day results from Section 6.1.. For this, the model is run for one year for both scenarios.

6.3.1. 2040 annual sand transport

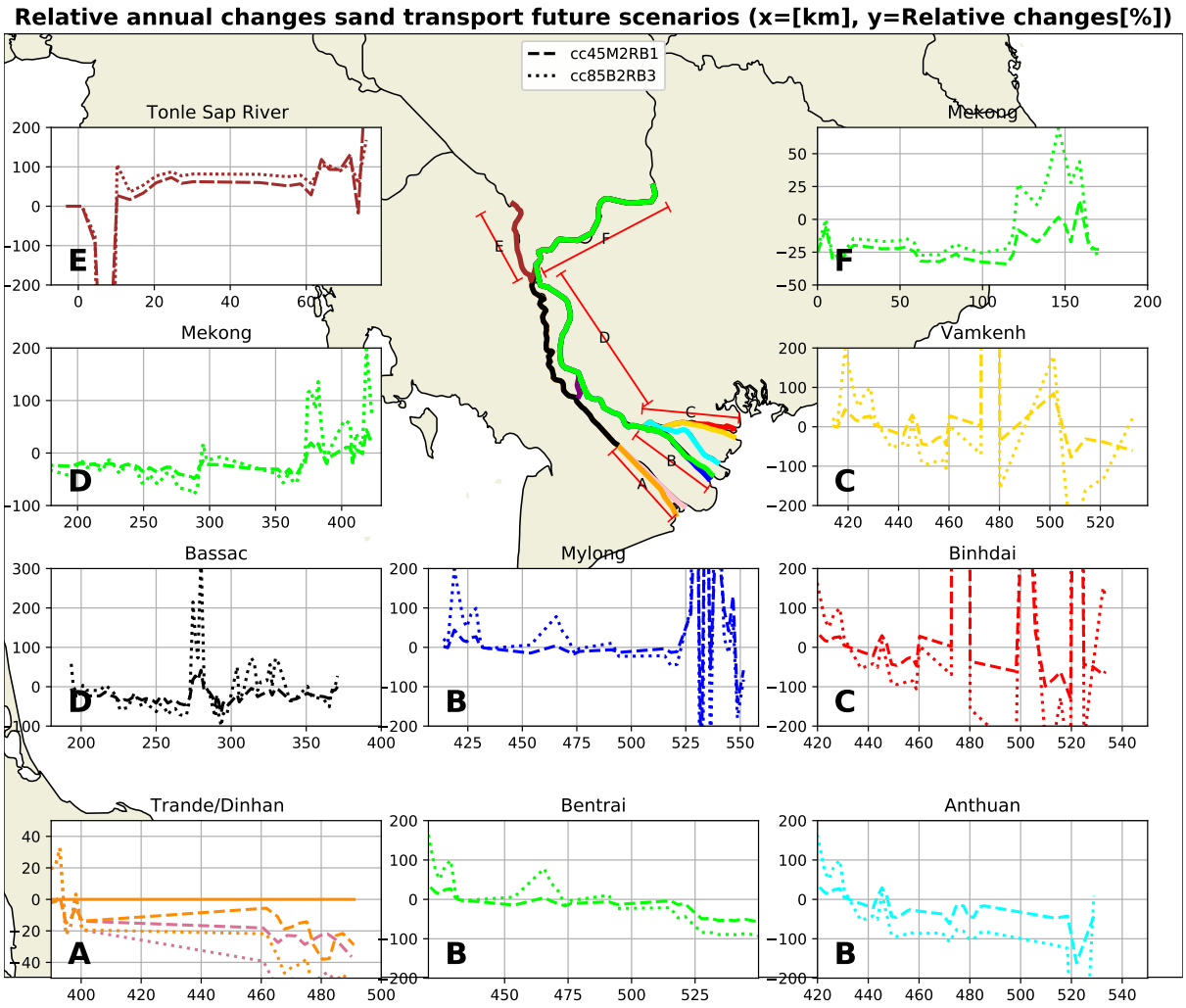

Figure 6.20: Relative annual sand transport changes $((scenario - presentday)/presentday * 100\%)$ for both future scenarios compared to the current situation. Each graph corresponds to one of the transects displayed on the map. For all transects except Tonle Sap River, distances are from Kratie. For Tonle Sap River x=0 at Tonle Sap Lake.

.

River dominated zone At Kratie, an approximate 20% decrease in sand input is simulated for both scenarios (0km transect F, Figure 6.20) (absolute changes can be found in Appendix Figure 9.9). From Phnom Penh onward (200km, transect D), a constant reduction of 20-30% can be seen. This percentage is in line with the wet season reduction in sand transport seen in Appendix Figure 9.7.

The large increase in transport between 120-170km can be considered a model artefact as RB is defined only from 150km, causing flow velocities to increase in this area. Between both scenarios, no significant differences can be seen up to My Thuan (440km) and the decreased sand transport change remains relatively constant. This suggests that the effects of RB, SLR and subsidence on cumulative annual sand transport are insignificant compared to the reduced wet season discharge in this section.

Tide-river transition zone In the tide-river transition zone in the Mekong/Tien River (transect D, 350-440km), sand transport rates increase for both scenarios. This is a result of the amplified tidal signal also seen in Figure 6.12, where the amplified tide results in larger seaward transport. Interestingly, the decreased wet season discharge does not offset this effect. Here, significant differences between both scenarios exist, where for the extreme scenario (CC85B2RB3), transport rates double in some areas.

Tide dominated zone Although the changes in sand transport differ locally, overall transport volumes decrease at every outlet (Transect A,B,C between 440 and 550km) for both scenarios. An exception is the Mylong outlet between 525 and 550km), this can be attributed to the redirected discharge from the Bentrai branch (Appendix Figure 9.11). Comparing both scenarios, for the extreme scenario, transport rates decrease relatively more than for the mild scenario. This is mainly caused by the lower river beds for the extreme scenario. As the river bed lowers, the cross-sectional area of the river increases. This causes flow velocities to decrease in the estuaries. Although the greater water depths allow the tidal signal to amplify at My Thuan, in the estuaries, the increased cross-sectional area counterbalances this. As a result, tidal flow velocities decrease (Appendix Figure 9.10) .

6.3.1.1. Timing of sand transport

Although RB, SLR and subsidence have little influence on the annual sand transport rates seen in Figure 6.20 in the river dominated section, it does influence the the annual distribution of sand transport through time. Figure 6.21 shows the number of days it takes when 50% the annual load is transported. For this, hourly, Godin filtered sand transport rates ($< q_s >$ were ranked from high to low and summed to find the number of hours until it met the following condition:

$$\sum_{k=0}^{n} < qs_k^{sorted} > \geq \frac{Total\ annual\ transport}{0.5} \tag{6.5}$$

Figure 6.21 displays the results for the Mekong river section. The number of days where equation 6.5 is satisfied is plotted on the vertical axis. From the results it can be deduced the time it takes for 50% of the sand to be transported is reduced by approximately 20 days in the river-dominated section for the CC85RB3B2 scenario, which is halved for this section. This is in line with the findings of the sensitivity analysis. As the river bed is lowered, the wet season peak discharge is more effectively captured inside the river channel as the buffering capacity of the floodplains and TSL decreases. During the dry season, less water from the floodplains and TSL will be delivered to the river. As a result, relatively more sand is transported during the wet season compared to the dry season. This leads to a more pulse like character of the sand transport. From 300km, the opposite is seen. Here transport duration is extended. This is caused by the increased influence of tides on the sand transport for both scenarios.

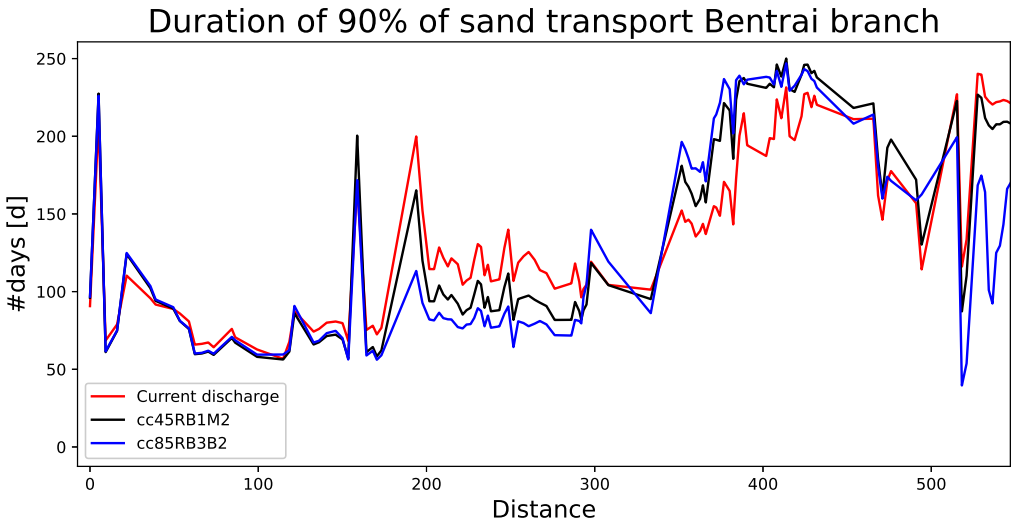

Figure 6.21: Number of days where 50% of the sand is transported for all future scenarios along the Mekong River from Kratie (0km) up to the Bentrai outlet at the mouth (550km)

.

Chapter 7

Discussion

7.1. Synthesis main findings

This study characterises the relative influence of river, tide-river and tidal transport and classified three different hydrodynamic regimes for the present-day system. Based on the results, a description of the current system, its response to human influences and a projection in sand transport for 2040 are summarised for each hydrodynamic regime.

7.1.1. River dominated zone (<300km)

In this section, sand transport rates are high and vary locally. These fluctuations are driven by the varying cross-sectional areas of the river (Figure 6.5 & 6.9). Moreover, in this region, sand transport is highly seasonal (Figure 6.6) and sensitive to future changes of the wet season discharge (figure 6.11). Here sand is almost exclusively transported during the wet season (Appendix Figure 9.5.

The alternation of the tidal signal due to river bed lowering, SLR and subsidence only have minor effects on annual sand transport volumes in this region. While river bed lowering has minimal impact on the annual sand transport in the river dominated zone, its effect on the timing of the sand transport is noticeable. With the deepened channels, water level lower relative to the river banks, reducing the outflow to the adjacent floodplains, canals and TSL during the wet season. This reduced connectivity to the floodplains, canals and TSL, results in a decrease in the deltas buffering capacity of peak discharges occurring in the wet season. Consequently, a more pulse like character of sand transport in the upstream sections of the delta was simulated (figure 6.21).

As sand is exclusively transported during the wet season, for 2040, the reduced wet season discharge will significantly reduce annual sand transport in this region.

7.1.2. Transition zone (300-440km)

The tide-river transition zone regions experience the greatest tidal velocity amplitudes as the channels have a low width-to-depth ratio and strongly converge (Gugliotta et al., 2017). In this region, tide-river transport dominates the sand transport mechanisms.

Sea level rise, subsidence and river bed lowering cause greater water depths inside the channels (Figure 6.17), resulting in an amplification of the tide (Figure 9.8E. This effect strengthens further along the channel, as the tidal wave experiences the decreased dampening effect for a longer distance. Together with the high tidal flow velocity amplitudes already present in this zone, makes sand transport sensitive to variations in tidal velocity amplitudes. Regarding annual sand transport, the tide-river transition zone mainly respond to the amplified tide in the seaward estuaries. Changes in wet season discharge are less relevant.

For 2040, this regions experiences increased sand transport rates due to an amplified tide.

7.1.3. Tide dominated zone (>440km)

After the My Thuan bifurcation, as the channels widen and sand transport by river currents are reduced and transport rates drop rapidly (Figure 6.7). Most of the sand is conveyed through the Bentrai, Trande and Dinhan outlets. In these estuaries, sand transport due to tide-river interaction

dominates over tidal asymmetry effects for both seasons (Figure 6.9). This results in a net seaward annual sand transport. In the smaller estuaries, during the dry season, net sand transport is directed landward (Figure6.5) due to flood-dominated tidal currents. In the wet season river currents cause net transport to be seaward. This opposing sand transport directions per season, ultimately results in a small seaward net annual sand transport (Figure 6.5).

After the My Thuan bifurcation, where the Mekong river transitions into the estuaries, channels widen. In these regions, width-to-depth ratios are high. The estuaries water depth increases because of river bed lowering, sea level rise (SLR), and subsidence. Additionally, it has higher width-to-depth ratios. As a result, the cross-sectional area of the estuaries increase more than in the upstream section, where the width-to-depth ratios are lower. Although the reduced friction allows the tidal wave to amplify further landward, in these regions, the large increase in cross-sectional area offsets this amplification.

Therefore, for the 2040 scenarios, the 1m and 3m river bed lowering result in a larger increase in cross-sectional area by which tidal flow velocities are reduced. As a result seaward sand transport rates in the estuaries decrease.

7.2. Simplifications and modelling assumptions

7.2.1. Sand flux estimations

An important simplification made in this study is the 10m thick bed containing a single-sized sand fraction of 200μm defined in each channel. Sub-bottom profiling surveys from Deltares show that the sand bed thickness, especially in the estuaries, is significantly thinner and at some locations, bed rock is exposed on the river bed or other sediment types are present (Gugliotta et al., 2017). Especially in the estuaries, the bed is mainly composed of finer material. This study showed that sand is mainly extracted from locally available sand reservoirs. Therefore, at locations where no sand is present on the bed, little to no sand is expected in the water column. The increased sand transport rates at the mouth displayed in Figure 6.5 show that these can only exist due to local sand availability present in these regions. Therefore, the sand export estimations made by Tu et al., 2019 should be carefully interpreted as this study also defines sand to be available uniformly throughout the bed.

Although the models hydrodynamics have been shown to perform well (Quoc Thanh et al., 2020), the model was not calibrated on sand transport measurements. Also, validation of the sand transport estimations are difficult due to the limited availability of data on sand in the delta.

7.2.2. Local sand transport variation

The model simulated highly varying sand fluxes throughout the delta that were closely correlated to flow velocity variation due to changes in cross-sectional area along the transect (Figure 7.1). As settling velocities are high, sand settles quickly at locations of lower flow velocities at locations with a large cross-sectional area. Where cross-sectional areas are small, local flow accelerates and sand transport rates increase. As cross-sectional areas vary highly throughout the study area, cumulative sand transport rates vary on the order of magnitudes within a couple of kilometres.

In Cambodia, these effects are most pronounced. In this region, bathymetry data is most limited. Also, here most of the bathymetry data points are linearly interpolated according to V. Q. Thanh et al., 2020. The inaccuracies or omissions in predicting the geometry of the thalweg contribute to the underestimations in cross-sectional area at 50 and 150km. At the same time, river flow velocities are high due the large discharge volumes conveyed through the channel. Therefore sand transport

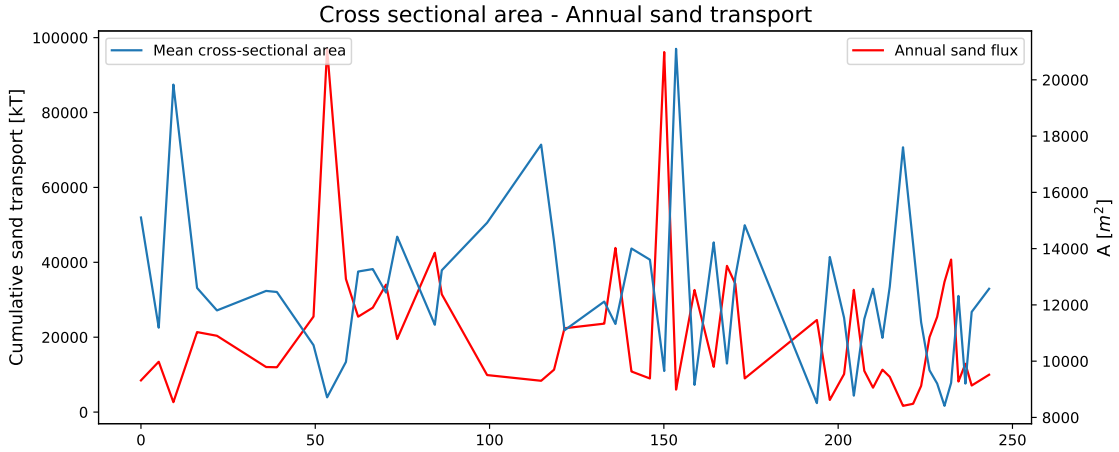

Figure 7.1: Mean annual cross-sectional area and annual sand transport from Kratie x=0 up to downstream of Phomn Penh (x=250km). The cross-sectional area is highly related to the cumulative annual transport. Where cross-sectional area is low, local flow velocities increase and cumulative sand transport increases.

rates are extremely sensitive to the bathymetry inaccuracies in this region. With an incoming sand flux of 6.18 $\pm$ 2.01Mt/yr Hackney et al., 2020, local cumulative sand transport fluxes of around 100Mt, estimated at 50 and 150km (Figure 6.5) would drive unrealistically high erosion rates locally.

Although high variability in sand transport rates along the river channel are not uncommon in rivers Nittrouer et al., 2012, this model is extra sensitive to the bathymetry variation as deposition and erosion do not lead to changes in bed level. In locations where erosion is high, incorporating incision would enlarge the cross sectional area. This reduces local flow velocities and sand transport rates which reduces the error at locations with inaccurate bathymetry.

7.2.3. Sand-mud coupling

In the estuaries, Gugliotta et al., 2017 reports an abundance of mud fractions present. Allison et al., 2017 mentions soft layers of mud observed on the channel floor in the estuarine zone during periods of low discharge. These layers cover the sand, shielding it from shear stresses during high discharge. This mechanism is likely to limit the suspended sediment concentration in periods of high flow, reducing the export capacity of these outlets. During the low discharge season, suspended and bedload transport are likely to completely shut down due to this (Allison et al., 2017). This, together with the findings of this study, argue that, on an annual basis, net export via the Vamkenh, Anthuan, Binhdai and Mylong outlets are small. To further improve the models capability in estimating sand fluxes in these regions, further research on incorporating sand-mud coupling in the model is recommended.

7.2.4. 3D-estuarine circulation

In the Dinhan outlet, seaward sand transport for both seasons have been simulated while Nowacki et al., 2015 measured a landward sediment (fines and sand) flux during periods of low flow in the Dinhan outlet. In this study, during a 25h measuring campaign, the relative contribution of tidal currents and transport due to salinity-driven estuarine circulation flows was depicted. Both these processes were relevant in the transport of the total sediment load during periods of low flow. As the model used in this study is in the 2D domain, these 3D circulations are not included, which could

potentially underestimate landward transport during low flow. Therefore, during the dry season, incorporating salinity driven 3D-estuarine circulation would potentially improve sand transport estimations. Still, for sand, estuarine circulation currents might not be as an important contributor to total transport as these currents are weak, and the settling velocity of sand, compared to fines, is high.

7.2.5. Suggested model improvements

To sum up, model improvements can be made on the following points

- Incorporation of different sediment grain sizes or bedrock on the bed surface
- Further validation and calibration to sand transport measurements.
- An improved cell resolution of the river bed that allows the inclusion of high-resolution bathymetry measurements
- Include a 3D domain in the estuaries, capable of simulating gravitational-driven estuarine circulation flows.

Due to these limitations, the values for the fluxes should be carefully interpreted. The transport estimates provided in this study can therefore be considered as (maximum) sand transport potentials and should not be considered as absolute fluxes. The goal of this study has not been to quantify absolute sand fluxes but rather to provide insight into complex processes throughout the delta that govern sand transport and how these are projected to change in the future.

7.3. Comparison to current literature

Despite the assumptions and simplifications made in this study that mainly lead to the over estimations of the annual sand flux (Hackney et al., 2020), it was able to capture the hydrodynamic processes and sand transport mechanisms that have also been found in other literature.

7.3.1. Hydrodynamic regimes

To understand the large scale sand transport mechanisms, this study distinguishes three different hydrodynamic regimes within the study area based on a flow velocity analysis. A river-dominated regime, tide-river transition zone and a tide-dominated regime. These regimes and their transitions, have also been distinguished byGugliotta et al., 2017 based on sedimentological properties found in the bed. Despite methodological differences between Gugliotta et al., 2017 and this study, the comparable positions of the regimes suggest that that the flow velocity analysis used in this study (Figure 6.9) parameterise the different hydrodynamic regimes well.

7.3.2. Sand versus fines

This study showed that the sand load inside the Mekong Delta behaves fundamentally differently than the fine particle load modelled by V. Q. Thanh et al., 2017. As fines remain in the water column as settling velocities are slow, a large part of the simulated sediment flux originates from further upstream. For sand this is different. Stephens et al., 2017 observed a that suspended sand in the water column mainly originates from the local bed source for the Bassac outlets. The significant variation in local sand transport (Figure 6.2) and the disparity between low transport rates in the estuaries and high sand transport at the mouth (as depicted in Figure 6.5) confirms that the results do not indicate an incoming sand flux from upstream. Instead, the presence of suspended sand in the water column is primarily influenced by the local presence of sand in the bed.

7.3.3. Sand mining pits

Although high variability in annual sand transport can partly be attributed due to inaccuracies in bathymetry reconstructions, (Jordan et al., 2019) describes the trapping of local aggregates by sand mining pits and the presence of scour holes. This study also showed that annual sand transport is highly sensitive to changes in channel geometry variations, confirming that these local deepenings likely trap locally available sand reducing the suspended sand concentration locally.

7.3.4. Decreased buffering effect

The hydrodynamic response to incision in the delta has been studied previously. Eslami et al., 2019 measured increased M2 tidal amplitudes and attributed this to lower bed levels. This study showed that subsidence and SLR also contribute to this (Section 6.2.3.). Binh et al., 2021 noted statically lower water level during the dry season despite increased discharge for this period.Park et al., 2020 measured decreased inundation-frequencies in the Long Xuyen Quadrangle area suggesting reduced connectivity of the river channels to the floodplains. Also the reduced inflow towards TSL found in this study (Figure 6.19) strengthen the claim made by Chua et al., 2022 stating that incision is an important driver in the reduced inflow from the Mekong River to TSL.

7.4. Future implications of the results

This study is the first that was able to replicate delta-wide hydrodynamic processes and link it to the sand transport mechanisms inside the delta. Furthermore, this study provides an overview of the system response to the human-induced hydrodynamic and morphological changes inside the delta.

A decreased wet season discharge reduces the transport capacity of the Mekong River by 1-10Mt/y. Figure 9.9. As a result, less inflow of new sand towards the delta is expected on a longer time scale. Unlike the 'sand hunger' caused by sand trapping of dams, annual sand transport responds instantaneously to changes in the wet season discharge. Therefore the effects of the decreased sand transport by the Mekong due to the redistribution of discharge from the wet to the dry season are likely to be already present in the delta.

(Brunier et al., 2014) found that channel morphology is currently not in equilibrium with the hydraulic parameters. This study showed that at the tide-river transition zone at My Thuan and Can Tho, increased erosion rates can be expected. In the most extreme case, transport rates double for this region (Figure 6.20) and anomalies in transport fluxes are in the order of 0.1 and 1Mt/y (Figure 9.9 . The limited resupply of sand by the reduced wet season discharge, will make this region extra vulnerable to increased incision rates. Leuven et al., 2021 states that the key factors favouring the formation of scour holes in tide-river transition zones are an increased tidal amplitude, a decreased fluvial discharge and a decreased upstream sediment supply. This study shows that, for the Mekong Delta, each of these factors are present at My Thuan. Binh et al., 2021 describes high incision rates already present in this region, attributing this to the heavy sand mining practices here. This study shows that a positive feedback occurs, where the lower river beds (or increased water depths) result in increased erosion rates in this region, accelerating the river bank erosion already present in the region (Hackney et al., 2020).

Only in the estuaries, an increased natural inflow of sand is expected. The increased erosion rates in the tide-river transition zone will increase the influx of sand towards the estuaries. At the same time, sand transport rates inside the estuaries are expected to decrease. Therefore, if no sand was extracted due to sand mining, the estuaries sand budgets will grow. This will only last as long as sand is available in the river bed in this region. Due to the heavy sand mining practises at My Thuan, it is uncertain if these reservoirs will last for this period.

From Figure 6.5, it can be seen that net annual transport rates in the smaller estuaries are small. With regard to annual sand transport, these estuaries are close to equilibrium. The changes in annual sand transport capacity (0.1-1Mt/y) found in this study could therefore alter annual net transport directions. Also, the low net annual transport rates imply that the residence time of sand in the smaller estuaries is long compared to the more river dominated estuaries (Dinhan, Trande and Bentrai). Sub-bottom profiling surveys from Deltares show that the sand thickness in the Anthuan and Vamkenh outlets is less than 1m, indicating that the sand reservoirs are small in these regions. This, together with the low net annual sand transport suggest that the effects of sand extraction is likely to remain present for a time period.

Comparing the magnitudes of the changes described above to the sand mining magnitude estimates (62.4-109.2 Mt/y, assuming $\rho_{sand} = 2650kg/m^3$), it can be concluded that the sand transport response to the hydrodynamic and morphological changes in the delta is relatively small. The morphological changes inside the delta are therefore mainly driven by the sand mining practises. Still, this study showed that changes in the future sand dynamics are contributing to the current problems that reside in the delta. The results of this study can be used to identify the areas where morphological changes due to the system's response are expected.

7.5. Future recommendations

The anthropologically driven hydro- and morphological changes described in this study are common in many tidal deltas worldwide (Lobo et al., 2018), (Bao et al., 2022) (Mei et al., 2021). Results from Bao et al., 2022 found a similar hydrodynamic response to river bed lowering in the different hydrodynamic regimes of the Pearl River Delta.Bao et al., 2022 reports increased tidal velocity amplitudes in the river-tide transition zone of the Pearl River that were also found at My Thuan in this study. Reduced upstream sand supply by the buffering effect dams have on the wet season discharge was found in the Changjiang Delta (Mei et al., 2021) Here, due to the wet season discharge through time, a landward shift in the maximum deposition zone was found. As this study provided the separate effect for each of these perturbations, the findings of this study can therefore be used to identify potential morphological changes in other tidally-influenced deltas (e.g. Ganges Delta, Indus Delta, Amazon Delta) where similar human influences are present. Future studies on a declining sand supply due to upstream dam construction and continued sea level rise will provide insight into the availability and movement of sand on longer timescales, as these actors will become more important for the deltas morphology over time.

Chapter 8

Conclusion

This study is the first that uses a state-of-the-art model to simulate the coupled hydro- and sand-dynamic response to anthropogenic changes in the Mekong Delta. First, the changing hydrodynamic and sand transport characteristics along the Mekong and Tien river were illustrated for the present situation. After this, 50cm of SLR, subsidence, river bed lowering and a projected 2040 wet season discharge were investigated to test their separate hydro- and sand dynamic response. In the end, future scenarios for 2040 were constructed where projected changes in SLR, subsidence, river bed lowering and an altered discharge were implemented collectively. The findings of this study present an insight into the sand transport mechanisms present at different hydrodynamic regimes (fluvial, fluvial-tidal and tidal) in the Mekong Delta and how these are projected to change in the coming future. The main findings of this study include:

- Sand transport from Kratie up to 250km from the sea is exclusively transported by river currents. Here the high river-induced sand transport rates vary greatly locally and correlate with the cross-sectional area of the river channel. A projected reduction in wet season discharge due to dam operation is the main driver for declining sand transport rates on an annual basis in this region. Although river bed lowering does not influence annual sand transport loads in this section, it reduces the deltas buffering effect on its seasonal discharge. Due to this, more sand is transported during the wet season relative to the dry season.
- From 250km from the sea, the influence of tides on sand transport rapidly increases. In this region, sand transport is a function of the tidal velocity amplitude together with mean river currents. In this region greater water depths as a result of subsidence, SLR and river bed lowering cause the tide to amplify. For channel deepening, this ultimately results in increased seaward sand transport rates which implies increased erosion rates for this region.
- At the My Thuan bifurcation, an abrupt decline in river influence causes the system to be almost exclusively tide-dominated. In this region, changes in wet season discharge have little influence on annual sand transport rates. Seasonal duality in the sand transport direction is present in the smaller estuaries, whereas the larger estuaries show seaward export of sand in both seasons. 50cm of SLR, subsidence and river bed deepening causes amplification of the tidal velocity amplitude. Further deepening as implemented in future scenarios causes the tidal velocity amplitudes to decline. This ultimately results in declined net sand transport rates decrease for both 2040 scenarios in this region.

The sand volumes extracted by sand mining, dominate the changes in sand transport modelled in this study. Therefore sand mining is the main driver for the direct morphological changes inside the delta. This study showed that the system response amplifies the current problems that reside in the delta.

Results of this study can be used to identify the areas where morphological changes due to the system's response to anthropogenic perturbations are expected. As the hydrodynamic regimes and changes investigated are similar for other tidal deltas worldwide, the findings of this study can act as an example for current and future sand transport mechanisms in different tidal deltas.

Bibliography

Abdulazeez, A. (n.d.). *A Review on the Impact of River and Inland Sand Mining on Nigerian River Basins. The Impact of Sand and Laterite Mining in the Watari River Basin of Kano State View project* (tech. rep.). https://www.researchgate.net/publication/343481022

Allison, M. A., Dallon Weathers, H., & Meselhe, E. A. (2017). Bottom morphology in the Song Hau distributary channel, Mekong River Delta, Vietnam. *Continental Shelf Research*, *147*, 51–61. https://doi.org/10.1016/J.CSR.2017.05.010

Anh, D. T., Hoang, L. P., Bui, M. D., & Rutschmann, P. (2018). Modelling seasonal flows alteration in the Vietnamese Mekong Delta under upstream discharge changes, rainfall changes and sea level rise. *https://doi.org/10.1080/15715124.2018.1505735*, *17*(4), 435–449. https://doi.org/10.1080/15715124.2018.1505735

Anthony, E. J., Brunier, G., Besset, M., Goichot, M., Dussouillez, P., & Nguyen, V. L. (2015). Linking rapid erosion of the Mekong River delta to human activities. *Scientific Reports 2015 5:1*, *5*(1), 1–12. https://doi.org/10.1038/srep14745

Bao, S., Zhang, W., Qin, J., Zheng, J., Lv, H., Feng, X., Xu, Y., & Hoitink, A. J. (2022). Peak Water Level Response to Channel Deepening Depends on Interaction Between Tides and the River Flow. *Journal of Geophysical Research: Oceans*, *127*(4), e2021JC017625. https://doi.org/10.1029/2021JC017625

Barlow, C., Campbell, I., Carson, S., Johnston, R., Juntopas, M., Lund, A., Mak, S., Mya, S., Nhoybouakong, S., Novak, S., & Pedersen, C. A. (2003). State of the Basin Report 2003 Coordination and Editing: Ann Bishop Design and Layout: Boonruang Song-ngam.

Binh, D. V., Kantoush, S., & Sumi, T. (2020). Changes to long-term discharge and sediment loads in the Vietnamese Mekong Delta caused by upstream dams. *Geomorphology*, *353*, 107011. https://doi.org/10.1016/J.GEOMORPH.2019.107011

Binh, D. V., Kantoush, S. A., Ata, R., Tassi, P., Nguyen, T. V., Lepesqueur, J., Abderrezzak, K. E. K., Bourban, S. E., Nguyen, Q. H., Phuong, D. N. L., Trung, L. V., Tran, D. A., Letrung, T., & Sumi, T. (2022). Hydrodynamics, sediment transport, and morphodynamics in the Vietnamese Mekong Delta: Field study and numerical modelling. *Geomorphology*, *413*, 108368. https://doi.org/10.1016/J.GEOMORPH.2022.108368

Binh, D. V., Kantoush, S. A., Sumi, T., Mai, N. P., Ngoc, T. A., Trung, L. V., & An, T. D. (2021). Effects of riverbed incision on the hydrology of the Vietnamese Mekong Delta. *Hydrological Processes*, *35*(2), e14030. https://doi.org/10.1002/HYP.14030

Bravard, J.-P., Goichot, M., & Gaillot, S. (2013). Geography of Sand and Gravel Mining in the Lower Mekong River. *http://journals.openedition.org/echogeo*, (26). https://doi.org/10.4000/ECHOGEO.13659

Brunier, G., Anthony, E. J., Goichot, M., Provansal, M., & Dussouillez, P. (2014). Recent morphological changes in the Mekong and Bassac river channels, Mekong delta: The marked impact of river-bed mining and implications for delta destabilisation. *Geomorphology*, *224*, 177–191. https://doi.org/10.1016/j.geomorph.2014.07.009

Chua, S. D. X., Lu, X. X., Oeurng, C., Sok, T., & Grundy-Warr, C. (2022). Drastic decline of flood pulse in the Cambodian floodplains (Mekong River and Tonle Sap system). *Hydrology and Earth System Sciences*, *26*(3), 609–625. https://doi.org/10.5194/HESS-26-609-2022

Cook, B. I., Bell, A. R., Anchukaitis, K. J., & Buckley, B. M. (2012). Snow cover and precipitation impacts on dry season streamflow in the Lower Mekong Basin. *Journal of Geophysical Research Atmospheres*, *117*(16). https://doi.org/10.1029/2012JD017708

Deltares. (2023). *Delft3D fM Suite 2D3D Simulation software for safe, sustainable and future deltas User Manual D-Morphology* (tech. rep.).

Egbert, G. D., & Erofeeva, S. Y. (2002). *Efficient Inverse Modeling of Barotropic Ocean Tides* (tech. rep.).

Eslami, S., Hoekstra, P., Minderhoud, P. S., Trung, N. N., Hoch, J. M., Sutanudjaja, E. H., Dung, D. D., Tho, T. Q., Voepel, H. E., Woillez, M. N., & van der Vegt, M. (2021). Projections of salt intrusion in a mega-delta under climatic and anthropogenic stressors. *Communications Earth & Environment 2021 2:1*, *2*(1), 1–11. https://doi.org/10.1038/s43247-021-00208-5

Eslami, S., Hoekstra, P., Nguyen Trung, N., Ahmed Kantoush, S., Van Binh, D., Duc Dung, D., Tran Quang, T., & van der Vegt, M. (2019). Tidal amplification and salt intrusion in the Mekong Delta driven by anthropogenic sediment starvation. *Scientific Reports 2019 9:1*, *9*(1), 1–10. https://doi.org/10.1038/s41598-019-55018-9

Friedrichs, C. T. (2010). Barotropic tides in channelized estuaries. In *Contemporary issues in estuarine physics* (pp. 27–61). Cambridge University Press. https://doi.org/10.1017/CBO9780511676567.004

Gatto, V. M., van Prooijen, B. C., & Wang, Z. B. (2017). Net sediment transport in tidal basins: quantifying the tidal barotropic mechanisms in a unified framework. *Ocean Dynamics*, *67*(11), 1385–1406. https://doi.org/10.1007/s10236-017-1099-3

GitHub - Deltares/hatyan: Harmonic tidal analysis and prediction. (n.d.). https://github.com/Deltares/hatyan

Godin, G. (1972). *The Analysis of Tides* (1st edn). University of Toronto Press.

Gruel, C. R., Park, E., Switzer, A. D., Kumar, S., Loc Ho, H., Kantoush, S., Van Binh, D., & Feng, L. (2022). New systematically measured sand mining budget for the Mekong Delta reveals rising trends and significant volume underestimations. *International Journal of Applied Earth Observation and Geoinformation*, *108*, 102736. https://doi.org/10.1016/J.JAG.2022.102736

Gugliotta, M., Saito, Y., Nguyen, V. L., Ta, T. K. O., Nakashima, R., Tamura, T., Uehara, K., Katsuki, K., & Yamamoto, S. (2017). Process regime, salinity, morphological, and sedimentary trends along the fluvial to marine transition zone of the mixed-energy Mekong River delta, Vietnam. *Continental Shelf Research*, *147*, 7–26. https://doi.org/10.1016/J.CSR.2017.03.001

Gugliotta, M., Saito, Y., Nguyen, V. L., Ta, T. K. O., & Tamura, T. (2019). Sediment distribution and depositional processes along the fluvial to marine transition zone of the Mekong River delta, Vietnam. *Sedimentology*, *66*(1), 146–164. https://doi.org/10.1111/SED.12489

Hackney, C. R., Darby, S. E., Parsons, D. R., Leyland, J., Best, J. L., Aalto, R., Nicholas, A. P., & Houseago, R. C. (2020). River bank instability from unsustainable sand mining in the lower Mekong River. *Nature Sustainability 2020 3:3*, *3*(3), 217–225. https://doi.org/10.1038/s41893-019-0455-3

Jordan, C., Tiede, J., Lojek, O., Visscher, J., Apel, H., Nguyen, H. Q., Quang, C. N. X., & Schlurmann, T. (2019). Sand mining in the Mekong Delta revisited - current scales of local sediment deficits. *Scientific Reports 2019 9:1*, *9*(1), 1–14. https://doi.org/10.1038/s41598-019-53804-z

Kallio, M., & Kummu, M. (2021). Comment on 'Changes of inundation area and water turbidity of Tonle Sap Lake: Responses to climate changes or upstream dam construction?' https://doi.org/10.1088/1748-9326/abf3da

Kernkamp, H. W., Van Dam, A., Stelling, G. S., & De Goede, E. D. (2011). Efficient scheme for the shallow water equations on unstructured grids with application to the Continental Shelf. *Ocean Dynamics*, *61*(8), 1175–1188. https://doi.org/10.1007/s10236-011-0423-6

Kondolf, G. M., Rubin, Z. K., & Minear, J. T. (2014). Dams on the Mekong: Cumulative sediment starvation. *Water Resources Research*, *50*(6), 5158–5169. https://doi.org/10.1002/2013WR014651

Kummu, M., Tes, S., Yin, S., Adamson, P., Józsa, J., Koponen, J., Richey, J., & Sarkkula, J. (2014). Water balance analysis for the Tonle Sap Lake–floodplain system. *Hydrological Processes*, *28*(4), 1722–1733. https://doi.org/10.1002/HYP.9718

Kummu, M., & Sarkkula, J. (2008). Impact of the Mekong River Flow Alteration on the Tonle Sap Flood Pulse. *https://doi.org/10.1579/0044-7447(2008)37[185:IOTMRF]2.0.CO;2*, *37*(3), 185–192. https://doi.org/10.1579/0044-7447(2008)37

Kummu, M., & Varis, O. (2007). Sediment-related impacts due to upstream reservoir trapping, the Lower Mekong River. *Geomorphology*, *85*(3-4), 275–293. https://doi.org/10.1016/J.GEOMORPH.2006.03.024

Lauri, H., De Moel, H., Ward, P. J., Räsänen, T. A., Keskinen, M., & Kummu, M. (2012). Hydrology and Earth System Sciences Future changes in Mekong River hydrology: impact of climate change and reservoir operation on discharge. *Hydrol. Earth Syst. Sci*, *16*, 4603–4619. https://doi.org/10.5194/hess-16-4603-2012

Leuven, J. R., van Keulen, D., Nienhuis, J. H., Canestrelli, A., & Hoitink, A. J. (2021). Large-Scale Scour in Response to Tidal Dominance in Estuaries. *Journal of Geophysical Research: Earth Surface*, *126*(5). https://doi.org/10.1029/2020JF006048

Li, X., Liu, J. P., Saito, Y., & Nguyen, V. L. (2017). Recent evolution of the Mekong Delta and the impacts of dams. *Earth-Science Reviews*, *175*, 1–17. https://doi.org/10.1016/J.EARSCIREV.2017.10.008

Lobo, F. d. L., Souza-Filho, P. W. M., Novo, E. M. L. d. M., Carlos, F. M., & Barbosa, C. C. F. (2018). Mapping Mining Areas in the Brazilian Amazon Using MSI/Sentinel-2 Imagery (2017). *Remote Sensing 2018, Vol. 10, Page 1178*, *10*(8), 1178. https://doi.org/10.3390/RS10081178

Lu, X., Kummu, M., & Oeurng, C. (2014). Reappraisal of sediment dynamics in the Lower Mekong River, Cambodia. *Earth Surface Processes and Landforms*, *39*(14), 1855–1865. https://doi.org/10.1002/ESP.3573

Manh, N. V., Dung, N. V., Hung, N. N., Kummu, M., Merz, B., & Apel, H. (2015). Future sediment dynamics in the Mekong Delta floodplains: Impacts of hydropower development, climate change and sea level rise. *Global and Planetary Change*, *127*, 22–33. https://doi.org/10.1016/J.GLOPLACHA.2015.01.001

Mei, X., Dai, Z., Darby, S. E., Zhang, M., Cai, H., Wang, J., & Wei, W. (2021). Landward shifts of the maximum accretion zone in the tidal reach of the Changjiang estuary following construction of the Three Gorges Dam. *Journal of Hydrology*, *592*. https://doi.org/10.1016/j.jhydrol.2020.125789

Minderhoud, P. S., Coumou, L., Erkens, G., Middelkoop, H., & Stouthamer, E. (2019). Mekong delta much lower than previously assumed in sea-level rise impact assessments. *Nature Communications 2019 10:1*, *10*(1), 1–13. https://doi.org/10.1038/s41467-019-11602-1

Minderhoud, P. S., Erkens, G., Pham, V. H., Bui, V. T., Erban, L., Kooi, H., & Stouthamer, E. (2017). Impacts of 25 years of groundwater extraction on subsidence in the Mekong delta, Vietnam. *Environmental Research Letters*, *12*(6). https://doi.org/10.1088/1748-9326/aa7146

Minderhoud, P. S., Middelkoop, H., Erkens, G., & Stouthamer, E. (2020). Groundwater extraction may drown mega-delta: Projections of extraction-induced subsidence and elevation of the mekong delta for the 21st century. https://doi.org/10.1088/2515-7620/ab5e21

MONRE, M. o. N. R., & Environment. (2016). Climate Change and Sea Level Rise Scenarios for Vietnam, Ministry of Natural Resources and Environment.

Moriasi, D. N., Arnold, J. G., Liew, M. W. V., Bingner, R. L., Harmel, R. D., & Veith, T. L. (2007). Model Evaluation Guidelines for Systematic Quantification of Accuracy in Watershed Simulations. *Transactions of the ASABE*, *50*(3), 885–900. https://doi.org/10.13031/2013.23153

MRC. (n.d.). MRC - Data Portal. https://portal.mrcmekong.org/data-catalogue?q=17c0ffe74e224b50a9e3142fc4042size=n_20_n

MRC. (2017). *THE SUSTAINABLE MANAGEMENT AND DEVELOPMENT OF THE MEKONG RIVER INCLUDING IMPACTS OF MAINSTREAM HYDROPOWER PROJECTS* (tech. rep.).

NASH, S. (1970). Nash JE, Sutcliffe JV-River flow forecasting through conceptual models. *Journal of Hydrology*, *10*, 282–290.

Nittrouer, J. A., Shaw, J., Lamb, M. P., & Mohrig, D. (2012). Spatial and temporal trends for water-flow velocity and bed-material sediment transport in the lower Mississippi River. *Bulletin of the Geological Society of America*, *124*(3-4), 400–414. https://doi.org/10.1130/B30497.1

Nowacki, D. J., Ogston, A. S., Nittrouer, C. A., Fricke, A. T., & Van, P. D. T. (2015). Sediment dynamics in the lower Mekong River: Transition from tidal river to estuary. *Journal of Geophysical Research: Oceans*, *120*(9), 6363–6383. https://doi.org/10.1002/2015JC010754

Ogston, A. S., Allison, M. A., Mullarney, J. C., & Nittrouer, C. A. (2017). Sediment- and hydro-dynamics of the Mekong Delta: From tidal river to continental shelf. *Continental Shelf Research*, *147*, 1–6. https://doi.org/10.1016/J.CSR.2017.08.022

OpenEarth. (n.d.). https://www.openearth.nl/

Park, E., Ho, H. L., Tran, D. D., Yang, X., Alcantara, E., Merino, E., & Son, V. H. (2020). Dramatic decrease of flood frequency in the Mekong Delta due to river-bed mining and dyke construction. *Science of The Total Environment*, *723*, 138066. https://doi.org/10.1016/J.SCITOTENV.2020.138066

Quoc Thanh, V., Quoc Thanh, V., Roelvink, D., Van Der Wegen, M., Reyns, J., Kernkamp, H., Van Vinh, G., & Thi Phuong Linh, V. (2020). Flooding in the Mekong Delta: The impact of dyke systems on downstream hydrodynamics. *Hydrology and Earth System Sciences*, *24*(1), 189–212. https://doi.org/10.5194/HESS-24-189-2020

Stephens, J. D., Allison, M. A., Di Leonardo, D. R., Weathers, H. D., Ogston, A. S., McLachlan, R. L., Xing, F., & Meselhe, E. A. (2017). Sand dynamics in the Mekong River channel and export to the coastal ocean. *Continental Shelf Research*, *147*, 38–50. https://doi.org/10.1016/J.CSR.2017.08.004

Ta, T. K. O., Nguyen, V. L., Tateishi, M., Kobayashi, I., Tanabe, S., & Saito, Y. (2002). Holocene delta evolution and sediment discharge of the Mekong River, southern Vietnam. *Quaternary Science Reviews*, *21*(16-17), 1807–1819. https://doi.org/10.1016/S0277-3791(02)00007-0

Takagi, H., Ty, T. V., Thao, N. D., & Esteban, M. (2015). Ocean tides and the influence of sea-level rise on floods in urban areas of the Mekong Delta. *Journal of Flood Risk Management*, *8*(4), 292–300. https://doi.org/10.1111/JFR3.12094

Thanh, Q. V. (2021). *Modeling of Hydrodynamics and Sediment Transport in the Mekong Delta*. https://doi.org/10.1201/9781003193913

Thanh, V. Q., Reyns, J., Wackerman, C., Eidam, E. F., & Roelvink, D. (2017). Modelling suspended sediment dynamics on the subaqueous delta of the Mekong River. *Continental Shelf Research*, *147*(July), 213–230. https://doi.org/10.1016/j.csr.2017.07.013

Thanh, V. Q., Roelvink, D., van der Wegen, M., Tu, L. X., Reyns, J., & Linh, V. T. P. (2020). Spatial Topographic Interpolation for Meandering Channels. *Journal of Waterway, Port, Coastal, and Ocean Engineering*, *146*(5), 1–11. https://doi.org/10.1061/(asce)ww.1943-5460.0000582

Tu, L. X., Thanh, V. Q., Reyns, J., Van, S. P., Anh, D. T., Dang, T. D., & Roelvink, D. (2019). Sediment transport and morphodynamical modeling on the estuaries and coastal zone of the Vietnamese Mekong Delta. *Continental Shelf Research*, *186*, 64–76. https://doi.org/10.1016/J.CSR.2019.07.015

Van Rijn. (1993). *SIMPLE GENERAL FORMULAE FOR SAND TRANSPORT IN RIVERS, ESTUARIES AND COASTAL WATERS* (tech. rep.). www.leovanrijn-sediment.com

Vasilopoulos, G., Quan, Q. L., Parsons, D. R., Darby, S. E., Tri, V. P., Hung, N. N., Haigh, I. D., Voepel, H. E., Nicholas, A. P., & Aalto, R. (2021). Establishing sustainable sediment budgets is critical for climate-resilient mega-deltas. *Environmental Research Letters*, *16*(6), 064089. https://doi.org/10.1088/1748-9326/AC06FC

Wang, Y., Feng, L., Liu, J., Hou, X., & Chen, D. (2020). Changes of inundation area and water turbidity of Tonle Sap Lake: responses to climate changes or upstream dam construction? *Environ. Res. Lett*, *15*, 940–941. https://doi.org/10.1088/1748-9326/abac79

Wolanski, E., Huan, N. N., Dao, L. T., Nhan, N. H., & Thuy, N. N. (1996). Fine-sediment dynamics in the Mekong River Estuary, Vietnam. *Estuarine, Coastal and Shelf Science*, *43*(5), 565–582. https://doi.org/10.1006/ECSS.1996.0088

WWF. (2018). The sands are running out: Sediment in the Mekong river basin.

Xing, F., Meselhe, E. A., Allison, M. A., & Weathers, H. D. (2017). Analysis and numerical modeling of the flow and sand dynamics in the lower Song Hau channel, Mekong Delta. *Continental Shelf Research*, *147*, 62–77. https://doi.org/10.1016/J.CSR.2017.08.003

Xue, Z., Liu, J. P., DeMaster, D., Van Nguyen, L., & Ta, T. K. O. (2010). Late Holocene Evolution of the Mekong Subaqueous Delta, Southern Vietnam. *Marine Geology*, *269*(1-2), 46–60. https://doi.org/10.1016/J.MARGEO.2009.12.005

Zoccarato, C., Minderhoud, P. S., & Teatini, P. (2018). The role of sedimentation and natural compaction in a prograding delta: insights from the mega Mekong delta, Vietnam. *Scientific Reports 2018 8:1*, *8*(1), 1–12. https://doi.org/10.1038/s41598-018-29734-7

Chapter 9

Appendix

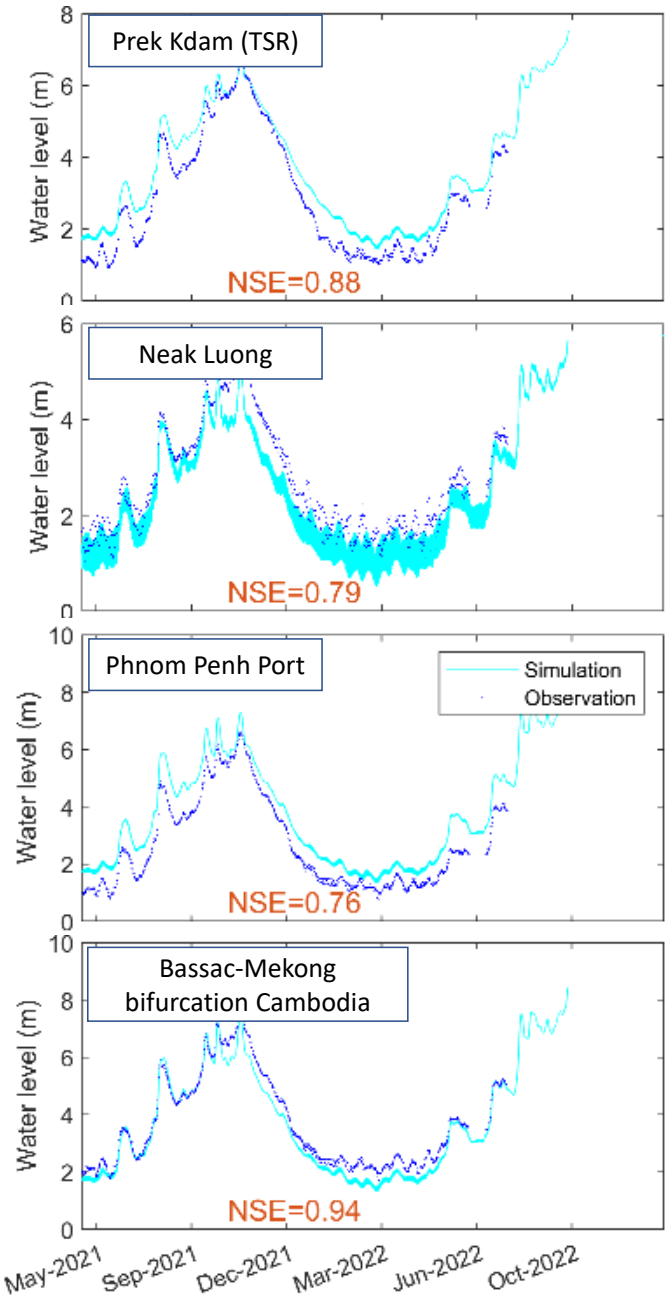

Figure 9.1: One year measured and simulated water levels at Cambodian part of the study area. For the calibration, the 2022 measured water levels are used. NSE indicates the Nash-Sutcliffe efficiency NASH, 1970

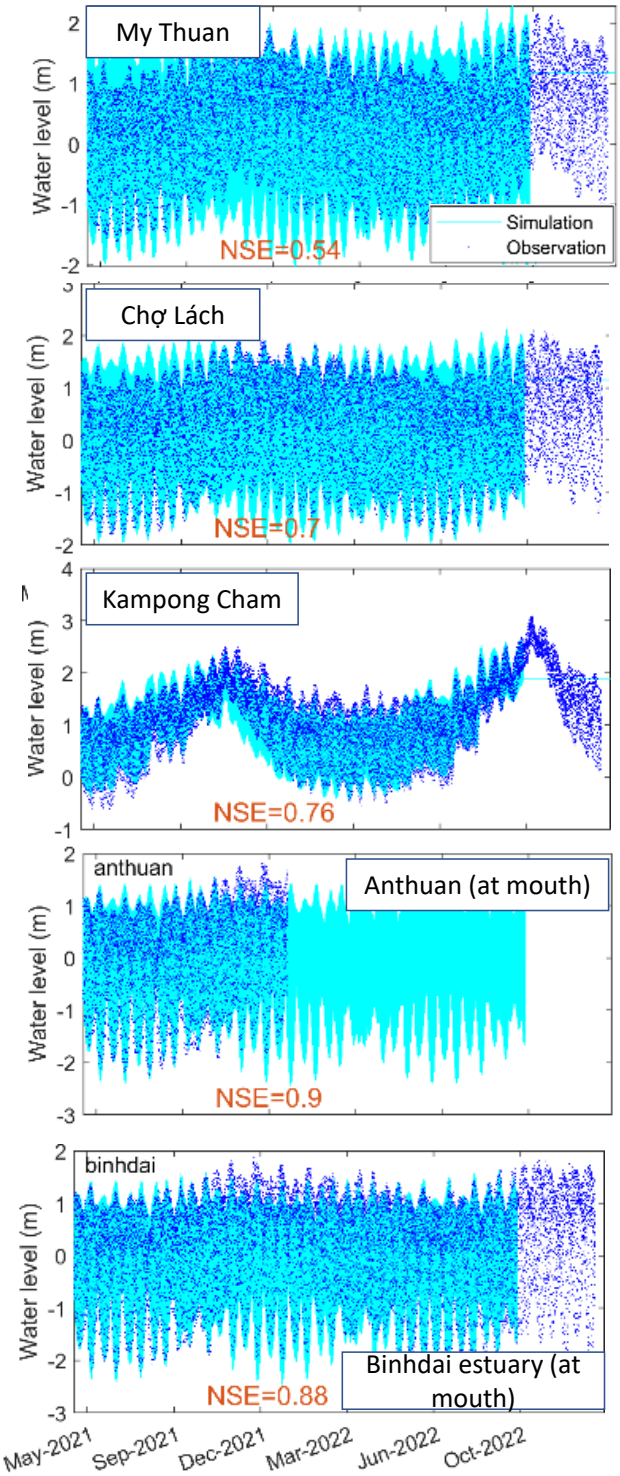

Figure 9.2: One year measured and simulated water levels at Vietnamese part of the study area. For the calibration, the 2022 measured water levels are used. NSE indicates the Nash-Sutcliffe efficiency NASH, 1970

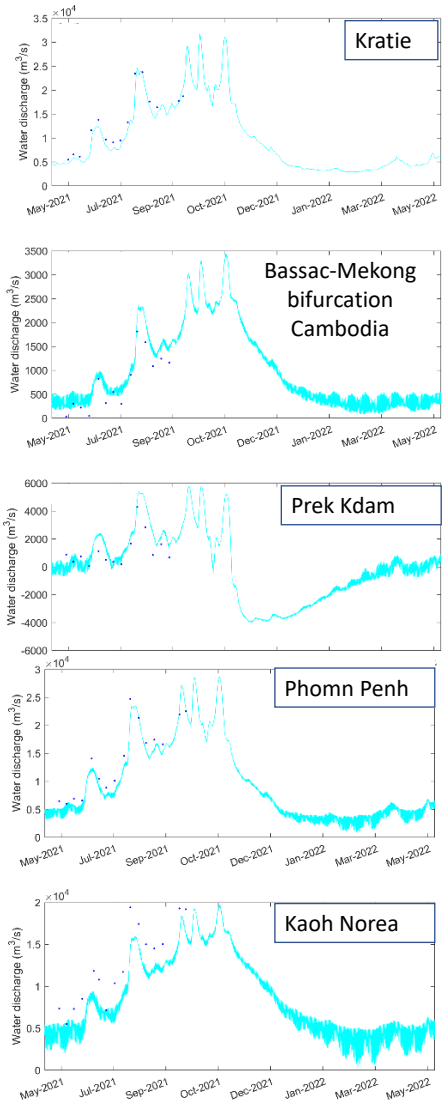

Figure 9.3: One year measured and simulated discharge at Cambodian part of the study area. For the calibration, the 2022 measured discharge is used. NSE indicates the Nash-Sutcliffe efficiency NASH, 1970

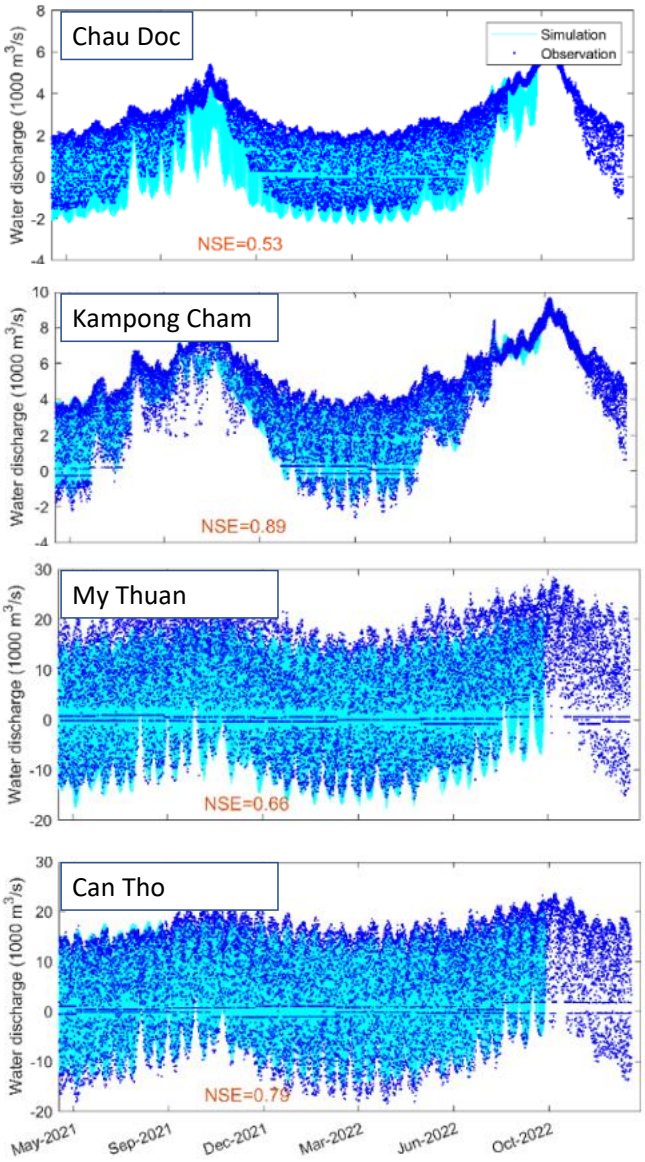

Figure 9.4: One year measured and simulated discharge at Vietnamese part of the study area. For the calibration, the 2022 measured discharge is used. NSE indicates the Nash-Sutcliffe efficiency NASH, 1970

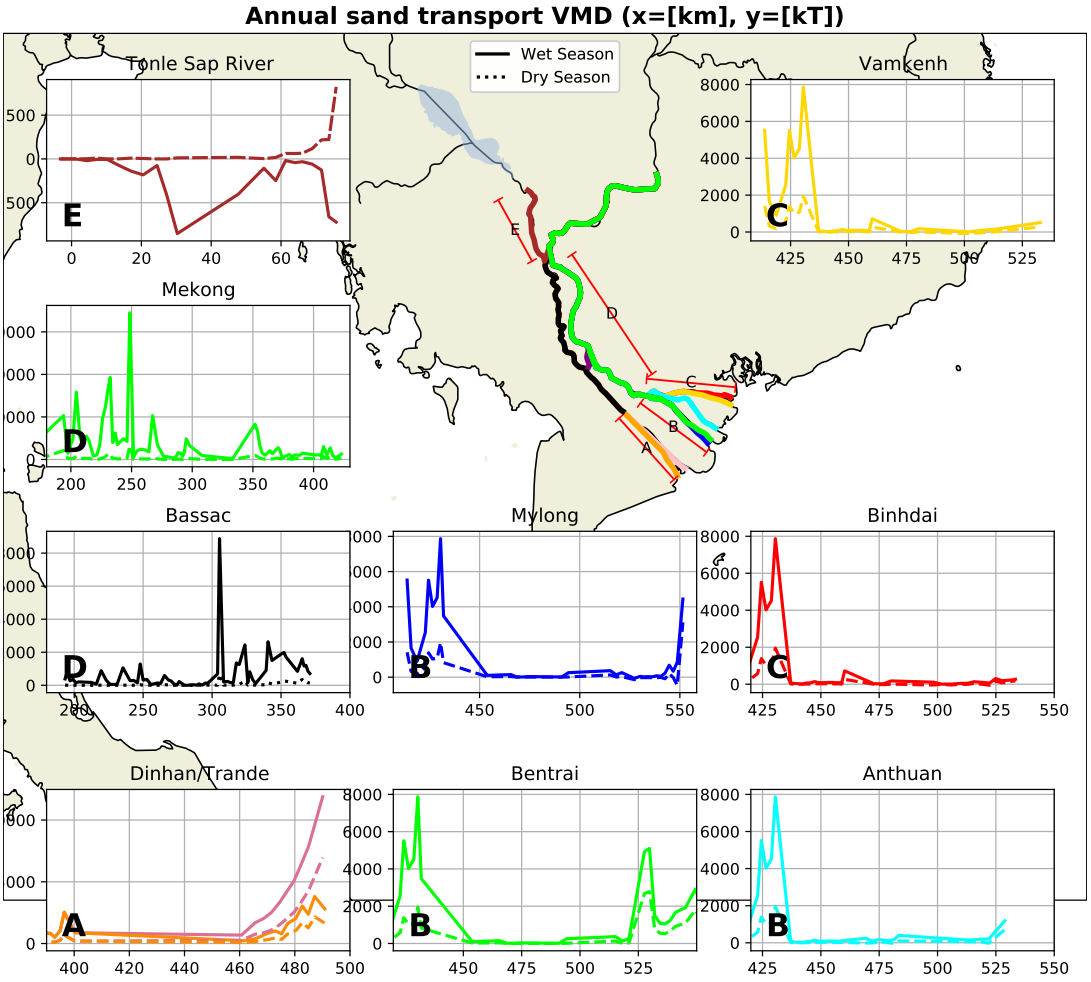

Figure 9.5: Wet season (solid) and dry season (dotted) total transport volumes for each branch. Distances are calculated from the most upstream location in Cambodia (Kratie x=0). Distance 0 for TSR is at TSL. Sand transport quantities indicated in the graphs are in [kT] and positive in the seaward direction.

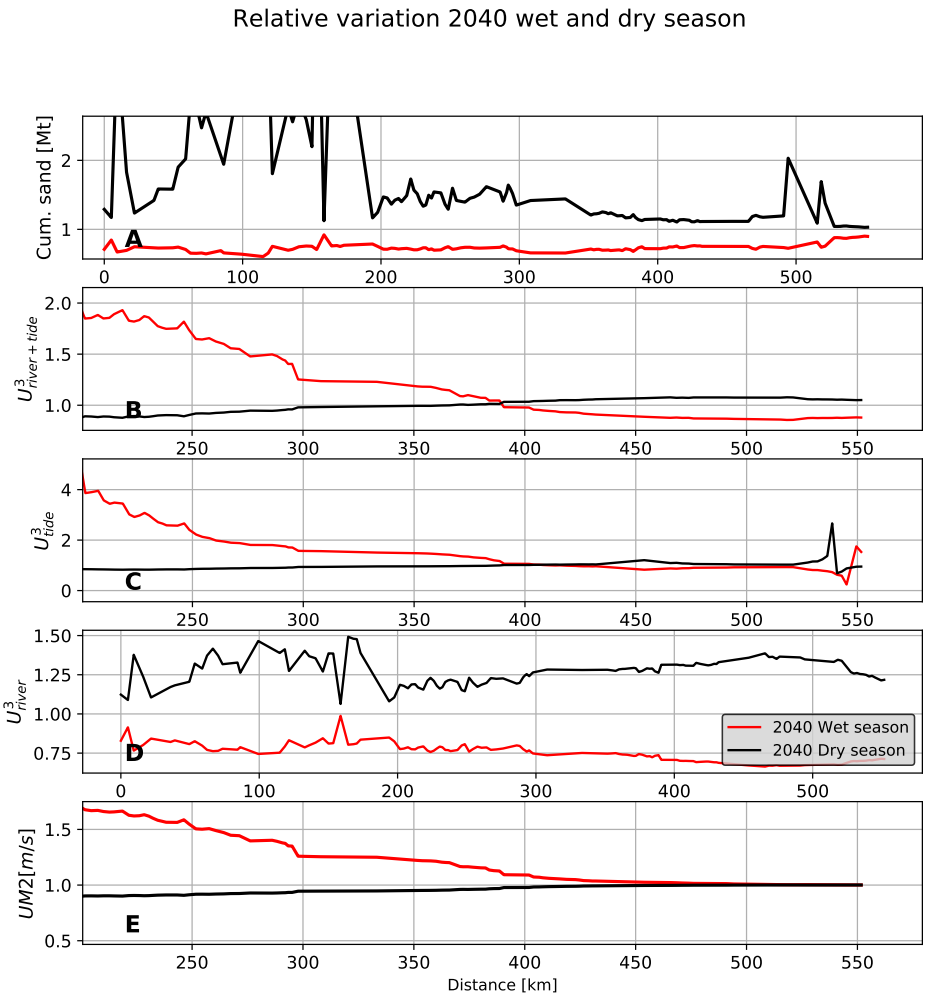

Figure 9.6: Indicates relative changes in sand transport (parameter) for the wet (red) and dry (black) seasons of 2040 compared to the present wet and dry season. The model was run for one year with a 2040 discharge and compared to the present day discharge simulation for both seasons. Panels where tidal influences are shown are taken from Phomn Penh (200km). River influence and cumulative sand transport are taken from Kratie (0km). Panels indicate relative changes for: A) Cumulative sand transport, B) Sand transport by tide-river interaction, C) Sand transport due to tidal asymmetry, D) Sand transport by river currents ,E) M2 velocity amplitude UM2.)

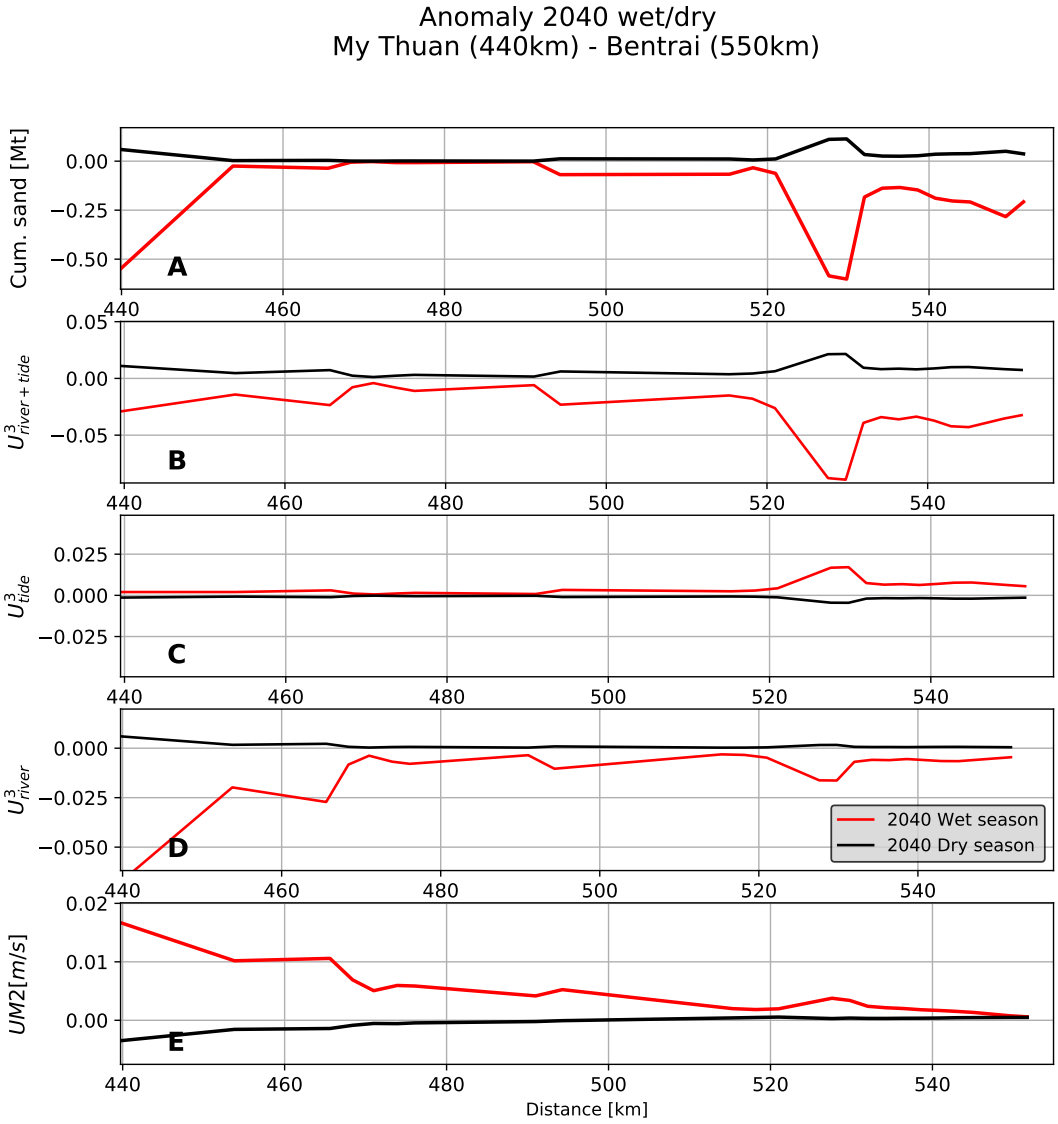

Figure 9.7: Indicates sand transport (parameter) anomalies for the wet and dry seasons of 2040 compared to the present wet and dry season. The model was run for one year with a 2040 discharge and compared to the present day discharge simulation for both seasons. The transect was taken from My Thuan (440km) to the Bentrai outlet (550km) (lime branch in Figure 4.1).Panels indicate anomalies for: A) Cumulative sand transport [Mt], B) Sand transport by tide-river interaction, C) Sand transport due to tidal asymmetry, D) Sand transport by river currents ,E) M2 velocity amplitude UM2. The figure shows only little variation in the annual downstream sand transport rates.)

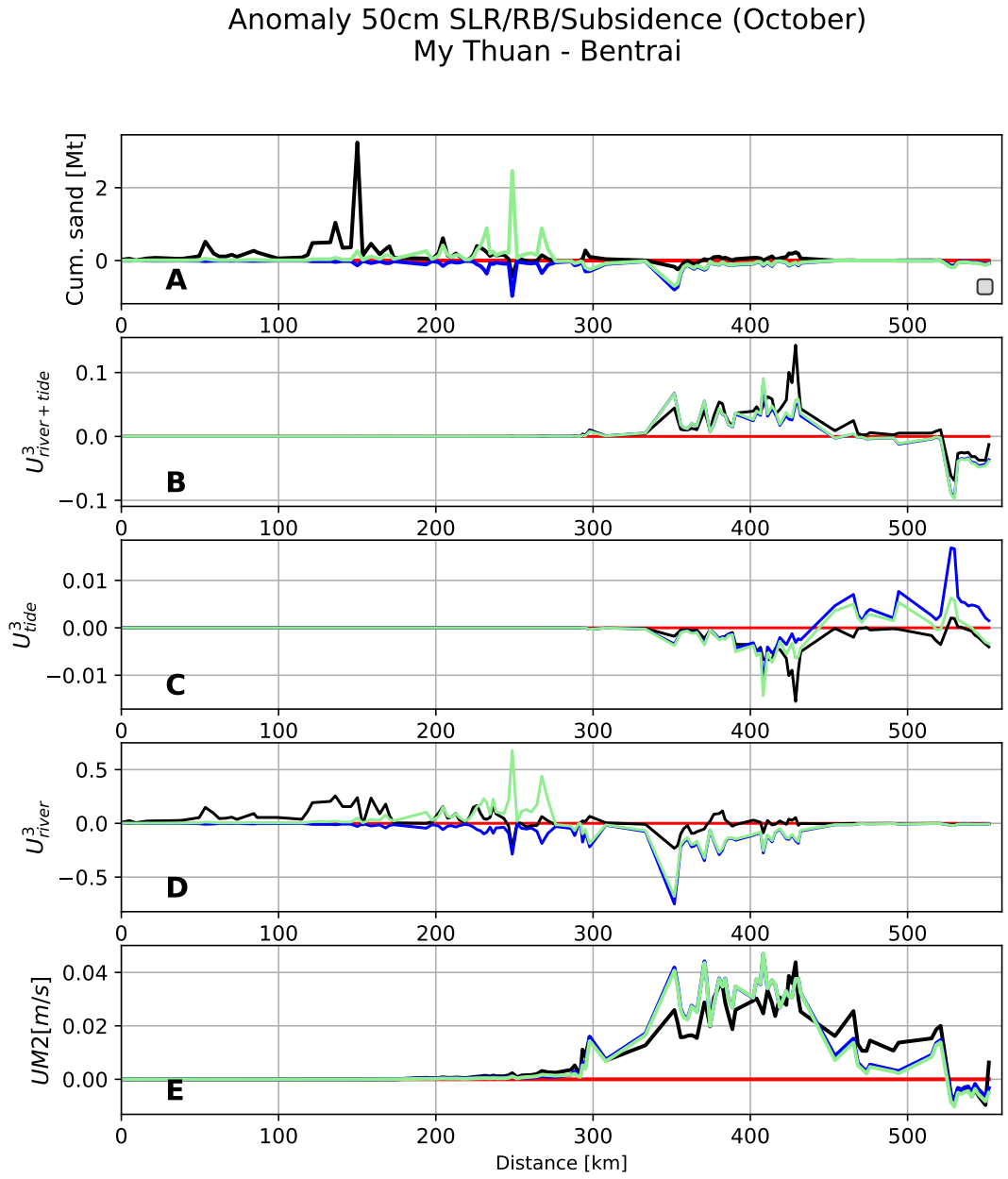

Figure 9.8: Indicates anomalies 50cm of SLR, subsidence and RB. The model was run for one year with a 2040 discharge. Results for the month October are displayed in this figure. The transect was taken from Kratie (x=0km) via the Tien River up to the Bentrai outlet (x=550) (lime branch in Figure 4.1). A) Cumulative sand transport [Mt], B) Sand transport by tide-river interaction, C) Sand transport due to tidal asymmetry, D) Sand transport by river currents ,E) M2 velocity amplitude UM2. The figure shows increased sand transport rates for RB in the Cambodian/Upper delta (fluvial dominated) section.

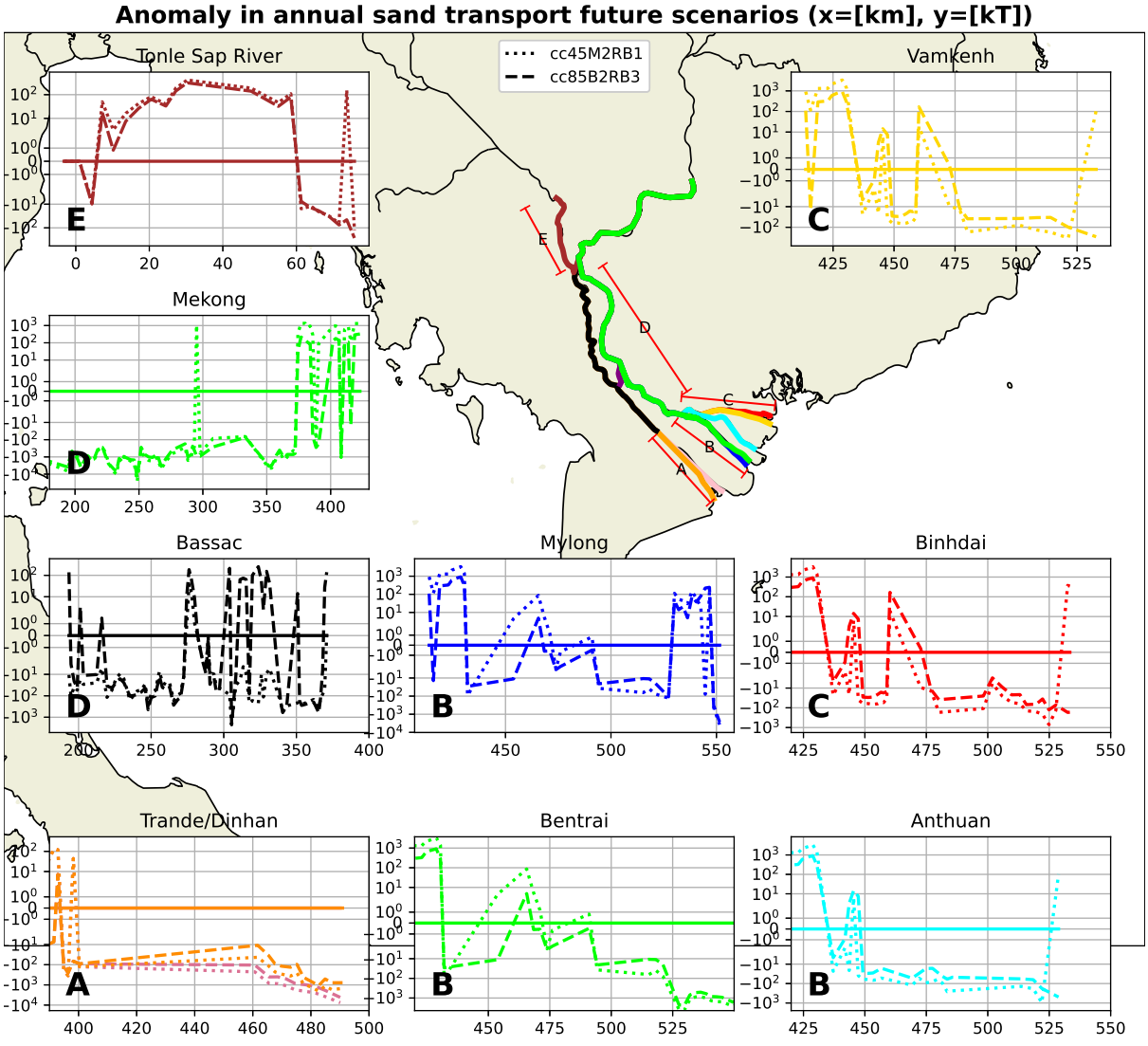

Figure 9.9: Annual sand transport volume anomalies (in kT) for both future scenarios compared to the current situation. Each graph corresponds to one of the transects displayed on the map. For all transects except Tonle Sap River, distances are from Kratie. For Tonle Sap River x=0 at Tonle Sap Lake.

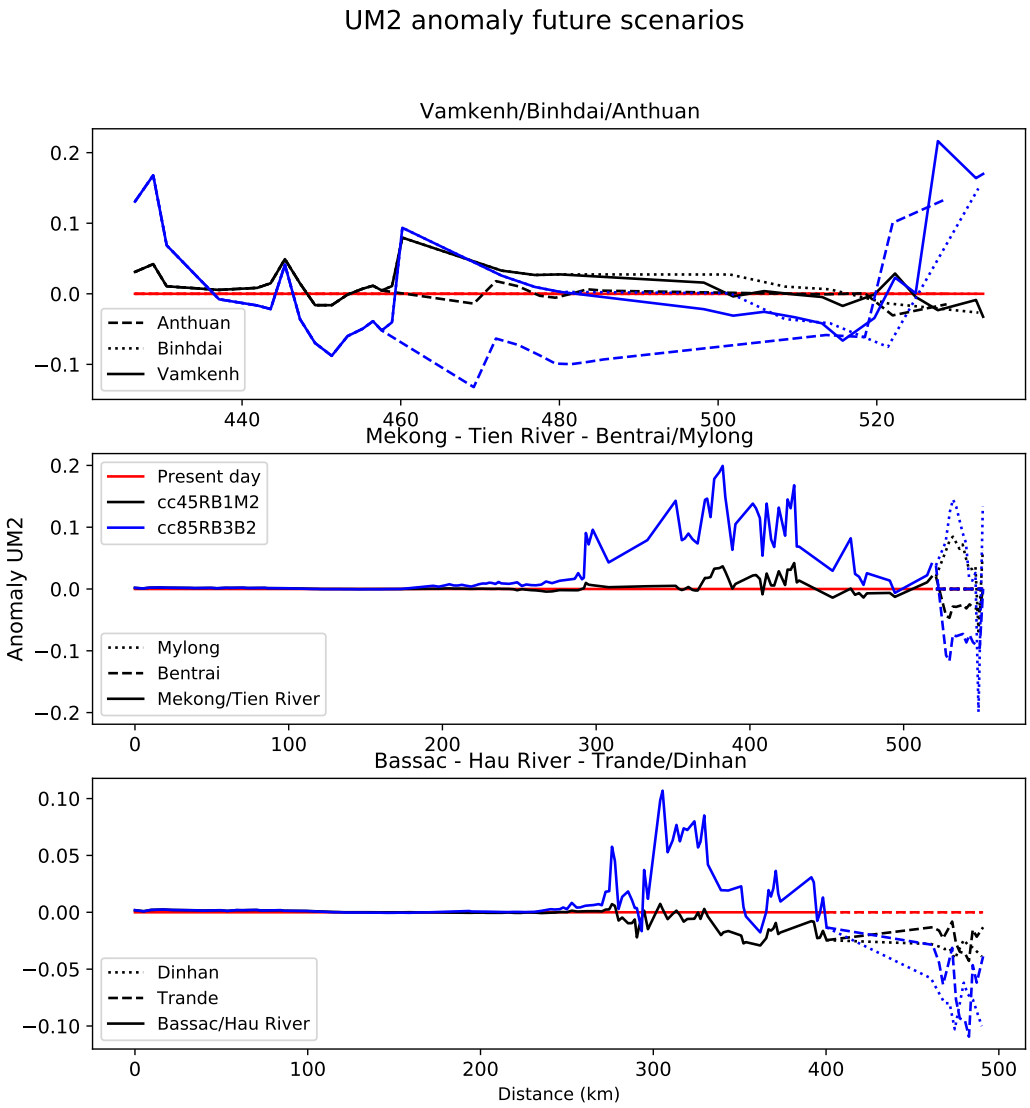

Figure 9.10: Absolute UM2 anomalies in [m/s] for both 2040 scenarios compared to the present day. Upper figure covers the outlets Vamkenh (solid), Binhdai (dotted) and Anthuan (dashed) from My Thuan (x=440). Middle figure includes the Mylong (dotted) and Bentrai (dashed) outlet from Kratie via the Mekong and Tien river (solid) from Kratie (x=0) up to the mouth. Lower figure shows the Trande (dashed) and Dinhan outlets up to Kratie from Phomn Penh. The different markers indicte the different branches. All distances are relative to Kratie (x=0). Tidal analysis was done for the month of October (wet season).

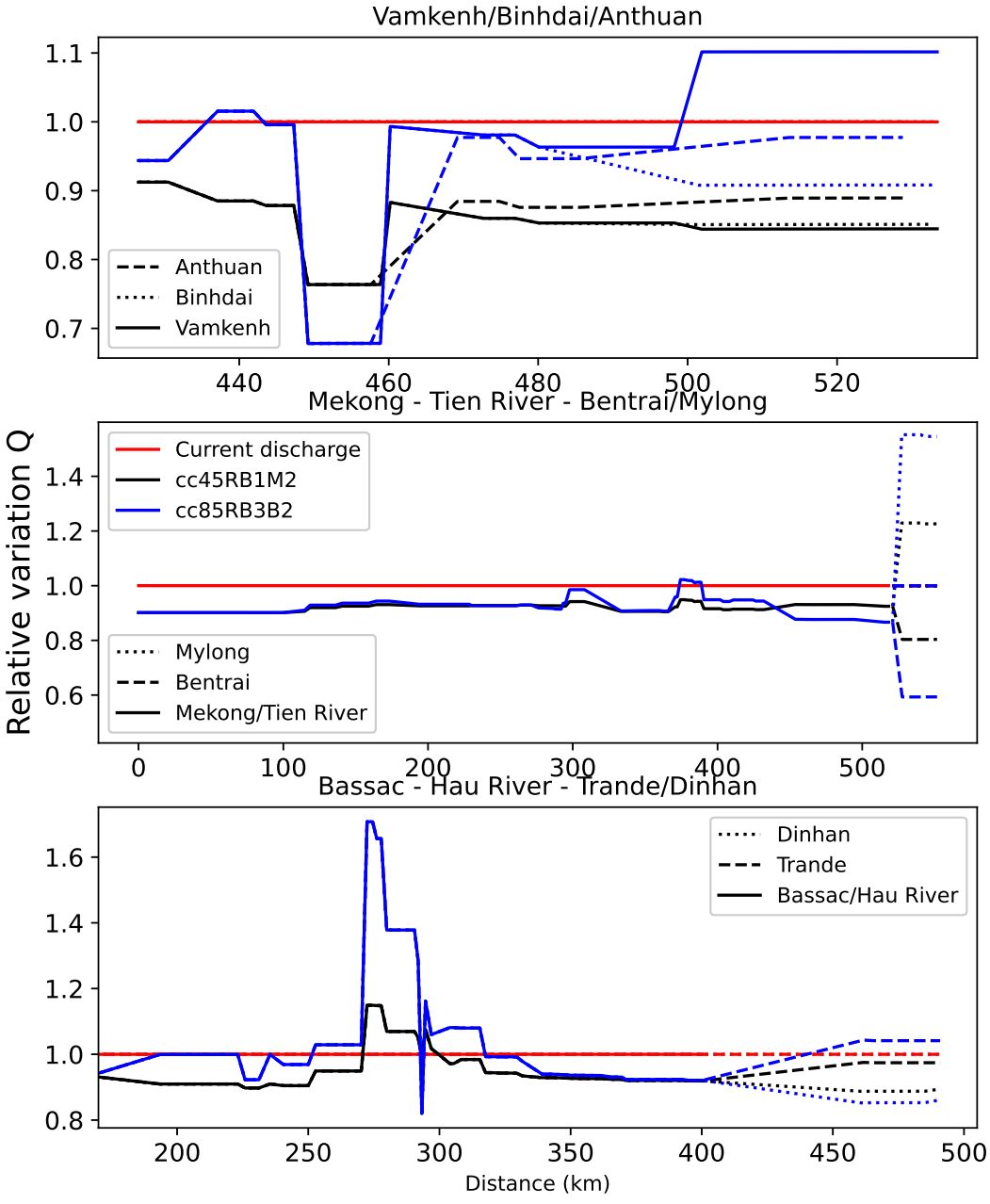

Figure 9.11: Annual cumulative discharge anomaly for every branch compared to the current situation. Blue indicates CC85RB3B2, black indicates CC45RB1M2, the different markers indicate the different branches/outlets.